# Wetting dynamics on soft surfaces

## Dissertation

for the award of the degree
"Doctor rerum naturalium"
of the Georg-August-Universität Göttingen

within the doctoral program Physics
of the Georg-August University School of Sciences (GAUSS)

submitted by

**Hansol Jeon**
from Daejeon, Republic of Korea

Göttingen, 2022

Thesis Committee

**Dr. Stefan Karpitschka**

Interfaces of Complex Fluids
Max Planck Institute for Dynamics and Self-Organization

**Prof. Dr. Marcus Müller**

Institut für Theoretische Physik
Georg-August-Universität Göttingen

**Dr. Isabella Guido**

Faculty of Engineering and Physical Science
University of Surrey

Members of the Examination Board:

**Reviewer:**
**Dr. Stefan Karpitschka**

Interfaces of Complex Fluids
Max Planck Institute for Dynamics and Self-Organization

**Second Reviewer:**
**Prof. Dr. Marcus Müller**

Institut für Theoretische Physik
Georg-August-Universität Göttingen

Further Members of the Examination Board:

**Dr. Isabella Guido**

Faculty of Engineering and Physical Science
University of Surrey

**Prof. Dr. Timo Betz**

Drittes Physikalisches Institut - Biophysik
Georg-August-Universität Göttingen

**Prof. Dr. Ulrich Parlitz**

Biomedical Physics Group
Max Planck Institute for Dynamics and Self-Organization

**Prof. Dr. Philipp Vana, MBA**

Institute of Physical Chemistry
Georg-August-Universität Göttingen

Date of the oral examination: 25.01.2023

# Acknowledgements

First and foremost, thank you Stefan for your guidance through the 4 years of my PhD. I am quite sure it was very tough to supervise a chemist with not so much knowledge in Physics, but you did so very patiently throughout my entire PhD. I learnt a lot from you, and really enjoyed working with you. I hope you will have a blast in Konstanz and I wish your family the very best in the future! Thank you! Also, I would like to thank Dr. Isabella Guido, and Prof. Marcus Müller for their co-supervision throughout my PhD as thesis committee members. Thank you Prof. Philipp Vana, Prof. Timo Betz, and Prof. Ulrich Parlitz for agreeing to be part of my examination board.

Thank you Youchuang for being an awesome colleague and a friend. I will miss our random scientific/non-scientific discussions and your endless supply of fruits! Good luck with your new position in Harbin and don't forget me if you get a Nobel prize! Thank you Prashanth for being a very supportive friend. I always felt so relaxed after talking to you about things in life. I will miss you wandering around the corridors of the institute and randomly dropping by my office/labs! Have fun in Twente and good luck with the rest of your PhD! Thank you Olinka for being a nice office and groupmate! I still remember my first day at the institute and you were very friendly! I miss you and hope you are enjoying your time in Mexico! Thank you Ajinkya for being one of my best friends at the institute. I enjoyed chilling with you at 5pm in your office in the beginning of my PhD! Thank you Jan for being a cool football and gym buddy. I was always amazed by your beer drinking speed! I would also like to thank the other members of my group: Antaran, Franziska, and Maximilian. I will definitely miss everyone! Thank you Kris for your help with microscopes and other instruments, and also for the nice Ludwigstein retreat! Thank you Monika, Guido, Thomas, and Wolf for your help so far. I want to thank the other friends from the institute: Xin, Sebastian, Akinori, Swati, and Michiel. I'm glad that we still keep in touch even years after you leave the institute. Thank you old colleagues and friends who are now in Bayreuth, Rodrigo, Cote, and Alex. Thank you for your hospitality whenever I visit Bayreuth. Thank you Kenny for your awesome barbeque parties and random jokes in the middle of the German class! Thank you friends in the other side of the world-Hyesu, Crystal, Devico, McZingers, Jit Wu, and so on. I miss all of you! Thank you Antoine for being the best person in my life. I am very glad to have met you at this institute. Thank you for your continuous support throughout my PhD and always being there for me.

Last but not least, I want to thank my parents for their endless love and support ever since the day I was born. We went through many tough events in the past two years, but we managed to stay solid as a family and continued to love each other. I dedicate my thesis to them and my grandma, whom I dearly miss.

# Abstract

Dynamic wetting of a liquid deposited on a soft solid is very common in many biological, medical, and industrial processes. Thus, understanding the interaction between a moving liquid drop and a soft surface remains crucial, and yet poorly understood. In this context, this thesis focuses on the wetting dynamics of both biological and simple liquid systems on soft tailored surfaces. To do so, we first develop and produce soft PDMS solids of tunable stiffness with a in-house formulation by using pre-polymers of different molecular weight, and cross-linkers of various silane group concentration. We fully characterise the mechanical properties of our different gels with classical rheological tools. We use such soft PDMS surface as a model system with a stiffness comparable to the brain tissue to study the coalescence of phase separating tau protein droplets. We find that the tau protein droplets behave similarly to viscous liquid droplets and therefore that their coalescence dynamics can be described by using the same scaling law. Beyond the relevance of soft and deformable PDMS surfaces for biological applications, they can also be used to tackle more fundamental questions. For instance, we also address recent controversies on the underlying theoretical description of static and dynamic wetting of soft polymer gels. We present measurements of the shapes of moving wetting ridges obtained with high spatio-temporal resolution, combining different liquid systems on top of different soft PDMS gels. We find that the ridge shapes fail to collapse with the commonly used elastocapillary scaling, but for small normal forces, yields a viable prediction of the the dynamic ridge angles. We demonstrate that neither of the debated theoretical models delivers a quantiative description, while the capillary extraction of an oil skirt appears to be the most promising.

# Table of Contents

# Chapter 1

# Introduction

## 1.1 Motivation

Wetting refers to the behaviour of a liquid in contact with a solid surface and its ability to spread out for example, as a result of the interactions between the liquid and the surface. Wetting is a very ubiquitous phenomenon that can be encountered in many situations ranging from natural phenomena to technological applications. For instance, wetting can be observed for morning dew drops on leaves. It is also particularly relevant in ink-jet printing [1], adhesives [2], coating [3] or even biomedical applications [4]. Due to the recent increasing demand for digital printing and electronic devices, there has been a growing interest in understanding wetting phenomena [5].

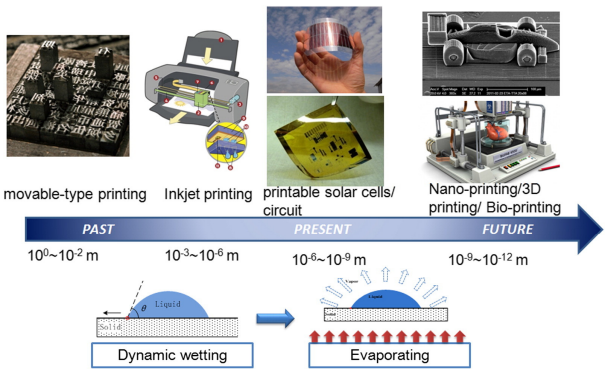


(a)

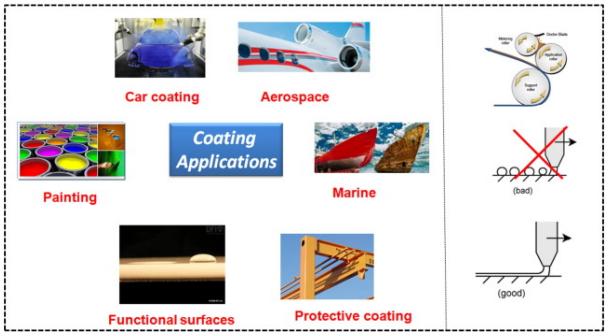


(b)

Figure 1.1: Applications of dynamic wetting in (a) printing techniques and (b) coating industries. Republished with permission from [6]

Static wetting refers to the equilibrium state where the liquid is immobile on a surface, and forms a sessile droplet or a liquid film for example. In contrast, dynamic wetting takes place when the fluid is moving (or spreading) on the solid surface. This scenario is also very common in everyday life and is widely used in various industrial applications such as modern nano, 3d, or bio-printing [6], as illustrated in Figure 1.1 (a). It also significantly affects the coating process in industries such as aerospace, marine, automotive, and so on as shown in Figure 1.1 (b) [6].

Soft solid materials like gels, biological tissues and rubbers respond to a stress by deforming unlike rigid solids. Thus the wetting behaviour of a liquid drop on a soft surface is fundamentally very different from that on a rigid surface. Owing to the early works of Lester [7], Deryagin, *et al.* [8], and Shanahan, *et al.* [9], there have been growing efforts to comprehend the interaction between a liquid drop and a soft surface. Recent developments of microscopic imaging techniques, such as traction force microscopy [10] or X-ray microscopy [11], have allowed researchers to detect the deformation induced by liquids on soft substrates, and have led to a great improvement of our understanding of soft wetting.

Despite such huge potential for biological, medical and industrial applications, fundamental studies on the dynamics of soft wetting are still lacking to this day. With the work presented in this manuscript, we therefore address this issue by investigating the wetting dynamics on soft surfaces.

## 1.2 Objectives

This work focuses on studying fundamental aspects of the dynamics of a contact line on soft surfaces. First of all, it is therefore a question of producing very soft surfaces capable of easily deforming under the action of a contact line induced by classical liquids. We developed a procedure to manufacture tailored soft surfaces using polydimethylsiloxane (PDMS), for which we can tune the stiffness as desired. With such versatile surfaces, we aim to reach three main objectives with this research:

1. We aim to investigate and precisely characterise the mechanical properties of the formulated PDMS gels. The relationship between these properties and the stoichiometric ratio of two reactive functional groups is then discussed. Also, we want to find out how do the stoichiometric ratio and the stiffness of the gel affect the degree of swelling and extraction of the network.

2. We aim to study the coalescence of phase separating tau protein droplets on a soft PDMS surface which can serve as a model system of a soft in-vitro environment. Such phenomenon is particularly relevant to understand the aggregation of these proteins, which are known to cause neuro-degenerative diseases such as Alzheimer's disease.

3. We aim to address recent controversies on the theory of static and dynamic wetting of soft polymer gels through the measurement of the shapes of moving wetting ridges.

## 1.3 Outline of this thesis

In Chapter 2, we discuss fundamental theories necessary for this thesis, from wetting on rigid surfaces to soft solids. Recent debates on the soft wetting are also presented in this chapter.

Chapter 3 describes in details the materials and experimental techniques used for this study. In particular, we explain how to characterise the rheology of PDMS gels and present the different setups used to carry out our experiments.

In Chapter 4, we describe our in-house developed recipe for the formulation of soft PDMS gels, and the results of swelling and extraction experiments of these prepared PDMS samples.

Chapter 5 tackles the coalescence of phase separating tau protein droplets on a soft PDMS substrate that serves as a model system of soft in-vitro environment with similar stiffness as the brain tissues. More precisely, we focus on the dynamics of the liquid meniscus bridging two coalescing droplets. Therefore, we experimentally determine the capillary velocity and compare it to values from the literature.

Chapter 6 presents our work on the experimental visualisation of moving wetting ridges. The dynamic liquid contact angle as well as the rotation and opening angles of the solid wetting ridge are extracted from our experiments. The study of these angles are used to discuss recent contradictions in the theoretical description of static and dynamic soft wetting.

Finally, the conclusion of this work and the possible future perspectives are discussed in Chapter 7.

# Chapter 2

# Surface wetting: theoretical background

## 2.1 Wetting on rigid surfaces

### 2.1.1 Static wetting

Wetting refers to the study of the ability of a liquid deposited on a solid to spread out [12]. When a liquid droplet is resting on a rigid surface, it forms a three-phase contact line of the surface, liquid and air. On the rigid surface, the liquid droplet such as water adopts a characteristic spherical cap shape due to surface tension, as illustrated in Figure 2.1. The origin of this tension can be understood at the molecular level. Liquid molecules in the bulk interact with each other through cohesive forces that keep the molecules close to one another. However, the molecules at the liquid-air interface do not have the same amount of interactions, as there are less number of neighbouring molecules. Therefore they pull each other which creates a tension parallel to the interface: the surface tension. Surface tension, often called $\gamma$, is then a force per unit of length or an energy per unit of area, and thus can be expressed in $\mathrm{N\,m^{-1}}$ or $\mathrm{J\,m^{-2}}$. The spherical shape of water droplet is a result of surface tension that minimises the surface area, and thus the free energy of the droplet.

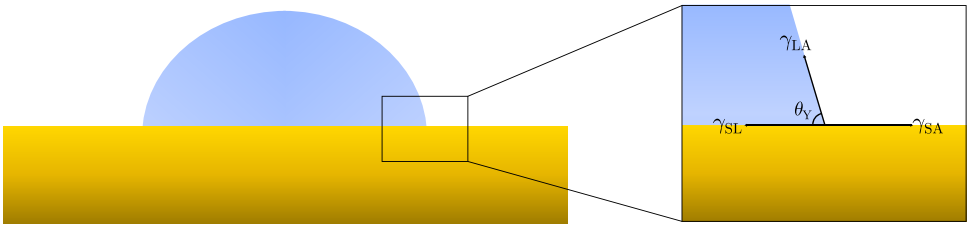


Figure 2.1: Three interfacial tensions, $\gamma_{LA}$, $\gamma_{SL}$, and $\gamma_{SA}$ acting on three-phase contact line of a liquid drop. A liquid drop forms Young's angle $\theta_Y$ with the surface

As sketched in Figure 2.1, there are three different surface (interfacial) tensions acting on the three-phase contact line of a droplet on a surface: liquid-air surface tension $\gamma_{LA}$, solid-liquid interfacial tension $\gamma_{SL}$, and solid-air surface tension $\gamma_{SA}$. These three interfacial tensions form

a force balance that imposes an angle $\theta_Y$ between the liquid and the solid surface, also known as Young's angle [13]. This macroscopic contact angle is usually measured with an optical photograph of a contact region [13]. The force balance at the contact line in the direction parallel to the surface is given the following relation known as Young's equation:

$$\gamma_{SL} + \gamma_{LA} \cos\theta_Y = \gamma_{SA}. \tag{2.1}$$

In 1985, Gennes, *et al.* described two regimes of wetting distinguished by a spreading parameter $S$ that measures the difference between the surface energy per unit area of the substrate below the liquid (wet region) and outside of the liquid (dry region) [12]. The spreading parameter is thus expressed as:

$$S = \gamma_{SA} - (\gamma_{SL} + \gamma_{LA}) \tag{2.2}$$

When $S > 0$, the liquid spreads completely on the substrate, forming a Young's angle of $\theta_Y = 0$. This phenomenon is known as a "complete wetting", as illustrated in Figure 2.2. Partial wetting, which is the most common case and what we will mainly focus on our study, is observed when the spreading parameter is larger than 0. The droplet will form the cap shape with $\theta_Y$ between 0 and $\pi$.

Figure 2.2: Complete wetting of liquid on a solid surface, $\theta_Y = 0$

### 2.1.2 Dynamic wetting

So far, we have discussed the simple case of the static wetting of a drop on a surface, which is described by Young's equation. The question now is: what happens when this liquid drop moves on the same rigid surface?
There are various ways to induce contact line motion such as inflating or deflating an already deposited drop [14], tilting a surface to introduce gravitational effect on the drop [15], or spontaneous spreading of the drop [16].

Let us now consider that the contact line of a drop on a surface is moving at a speed $U$. Figure 2.3 (a) shows the typical evolution of the contact angle as a function of contact line speed $U$. The contact angle here is the dynamic equivalent of the Young's angle for the static case. In this example, Dussan considered that the contact line is advancing if $U > 0$, and receding when $U < 0$ [17]. This evolution of the contact angles proved that the dynamic contact angle of a moving liquid drop depends on the contact line velocity. The contact angle always increases with increasing velocity, i.e. $\partial U/\partial\theta$. This first example shows that the dynamics of a moving drop requires a more complex description and that Young's equation no longer applies to this dynamic system [17, 20].

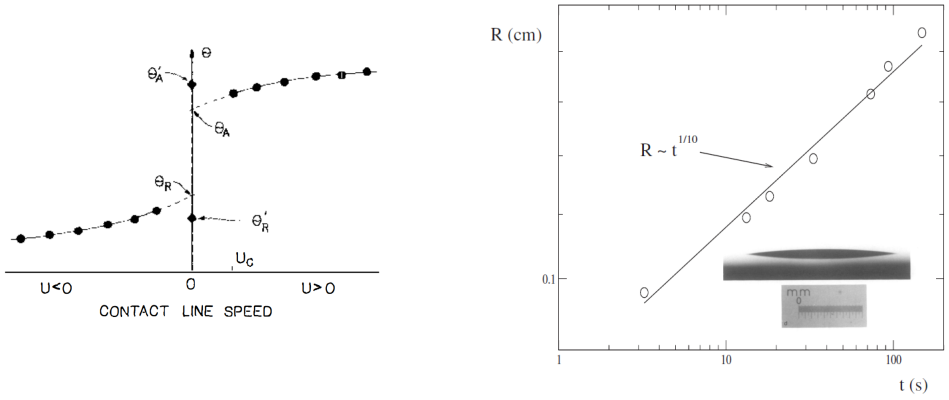


(a) (b)

Figure 2.3: (a) Evolution of advancing $\theta_A$ and receding $\theta_R$ contact angles as a function of contact line speed. Republished with permission from [17] (b) Radius of a spreading silicone oil drop as function of time described by Tanner's law. Republished with permission from [18]. Inset: An image of a silicone oil drop spreading on a glass substrate. Republished with permission from [19]

Contact line motion can also be induced when a liquid drop is deposited on a solid surface. The drop actually spreads and its contact angle decreases until it reaches an equilibrium contact angle $\theta_{eq}$. Due to its ubiquity in nature and in technological applications, there have been numerous experimental and theoretical studies to understand the spreading of drops on surfaces [17, 19, 21, 22]. Figure 2.3 (b) shows a silicone oil drop spreading on a glass surface and the evolution of its radius as a function of time. The radius of the silicone oil drop increases over time before reaching complete wetting of the glass substrate at equilibrium, for which $\theta_{eq} = 0°$. The temporal evolution of the droplet radius follows a power law with an exponent 1/10. Such power law dependence of radius of a droplet spreading on a surface is known as Tanner's law and is given by [21]:

$$R(t) \propto t^n. \tag{2.3}$$

The exponent $n = 1/10$ arises when the droplet radius $R$ is smaller than the capillary length $\ell_c$ ($\ell_c = \sqrt{\gamma/\rho g}$ when $\gamma$ is the liquid surface tension, $\rho$ is the liquid density, and $g$ is the gravitational accelaration). The driving force of this spreading drop is its surface tension and the energy dissipation occurs at the contact line [23].

Tanner's law shows that the spreading rate of a drop does not depend on the available surface energy [18]. To explain such power law dependence with very small exponent $n$, the rate of energy dissipation needs to be considered near the contact line [18]. It was found that the rate of energy dissipation increases very rapidly near the contact line, leading to a divergence of energy dissipation [24]. The basis of energy dissipation of a moving contact line on a rigid surface is discussed in two separate theories: hydrodynamic and molecular-kinetic theories [24, 25, 12, 18]. These theories give rise to different scaling exponent $n$. The detailed explanation of these two different theories is out of scope of this thesis, and will not be discussed further.

## 2.2 Wetting on soft surfaces

So far, we have presented the wetting of liquid drops on idealised (rigid) surfaces. However, many surfaces such as biological tissues are actually soft. The wetting behaviour of a liquid droplet on a soft surface differs from that on a rigid surface due to the ability of the soft solid to deform. In this section, we will first introduce the basic elements of elastic and viscoelastic theory needed to describe the deformation of a soft surface. Then we will discuss the characteristic wetting behaviour on such soft surfaces in both static and dynamic scenarios.

### 2.2.1 From purely elastic to viscoelastic materials

#### Elastic theory

The ability of a soft solid to deform under an applied force and to regain its original shape is known as elasticity.

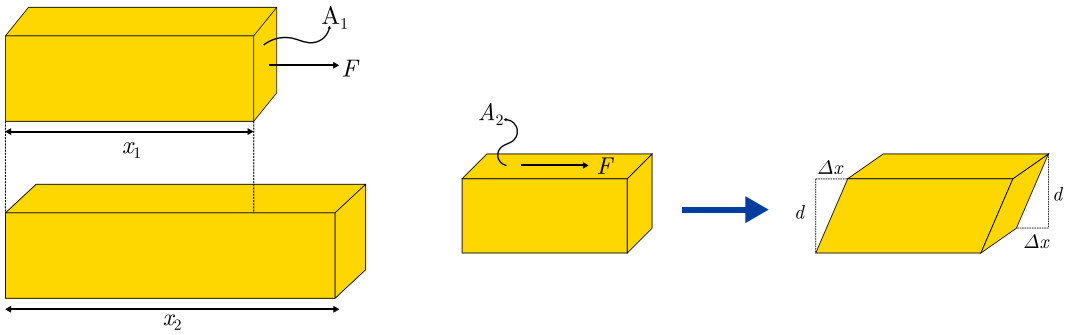


Figure 2.4: Schematic representation of the deformation of a purely elastic solid (a) under a given force $F$ acting normally to its cross-section and (b) under a shear force

Let us consider here an incompressible, and deformable solid of initial length $x_1$ and cross-section $A_1$. For example, this solid can be elongated to a final length $x_2$ under the action of a force $F$ as illustrated in Figure 2.4 (a). The resulting strain ($\varepsilon$), which is a dimensionless quantity that refers to the relative deformation/elongation due to the applied force, is expressed as:

$$\varepsilon = \frac{(x_2 - x_1)}{x_1} \tag{2.4}$$

The stress $\sigma$ is the resistance of an object to an applied force that could tear it apart. When a force is applied to an incompressible solid, the cross-sectional area $A_1$ will change to compensate the change in length. The stress corresponds to the force by unit of area and has the dimension of a pressure (expressed in Pa). In our example, the corresponding stress is defined as:

$$\sigma = \frac{F}{A_1}. \tag{2.5}$$

The Young's modulus $E$ describes how easily can a material be stretched or deformed and is defined as the ratio of the stress and the strain:

$$E = \frac{\sigma}{\varepsilon}. \tag{2.6}$$

So far, we have just considered the case of an elongated object, for which the force acts perpendicularly to the cross-section. However the force $F$ can also be applied parallel to the surface as represented in Figure 2.4 (b), which is called shearing. In this case, the solid of thickness $d$ deforms sideways with a horizontal displacement $\Delta x$. The resulting shear strain $\gamma$ is a dimensionless quantity expressed as:

$$\gamma = \frac{\Delta x}{d}. \tag{2.7}$$

The shear stress $\tau$ corresponds to the applied shear force $F$ by unit of area. Contrary to the previous case of stretching, the cross-section to consider here is the one parallel to this force, called $A_2$. The shear stress is then given by:

$$\tau = \frac{F}{A_2} \tag{2.8}$$

To quantify the elastic stiffness of a material, the shear modulus $G$ is commonly used, in rheometers for example, and is defined as:

$$G = \frac{\tau}{\gamma} \tag{2.9}$$

The shear modulus has then the dimension of a pressure and is expressed in Pa. The larger the value of the shear modulus, the stiffer the material.

### Stress-strain relationship

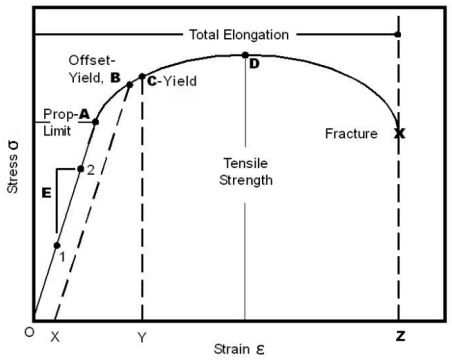


Figure 2.5: Exemplary stress $\sigma$-strain $\varepsilon$ curve of a material. The slope of the curve corresponds to the elastic modulus $E$ of the solid. Source: www.linearmotiontips.com

The stress-strain relationship of a material provides information on its elastic behaviour. Figure 2.5 shows a typical stress-strain diagram of a solid material. For a low stress applied to the

material, there is a linear relationship between stress and strain up to point A, known as proportional limit. Such linear relationship is described by Hooke's law, and the slope of the curve correspond to the Young's (or elastic) modulus of the material, defined as $E = \sigma/\varepsilon$. Until this limit, the deformed material can still recover its original shape once the force is released. From point C, known as a yield point, the strain increases more significantly than the stress, and the deformed material can no longer go back to its original shape even after the release of the force. The largest stress (or tensile strength) is reached at point D, beyond which a further stretching of the material will tear it apart (fracture).

### Viscoelastic models

Although some materials can be analysed only in terms of pure elasticity, most of the materials such as biological tissues or cells are rather viscoelastic [26]. A viscoelastic material, as self-explanatory, combines the characteristics of both an elastic solid and a viscous liquid. We will briefly introduce some theoretical elements used to describe a viscoelastic material in this section.

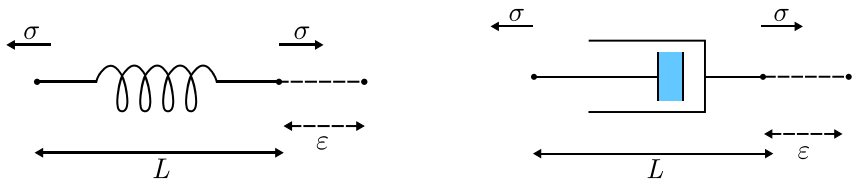


Figure 2.6: Sketch of (a) a spring that represents a perfectly elastic solid and (b) a dashpot that describes a purely viscous liquid. These two elements displace by a relative distance $\varepsilon$ under an applied stress $\sigma$.

The elastic component of a viscoelastic material is usually represented as a simple spring, as illustrated in Figure 2.6 (a). As we described in the previous section, the deformation of a purely elastic solid follows Hooke's law which in this case is given by:

$$\sigma = G \cdot \varepsilon, \tag{2.10}$$

where $\sigma$ is the the applied stress, $\varepsilon$ is the strain and $G$ is the spring constant, which corresponds to the elastic modulus of the spring.

In contrast, the purely viscous component of a viscoleastic material is represented by a dashpot filled with liquid, as shown in Figure 2.6 (b). Such dashpot follows Newton's law of viscosity:

$$\sigma = \eta \cdot \dot{\varepsilon}, \tag{2.11}$$

where $\eta$ is the viscosity of the liquid and $\dot{\varepsilon}$ is the strain rate.

By combining these two basic elements, a spring and a dashpot, several models are thus available to describe the behaviour of a viscoelastic material. The two well-established models

are Kelvin-Voigt and Maxwell models.

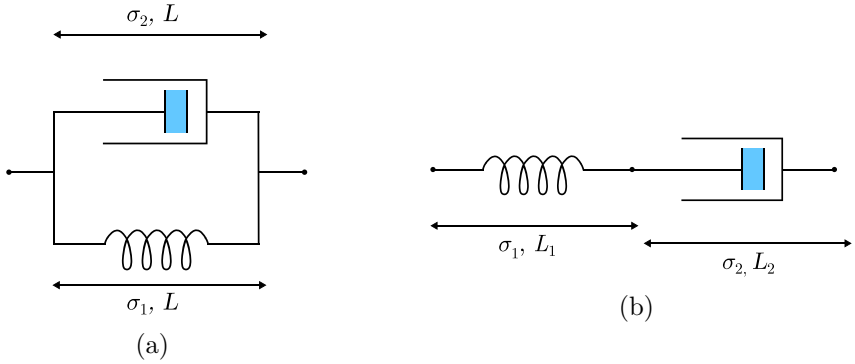


Figure 2.7: The two most commonly used models to represent a viscoelastic solid: (a) the Kelvin-Voigt model and (b) the Maxwell model. These models are obtained when a spring and a dashpot are connected in parallel and in series, respectively.

The Kelvin-Voigt model is obtained by connecting a spring and a dashpot in parallel, as illustrated in Figure 2.7 (a). The corresponding strain and stress are given by:

$$\varepsilon = \varepsilon_1 = \varepsilon_2 \tag{2.12}$$

$$\begin{aligned} \sigma &= \sigma_1 + \sigma_2 \\ &= G \cdot \varepsilon + \eta \cdot \dot{\varepsilon} \end{aligned} \tag{2.13}$$

When a constant stress ($\dot{\sigma} = 0$) is applied suddenly on a Hookean solid, the solid reaches its maximum deformation immediately. In contrast, a viscoelastic material exhibits a creep behaviour, for which the solid gradually reaches its maximum deformation over a certain period of time. In the Kelvin-Voigt model, the deformation reaches equilibrium exponentially with a characteristic time $\tau = \eta/G$.

On the other hand, the Maxwell model is obtained when a spring and a dashpot are connected in series, as shown in Figure 2.7 (b). The total strain is additive, and the stress over the elements is the same:

$$\varepsilon = \varepsilon_1 + \varepsilon_2 \tag{2.14}$$

$$\begin{aligned} \sigma &= \sigma_1 = \sigma_2 \\ &= G \cdot \varepsilon_1 = \eta \cdot \dot{\varepsilon}_2 \end{aligned} \tag{2.15}$$

In a Newtonian fluid such as water, the stress disappears immediately once the flow stops (i.e. the strain $\varepsilon$ is constant and thus $\dot{\varepsilon} = 0$). However, for a viscoelastic material, the stress gradually relaxes over a relaxation time $\tau$ even after the flow has stopped.

The Kelvin-Voigt model shows that the strain approaches a constant value at infinite time limit while the Maxwell model describes a lienar relationship between the strain and the time. Thus, the Kelvin-Voigt model describes the creep behaviour of a viscoelastic material better than the Maxwell model does.

In the Maxwell model, the stress relaxes exponentially and reaches an equilibrium at infinite tie limit. However, this is not the case in the Kelvin-Voigt model, as the stress relaxes immediately without any retardation. Therefore, the Maxwell model is more effective to depict the stress relaxation behaviour of a viscoelastic material.

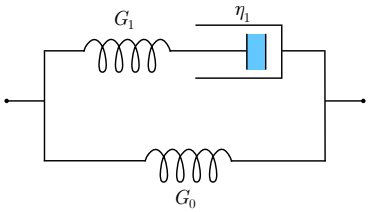


Figure 2.8: Sketch of a Standard Linear Solid used to model viscoelastic materials. A Maxwell model is connected in parallel with another spring of stiffness constant $G_0$

A Standard Linear Solid (S.L.S.), as depicted in Figure 2.8, represents a more comprehensive model that captures both creep and stress relaxation behaviours of viscoelastic materials. The model consists of a Maxwell solid in parallel with a spring. The strain and stress relationships for this model is thus given as:

$$\varepsilon = \varepsilon_0 = \varepsilon_M \tag{2.16}$$

$$\sigma = \sigma_0 + \sigma_M \tag{2.17}$$

$$\sigma = G_0 \cdot \varepsilon_0 + \sigma_M$$

where $\varepsilon_M$ and $\sigma_M$ are the strain and stress of the Maxwell element respectively.

We see that any model containing a viscous component, described by a dashpot, involves an exponential relaxation process for a creep or a stress relaxation. However this is not necessarily the case for PDMS silicone networks, which are probably the most extensively used viscoelastic materials in the study of soft wetting. These networks are formed via polymerisation of small pre-polymers of different functional groups (by mixing a base polymer with a cross-linker). A reticulated PDMS network does not have any liquid phase trapped inside, and thus it does not necessarily obey an exponential relaxation function [27], as described previously for the different models. It rather follows a power-law response function expressed as:

$$\mu(t) = \mu \left[1 + \Gamma(1-n)^{-1} \left(\frac{\tau}{t}\right)^n\right], \tag{2.18}$$

where $\mu$ is a shear modulus, $\Gamma$ is a gamma function, and $1/2 \leq n \leq 2/3$ (depending on the base polymer to cross-linker ratio) [27].

A proper rheological characterization of soft viscoelastic PDMS solids can therefore be obtained with such models, which remains crucial to understand the complex dynamic of soft wetting.

### 2.2.2 Static wetting on soft surfaces

#### Elasto-capillary length

We have already discussed the effect of surface tension on the shape and the wetting of a liquid droplet resting on a rigid surface in Section 2.1.1. We will now focus on what happens when the surface is soft.

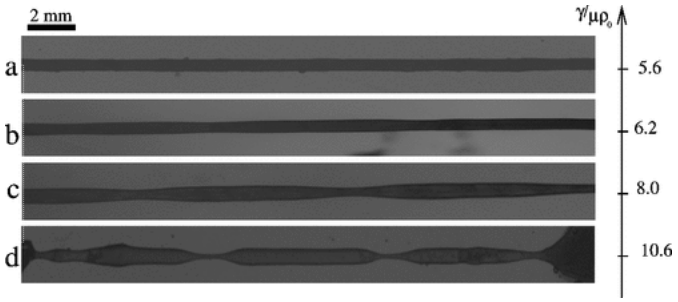


(a)

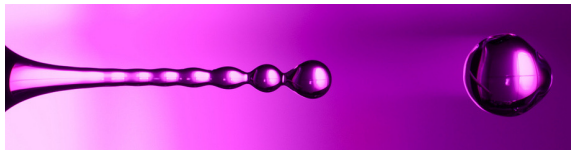

(b)

Figure 2.9: (a) Rayleigh-Plateau instability of cylinders of agar gels immersed in toluene. Republished with permission from [28]. (b) Rayleigh-Plateau instability typically observed for a water column flowing out of a faucet. Source: https://fyfluiddynamics.com

Let us consider here a soft viscoelastic solid in contact with a liquid. Is surface tension still a relevant parameter in the case of such deformable surface? Or should we only consider the mechanical properties of the soft surface?
Recent literature showed that the solid surface tension (between the liquid and the solid surface) indeed affects the shape of soft viscoelastic cylinders of agar gels immersed in toluene [28]. A tendency of the liquid to minimise its surface area with its surface tension as a driving force breaks the stream of water into smaller droplets. Such unstable nature of a liquid jet is known as the Rayleigh-Plateau instability. In Figure 2.9 (a), we can see that these viscoelastic cylinders exhibit a Rayleigh-Plateau instability, very similar to what one could observe for a stream of water flowing from a faucet (see Figure 2.9 (b)). The instability in the viscoelastic cylinders rises when the Laplace pressure overcomes the elastic forces of the gel. Such competition between these two forces, capillary and elastic, can be expressed by a ratio of surface energy to elasticity, which is expressed as "$\gamma/\mu\rho_0$" in Figure 2.9 (a). Here $\gamma$ is the gel/toluene surface tension, $\mu$ is the shear modulus of the gel and $\rho_0$ is the radius of the cylinder. The larger the ratio, the more viscous the material is, and the smaller the ratio, the more elastic the material is. As can be observed in Figure 2.9 (a), more viscous gels deform more than the elastic ones.

Bearing in mind that there exists a competition between capillarity and elasticity for a soft material, let us now revisit the equilibrium wetting configuration from Figure 2.1.

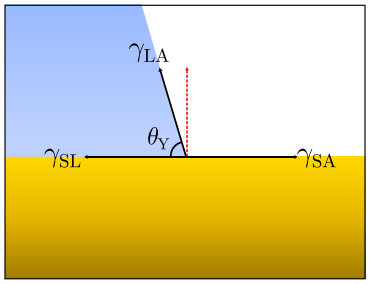


Figure 2.10: Schematic drawing of a liquid droplet on a surface. Three interfacial tensions act on the solid-liquid contact region. The red arrow indicates the vertical force component of the liquid surface tension $\gamma_{LA}$.

Previously, we only considered the force balance in the direction parallel to the surface (see Equation 2.1). Yet, the liquid-air interfacial tension also contains a vertical force component $\gamma_{LA} \sin\theta_Y$ represented by the red arrow in Figure 2.10. There exists a balance of capillary and elastic forces of the surface. This balance is represented by the elasto-capillary length ($\ell$):

$$\ell = \frac{\gamma_{LA} \sin\theta_Y}{G}, \tag{2.19}$$

where $G$ is a solid shear modulus of the solid surface and $\theta_Y$ the Young's angle.

Surfaces such as glass have a typical shear modulus of a few hundred GPa, and thus the elastocapillary length is in the order of pm and nm. For these surfaces, the elasto-capillary length is significantly smaller than their thickness (typically of mm to cm), and thus we will not observe any surface deformation. They are categorised as the "rigid surfaces". In contrast, solids such as polymer gels have a shear modulus of few Pa to few kPa in magnitude, and thus the corresponding elastocapillary length is in the µm to mm range. These surfaces are known as the "soft surfaces". Due to the relatively larger elasto-capillary length, a deformation of the soft surface at the three phase contact line can be observed, and is commonly known as the "wetting ridge".

### The wetting ridge

Lester, and many others in the 1960s and 1980s, discussed the existence of a vertical force balance at the contact line of a drop deposited on a soft solid surface [7, 30, 9]. They assumed that soft solids deform into a sharp wetting ridge due to the presence of a point force acting at the tip of the ridge [7] as described in Figure 2.11 (a). With such assumption, Carré, *et al.* obtained a theoretical profile of the wetting ridge [29] given by :

$$h(x) \approx \frac{\gamma_{LA} \sin\theta_{eq}}{2\pi G} \ln\left(\frac{d}{x}\right), x > \varepsilon, \tag{2.20}$$

where $h(x)$ is the vertical displacement of the wetting ridge, $\theta_{eq}$ is the liquid contact angle, $G$ is the shear modulus of the soft surface, $x$ is the distance from the three phase contact line, and $d$ is the distance along the surface tension $\gamma_{LA}$. The cut-off distance $\varepsilon$ will be discussed in the next paragraph.

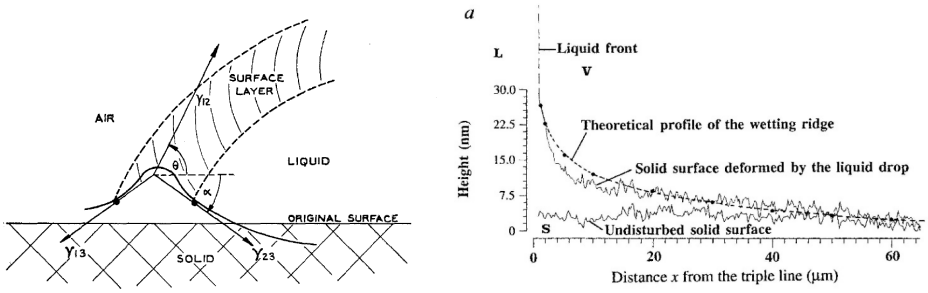


(a) (b)

Figure 2.11: (a) Schematic description of a wetting ridge with a point force ($\gamma_{12} \sin\theta$) acting at the tip. Republished with permission from [7]. (b) Surface topology of soft elastomer substrate (Elastic modulus= 0.63 MPa) obtained by interferometric microscopy. Republished with permission from [29]

To confirm this theoretical surface profile, they also investigated the topology of the wetting ridge by using an interferometric microscopy (Figure 2.11(b)), and obtained a good agreement between the experimental and theoretical profiles.

Let us now have a closer look at the Equation 2.20. The vertical displacement $h(x)$ is clearly depends logarithmically on the a horizontal distance $x$ from the contact line. This implies that the surface deformation $h(x)$ should be infinite for $x = 0$, i.e. there is a singularity at the contact line. Such singularity was resolved by Carré by assuming that $x$ is larger than a cut-off distance $\varepsilon$, a few nanometers away from the triple line. However, such cut-off distance away from the contact line has left an ambiguity regarding the actual shape of the wetting ridge tip.

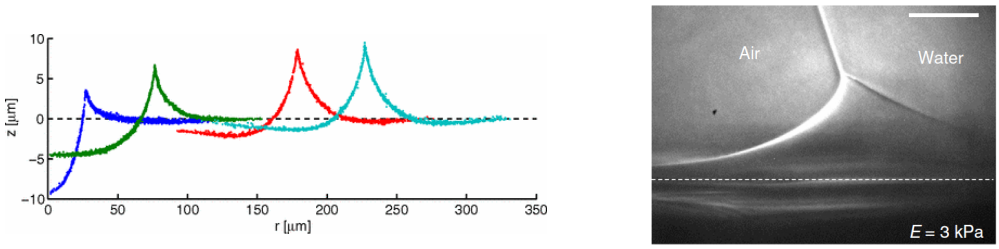


(a) (b)

Figure 2.12: (a) Surface profiles of a soft silicone gel substrate deformed by glycerol droplets of different radii. From left to right: glycerol droplet radii of 26.8, 74.5, 176.7, and 225.5 μm. Republished with permission from [10]. (b) X-ray image of the wetting ridge formed by a water droplet on a silicone gel of Young's modulus 3 kPa. Scale bar= 5 μm. Republished with permission from [11]

More recently, there have been many efforts to resolve the tip of the ridge. As displayed in Figure 2.12 (a), Style, *et al.* recorded the deformation of a soft surface by embedding fluorescent beads on the surface and tracking their positions using a laser confocal microscopy [10]. Also, Park, *et al.* successfully obtained a high-resolution image of the sharp asymmetric ridge tip with X-ray microscopy, as shown in Figure 2.12 (b). Both images show a sharp tip of the wetting ridge (with a finite amplitude) at the contact line, and they prove that the shape of the ridge

tip is determined by the balance of three interfacial tensions not just in the horizontal direction, but also in the vertical direction. Also, they give a direct experimental proof that this force balance resembles the Neumann balance. This points to the possibility that the solid surface of the gel has a surface tension similar to liquids.

The triangle of the three interfacial tensions was first introduced by Neumann in 1894 [31], and is now being called as the Neumann's triangle. This condition always satisfies when there is a three-phase contact line with an equilibrium [7].

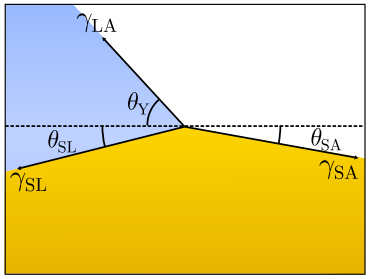


Figure 2.13: Schematic description of the Neumann balance of three surface tensions ($\gamma_{LA}, \gamma_{SL}, \gamma_{SA}$) at the tip of wetting ridge

Figure 2.13 describes the Neumann balacne of the three surface tensions acting at the tip of a wetting ridge. Using the angles imposed by these surface tensions, we can derive the following force balance:

$$\gamma_{LA} \cos\theta_Y = -\gamma_{SL} \cos\theta_{SL} + \gamma_{SA} \cos\theta_{SA} \tag{2.21}$$

$$\gamma_{LA} \sin\theta_Y = \gamma_{SL} \sin\theta_{SL} + \gamma_{SA} \sin\theta_{SA}. \tag{2.22}$$

### 2.2.3 Dynamic wetting

#### Viscoelastic braking

The dynamic wetting behaviour of a liquid droplet moving on a rigid surface is determined by dissipation of energy within the liquid droplet [32]. On the other hand, wetting on soft surfaces is mainly dominated by energy dissipation within the soft substrate [33]. Carré, *et al.* observed that a liquid droplet actually moves slower on a soft surface than on a rigid surface due to such dissipation.

This behaviour can be illustrated in Figure 2.14 (a) which shows the velocity of a low volatility liquid *o*-tricresyl phosphate (*o*-TCP) running down on PDMS substrates of different Young's modulus (called $\Upsilon$ in [33], but will be indicated as $E$ in this thesis to avoid confusion). The velocity of the liquid drop is higher when the Young's modulus of the substrate is larger [33]. By investigating the spreading of *o*-TCP on a soft elastomer surface (see Figure 2.14 (b)), the same authors showed that the contact angle ($\theta(t)$) decreases with the spreading speed $U$ [29]. They found that the contact angle can be described as power law of the liquid spreading speed. By using an energy balance involving both viscous and viscoelastic dissipation, they

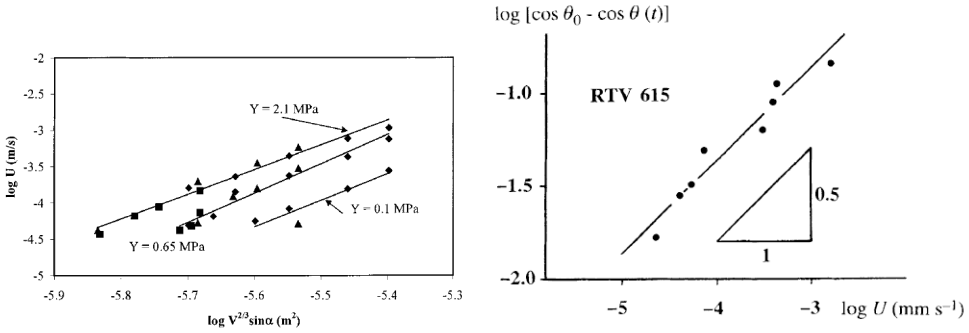


(a) (b)

Figure 2.14: (a) Speed $U$ of o-TCP drops of different volume V running down PDMS surfaces of different Young's modulus $\Upsilon$. Square: $V = 3\,\mu L$, triangle: $V = 5\,\mu L$, diamond: $V = 8\,\mu L$. Republished with permission from [33] (b) Evolution of contact angle $\theta(t)$ of o-TCP spreading on a silicone RTV 615 surface as a function of spreading speed $U$. Expressed in logarithmic scale. Republished with permission from [29]

obtained an equation that explains the spreading of the liquid:

$$\cos\theta_0 - \cos\theta(t) = \frac{3\eta l U}{\gamma\theta(t)} + \frac{\gamma}{2\pi G\varepsilon}\left(\frac{U}{U_0}\right)^n, \tag{2.23}$$

where $U_0$ and $n$ indicate the damping properties of the solid, with $n$ being typically less than 1. $\eta$ is the viscosity of the liquid, and $l$ is a logarithmic factor [29].

The right hand side of Equation 2.23 contains two main terms: the first one represents the viscous dissipation within the liquid, and the second term indicates viscoelastic dissipation. At low contact line speeds $U$, the second term dominates the behaviour of the contact angle, whereas the viscous dissipation is more dominant at high speeds. Comparing to their experiments on the o-TCP droplet spreading on the PDMS surface, they concluded that dissipation within the viscoelastic substrate governs the dynamics of liquid contact line at low velocity [29].

## 2.3 Wetting on real soft surfaces

From the previous section, we learnt that a sharp wetting ridge is formed by a drop on a soft surface due to the vertical component of the liquid surface tension and that a force balance acts at the tip of this ridge. However, the theories we discussed in the case of idealised soft surfaces do not completely capture the wetting behaviours on real soft surfaces. In this section, we will describe several studies on properties of a commonly used material, a polydimethylsiloxane (PDMS) gel.

### 2.3.1 PDMS

Polydimethylsiloxane (PDMS) is an inorganic polymer as its backbone consists of silicon instead of carbon atoms. It therefore also known as silicone elastomer. PDMS is widely used in domestic products such as sealants, cosmetics and baking moulds [34]. It is chemically inert, isotropic and

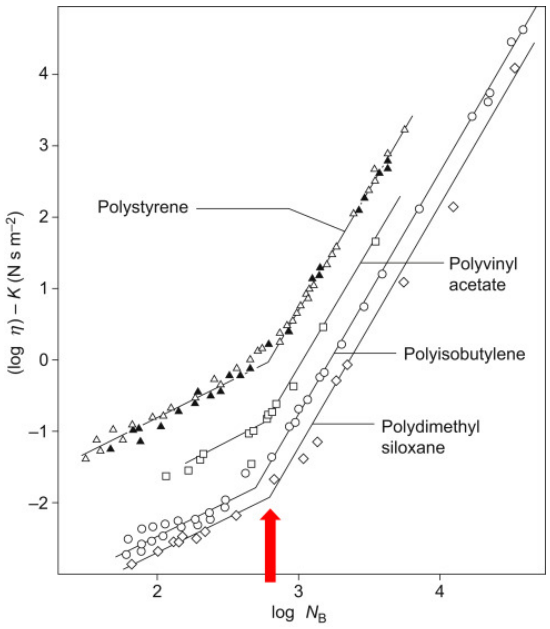


Figure 2.15: Viscosity $\eta$ of different polymer melts as a function of their molecular weight $N_{\mathrm{B}}$. The red arrow indicates an entanglement threshold. Republished with permission from [36]

homogeneous, optically transparent and can easily attach to surfaces like glass. Such properties of PDMS makes it compatible with optical and fluorescent microscopy [35].

### Dependence on Molecular weight

The flow behaviour of polymers of low molecular weight differs from those of high molecular weight. The viscosity of lower molecular weight polymers does not depend on the shear rate, and thus these polymers behave like a Newtonian fluid [37]. On the other hand, when the polymers have a higher molecular weight, the viscosity decreases with the shear rate i.e. the polymers exhibit a shear-thinning behaviour [37].

Figure 2.15 shows the viscosity of different types of polymer melts, including PDMS, as a function of their molecular weight. The viscosity of these polymers at zero shear rate was estimated to resolve the pure molecular weight dependence of the viscosity. As we can see, the viscosity is proportional to the molecular weight for all types of polymers until a certain indicated by the red arrow in the Figure 2.15. This red arrow indicates an entanglement threshold, above which the polymer chains start to entangle. The viscosity then increases according to power law above this threshold [36]. The entanglement of polymer chains refers to the state when the polymer molecules in a melt are surrounded by other long molecules that restrict their motion in response to a deformation. In high molecular weight polymers (above entanglement molecular weight), the motion of the polymer chain is disturbed by large entanglements, leading to a significant increase in zero shear viscosity.

PDMS networks are formed by mixing a base polymer and a cross-linker. Changing the mixing ratio of these two ingredients, or changing their molecular weight, affects the mechanical property of final PDMS network.

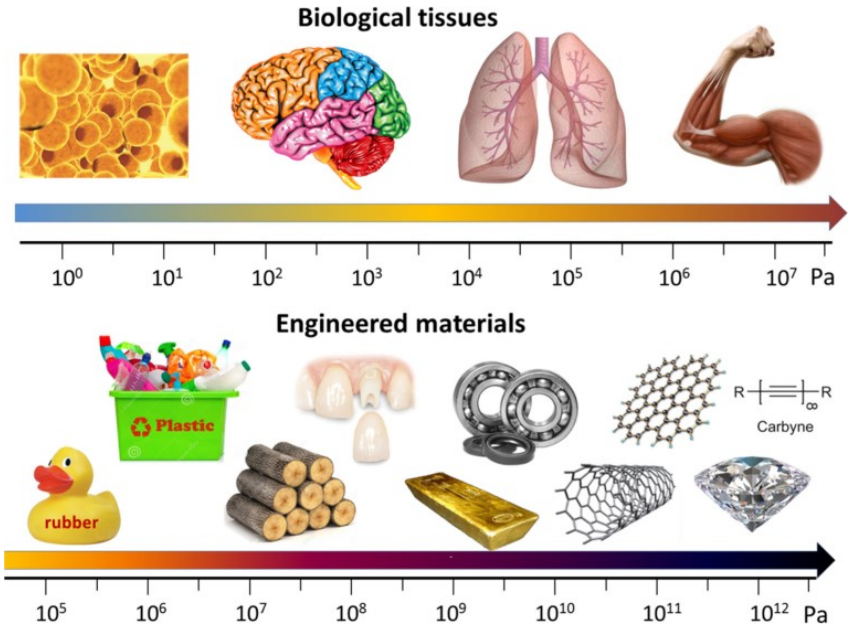


Figure 2.16: Elastic modulus of different common materials. The larger the elastic modulus, the stiffer the material. Republished with permission from [38]

Figure 2.16 shows the elastic modulus of different objects of everyday life. The elastic modulus quantifies the resistance of a material to an elastic deformation when a stress is applied as explained in Section 2.2.1. So the higher the elastic modulus, the stiffer the material. Biological tissues are very soft with an elastic modulus that can be as low as a few Pa. It is widely known that we can formulate PDMS networks with various elastic moduli [34]. Such flexibility to tune the stiffness of PDMS networks makes it a very attractive and versatile material to use as a surface for the study of soft wetting.

### 2.3.2 Shuttleworth effect

As already discussed in the Section 2.2.2, a liquid droplet wetting on a soft surface can deform the surface.

Any type of interface is characterised by a surface energy $\gamma$, which corresponds to an excess free energy per unit of area expressed in J/m$^2$ [39]. This gives rise to a surface tension $\Upsilon$, which is the excess force per unit length of the interface in N/m [40]. For a liquid, the surface energy $\gamma$ and the surface tension $\Upsilon$ are identical, i.e. $\gamma = \Upsilon$ [41]. In contrast, for an elastic solid, this is not the case. A stretching of its surface can alter its local physical chemistry, leading to a change in its solid surface tension [42], which is known as the Shuttleworth effect [43].

The change of the surface energy of the interface with an area $A$ due to the strain $\varepsilon$ parallel to the surface is expressed as:

$$\delta(\gamma A) = \left(\gamma + A\frac{d\gamma}{dA}\right)\delta A \tag{2.24}$$

$$= \left(\gamma + \frac{d\gamma}{d\varepsilon}\right)\delta A, \tag{2.25}$$

Both surface stress and surface energy are strain dependent. This leads to the so-called Shut-

tleworth relation:

$$\Upsilon = \gamma + \frac{d\gamma}{d\varepsilon}. \tag{2.26}$$

The Shuttleworth effect gave rise to a debate about the validity of Neumann's law at the wetting ridge of a soft surface [42]. This will be further discussed in Section 2.4.1.

### 2.3.3 Poroelasticity

A cross-linked polymer network is well-known to be an incompressible material that does not change in volume when deformed. When this elastic polymer network is placed into a solvent, it absorbs quite a large amount of solvent, owing to the entropy of mixing [44]. Such flow of liquid in and out of the network leads to a change in volume (i.e. a compressibility). Swelling or shrinking of the network occurs with the migration of fluid. The interplay between such fluid exchange and the deformation of an elastic network is called poroelasticity, which was first introduced by M. A. Biot in 1941 to explain soil consolidation [45].

Recently, it has been found that the flow of liquid within polymer networks affects wetting on a poroelastic surface. Zhao, *et al.* observed a logarithmic growth of the ridge height as the liquid moves towards the wetting ridge [46]. Xu, *et al.* measured the relaxation of a wetting ridge during a de-wetting process via interferometric imaging to observe the contribution from both viscoelastic and poroelastic dissipation. They found that viscoelasticity is more dominant at shorter timescales or for smaller droplets, while poroelastic contribution dominates the dynamics for larger droplets or longer timescales [47]. Hourlier-Fargette, *et al.* corroborated the existence of a poroelastic contribution by quantifying the extraction of a solvent (free oligomers) from an elastomer surface due to a moving liquid contact line and showing that such extracted solvent decreases the droplet surface tension [48].
The extraction of solvents by a contact line will be further discussed in the next section.

### 2.3.4 Extraction of solvents by a contact line

#### Effect of uncross-linked polymer chains

Hourlier-Fargette, *et al.* studied the dynamics of a moving droplet of water/glycerol on both untreated and toluene-treated PDMS surfaces, for which toluene removes the uncross-linked polymer chains from the PDMS network. Figure 2.17 (a) shows the evolution of a droplet sliding down a vertical PDMS surface. For this untreated surface, two distinct regimes (I and II) of droplet velocity are observed. At first the droplet slides down at moderate velocity (regime I) and then faster (regime II), and this for different droplet volumes. Several reasons can be responsible for this sudden change in droplet speed, such as droplet shape bistability or a modification of the droplet composition [48].
In comparison, when a droplet was deposited on a toluene-treated PDMS sample, only regime I was observed for the droplet velocity (see figure 2.17 (b)). The re-swelling of a treated sample with silicone oil led to recovery of the two droplet velocity regimes. Such result shows that the presence of uncross-linked oligomer chains influences the two-regime behaviour of droplet observed on untreated PDMS sample [48]. So how do these uncrossed-linked chains affect the velocity of a droplet moving on a surface?

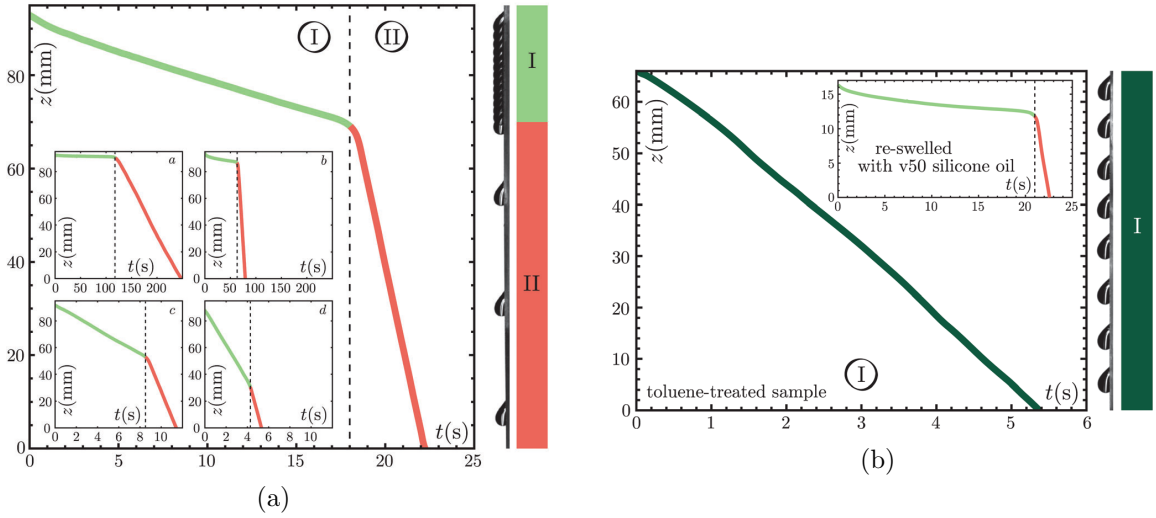


Figure 2.17: (a) Vertical distance $z$ travelled by a 40%/60% water/glycerol mixture droplet of volume 21.5 µL deposited on an untreated PDMS surface. Two different regimes of droplet velocities are observed. Inset: same experiment for droplets of different volume. (b) Vertical distance $z$ travelled by a 40%/60% water/glycerol mixture droplet of volume 21.5 µL deposited on a toluene-treated PDMS surface. Only one speed regime of the droplet is identified. Inset: the two speed regimes of the droplet are recovered after re-swelling the treated PDMS surface. Republished with permission from [48]

To answer this question, the authors then measured the surface tension of collected water-glycerol drops, after sliding down the two different PDMS surfaces as a function of the collected volume. They found that the surface tension of droplets that have slid on an untreated surface decreases dramatically with the collected droplet volume, from $V \approx 3\,\text{mL}$, and then saturates at higher volumes (see Figure 2.18 (b)). This sudden decrease of surface tension indicates the presence of a silicone oil film starting to form at the liquid-air interface [48]. As a droplet slides downs on the PDMS surface, it harvests the free oligomers that lower the surface tension of the liquid drop. Therefore the bigger the droplet, the more harvested oligmers and thus the lower the surface tension. For a high volume, the droplet surface is fully covered by a silicone oil film and thus the surface tension saturates. This mechanism also explains that the surface tension does not vary significantly with the volume for droplets sliding on a treated surface, as very few free oligomers are still present.
They confirmed the possibility of such mechanism by considering different droplets of given water-glycerol composition and by measuring their surface tension before and after deposition on an untreated PDMS surface (see Figure 2.18 (d)). They observed that the surface tension of a given droplet systematically decreases after sliding the surface. They argued that the silicone oil gradually covers the droplet surface as it rolls down the untreated PDMS surface, leading to this sudden decrease of surface tension.

We now can understand how the extraction of uncrossed-linked oligomers by a moving drop can affect the surface tension of this drop. Of course, this also affects the wetting dynamics on a soft surface and, for instance, allows to account for the change in velocity of a sliding drop presented in Figure 2.17.

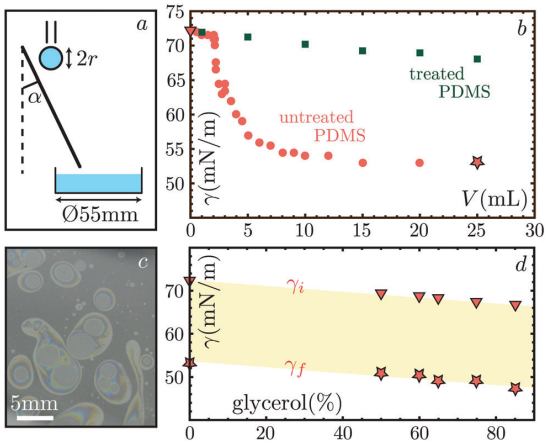


Figure 2.18: (a) Sketch of a liquid drop sliding down a PDMS surface, inclined with an angle $\alpha = 29.2°$. The droplet radius is $r = 2\,\text{mm}$. (b) Surface tension of water droplets collected after their descent on an untreated PDMS surface (red circles), and on treated PDMS surface (green circles). (c) Image of the surface of collected water droplets of volume 33 µL after sliding down the untreated PDMS surface. (d) Initial and final surface tension $\gamma$ of water/glycerol mixture droplets of different composition before and after their descent on untreated PDMS surface. Republished with permission from [48]

### Phase separation in the wetting ridge

As we just saw, the presence of free oligomers at a PDMS surface can modify the surface tension of a moving drop. However, these uncrossed-linked chains can also directly affect the wetting ridge.

Cai, *et al.* observed a fluid separation at the contact line of a soft PDMS network swollen with low molecular weight trimethylsilioxy-terminated silicone oil [49]. To visually differentiate the swelling silicone oil from the PDMS network, they implemented two different dyes of non-overlapping emission spectra. The silicone oil that served as a swelling fluid was dyed with a red perylene monoimide (PMI) dye ($\lambda_{\text{em}} \sim 700\,\text{nm}$), and a green fluorophore ($\lambda_{\text{em}} \sim 520\,\text{nm}$

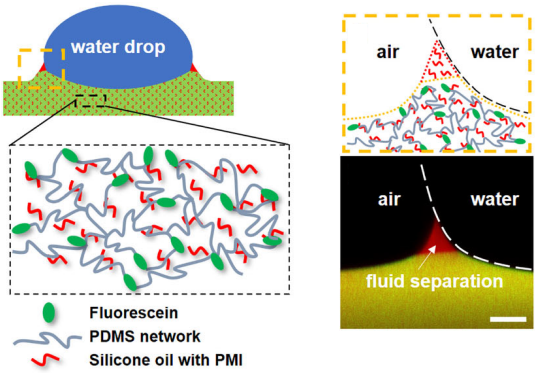


Figure 2.19: Schematic representation of a water droplet sitting on a swollen PDMS network. Bottom right: reconstructed z-stack laser confocal microscope image of a wetting ridge (red: extracted silicone oil, green: PDMS network, yellow: combination of green and red channels). Scale bar: 20 µm. Modified with permission from [49].

was bonded to the network to prevent the fluorophore to disperse into the fluid part [49]. They observed that a separation of silicone oil (red cusp region) from a PDMS network, referred as a "fluid separation", occurs near the contact line as shown in Figure 2.19 [49].

The authors also studied the influence of swelling and the degree of cross-linking on the static wetting ridge of a swollen PDMS network. They noticed more fluid separation for a softer (i.e. less cross-linked network), and also for a more swollen network [49].

They concluded that the surface tension of the liqudi drop pulls the network upwards and the fluid out, while the elastic energy of the network and the energy of mixing between the network and the swelling fluid lead to a finite height of the separated fluid [49].

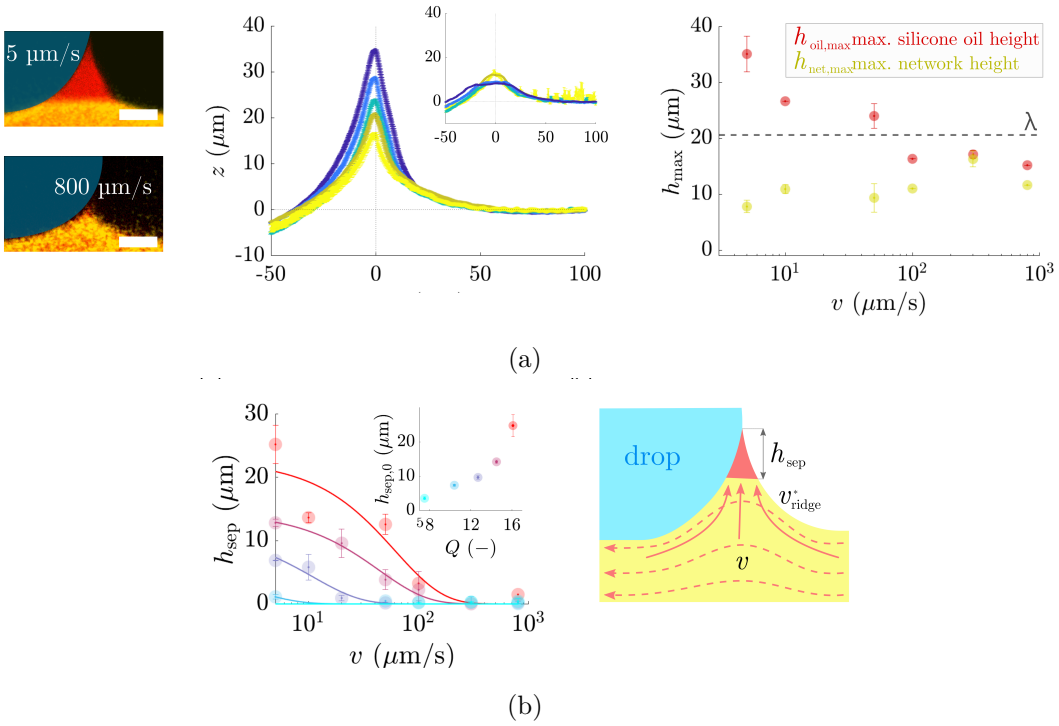


Figure 2.20: (a) Left: Experimental image of the dynamic wetting ridge different droplet velocity. Scale bar: 20 µm. Middle: Profile of the dynamic wetting ridge for different droplet velocity. from top to bottom $v = 5, 10, 50, 100, 300, 800\,\mu m/s$. Right: Maximum height of ridges of silicone oil $h_{oil,max}$ (red), and PDMS network $h_{net,max}$ (yellow). (b) Left: Separation height $h_{sep}$ vs droplet speed $v$ for different swelling ratios. $Q = 16$ (Cherry red), $Q = 14.5$ (bordeaux), $Q = 12.7$ (dark blue), $Q = 10$ (blue), and $Q = 7.5$ (torquoise). Inset, separation height for different $Q$ at zero speed $h_{sep,0}$. Right: competition of molecular (red solid arrows) and advective (red dashed arrows) fluxes on driving mechanism of phase separation ridge. Republished with permission from [50]

The same fluid separation also takes place in the case of a drop moving on a swollen PDMS surface. Hauer, *et al.* studied the effect of droplet dynamics on the wetting ridges of a soft and swollen PDMS surface [50].

They used soft PDMS networks with an elastic modulus of 3-5 kPa with different amounts of swelling silicone oil [50]. The fluorescence labelling was done in the same way as that of Cai, *et al.* (see previous page). The swollen PDMS network was mounted on a motorised stage, and

a 8 µL water drop was placed on the PDMS surface. The drop was fixed with a metal ring and the motorised stage moved at a constant speed [50]. The entire set up was installed on a laser confocal microscope to allow visualisation of a moving wetting ridge. The height of the PDMS network and the separated fluid were then measured with the corresponding droplet speed.

They found that the maximum height of silicone oil ($h_{\text{oil,max}}$) decreases, while the maximum PDMS network height ($h_{\text{net,max}}$) increases but not as significantly as the decrease of $h_{\text{oil,max}}$ when the droplet speed increases (see Figure 2.20 (a)). The separation of the height of silicone oil $h_{\text{sep}}$ ($h_{\text{sep}} = h_{\text{oil,max}} - h_{\text{net,max}}$) with an increase of the droplet speed was also measured (Figure 2.20 (b)). Here, $h_{\text{sep}}$ refers to the amount of pure silicone oil liquid phase separated, and it decreases with increasing droplet speed. They also compared the dynamic separation height of various substrates with different swelling ratio $Q$. When $Q > 10$, phase separation at the ridge was consistently observed [50]. $h_{\text{sep}}$ also increased with an increase of swelling ratio.

From these observations, Hauer *et al.* concluded that the competition of molecular flux between the PDMS network and the silicone oil, and drop advection determines the amount of liquid separation at the wetting ridge of a moving droplet [50].

## 2.4 Debate

Due to the behaviour of real soft surfaces, that are not expected in the ideal cases such as the phase separation of uncross-linked silicone oil, several theories and their applicability to the wetting of soft surfaces are still under a question by many literatures. In this section, we will discuss the two main debates in the field of soft wetting: the Shuttleworth effect for polymer gels and the validity of the Neumann's law in moving wetting ridges. These debates will also be addressed in Chapter 6.

### 2.4.1 Shuttleworth effect for polymer gels

As mentioned earlier in the Section 2.3.2, both the surface stress and the surface energy are strain-dependent for solids, and are related through the Shuttleworth equation (see Equation 2.26). However, no consensus has been reached regarding the existence of the Shuttleworth effect for the polymer gels [51].

Xu, *et al.* directly measured the surface stress as a function of the strain in a polymer gel [52]. A glycerol droplet was deposited on a soft silicone substrate ($E = 3.0\,\text{kPa}$) in which small fluorescent nanobeads were attached. A uniform baiaxial strain $\varepsilon_\infty$ was applied on the substrate with a biaxial stretcher ans the corresponding wetting profile was imaged with confocal microscopy.

As shown in the insert of Figure 2.21 (a), they observed a significant change in the geometry of the microscopic contact line. With an increase in the surface strain from 0 to 18%, the height of the wetting ridge decreased by a factor of three, and the ridge opening angle increased from 90.8° to 126.3° [52]. The strain at the contact line is a combination of the applied strain $\varepsilon_\infty$, and the localised deformation that forms the wetting ridge. Thus, they calculated the local strain $\varepsilon$ near the contact line by using the in-plane and out-of-plane displacements of the substrate

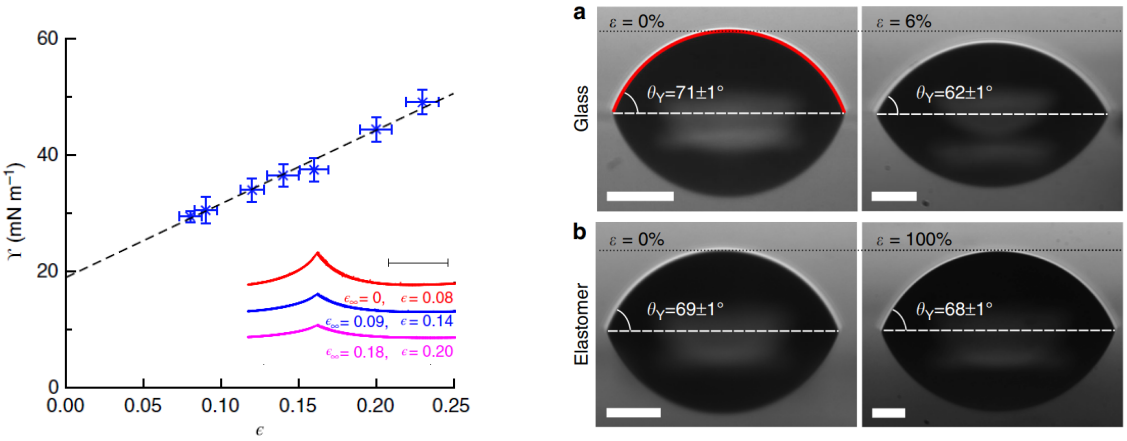


(a) (b)

Figure 2.21: (a) Left: Average surface stress as a function of the local strain for PDMS substrates deformed by a single glycerol droplet. Insert: Wetting profiles of a single glycerol droplet on unstretched (red), 9% stretched (blue), and 18% stretched (pink) PDMS substrates. Scale bar: 20 µm. Republished with permission from [52]. (b) Contact angle measurements of a glycerol droplet on strained and unstrained substrates. a: Glycerol droplet on unstrained (left) and 6% strained (right) polycarbonate glass. The red solid line indicates a typical fit of the circular cap. b: Glycerol droplet on unstrained (left) and 100% strained (right) Elastollan elastomer. Scale bar: 50 µm. The black dotted line in all the images indicates the height of each spherical cap. Republished with permission from [51]

by tracking the displacements of fluorescent beads in confocal microscopy. They noticed that the local strain increases and converges towards the $\varepsilon_\infty$ as the applied stress increases (see left image of Figure 2.21 (a)) [52]. By using the Neumann force balance and the measured opening angle of the wetting ridge, the authors calculated the strain dependence the surface stress as displayed in the right image of Figure 2.21 (a). They observed a linear increase of the surface stress $\Upsilon$ with an increase in the measured strain $\varepsilon$ [52].

From their experimental evidence, Xu, *et al.* concluded that the surface stress is indeed dependent on the surface strain of soft silicone elastomers, corroborating the validity of the Shuttleworth relation for the polymer gels.

On the other hand, Schulman, *et al.* compared the contact angles of glycerol droplets on strained and unstrained glassy and elastomer surfaces, and claimed to have found a strain-dependent surface stress of a glassy solid, but no strain-dependence of the surface stress of an elastomer surface [51].

A glycerol droplet was deposited on a polycarbonate glass, and on an elastomer surface. A strain $\varepsilon$ was applied to each substrate by using a motorised translation stage, and the contact angle of the droplet was measured by optical microscopy [51]. The contact angle of the glycerol droplet sitting on a glassy surface decreased from 71° to 62° with a 6% increase of the strain $\varepsilon$, as shown in Figure 2.21 (b) panel **a**. In contrast, the contact angle of the droplet did not change even with a 100% increase of surface strain of an elastomer [51].

Then they quantified the strain-dependence of the difference between the solid-solid and solid-vapour surface energies of strained glassy and elastomeric materials from the measured

contact angle. The Young's law (see Equation 2.1) was used to find the difference in surface energies ($\gamma_{SV} - \gamma_{SL}$) [51]. They found that the interfaces of polymeric glassy materials exhibit strain-dependent surface energies, but the surface energies of the interface involving elastomeric substrate have no strain-dependence [51]. Therefore, they concluded that glassy materials exhibit the Shuttleworth effect, but incompressible elastomers do not.

### 2.4.2 Validity of Neumann's law

The question of the existence of the Shuttleworth effect on polymer gels also gives rise to a question of the validity of the Neumann balance in a dynamic wetting ridge on a soft surface.

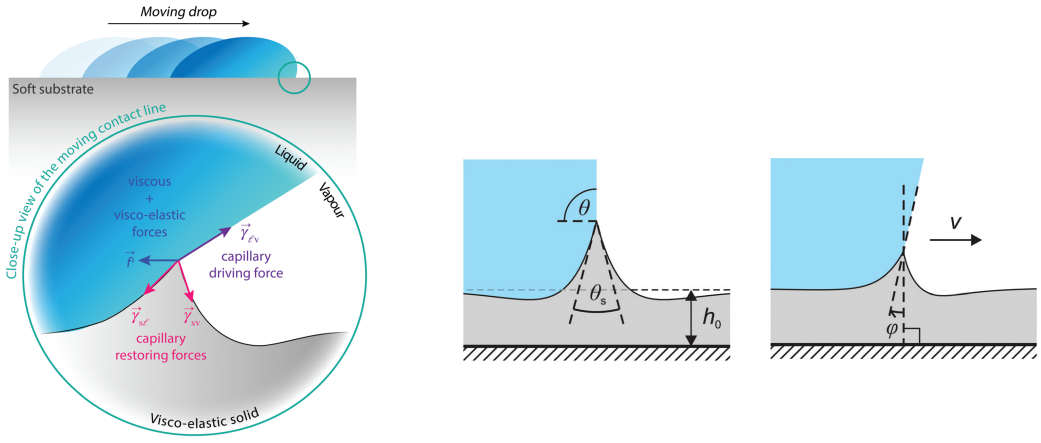


(a) (b)

Figure 2.22: (a) Schematics of the moving contact line region. Republished with permission from [53]. (b) Schematic representation of stationary (left) and dynamic (right) wetting ridge. $h_0$ is the substrate height, $\theta_S$ is the opening angle of solid wetting ridge. When the liquid contact line moves with velocity $v$, the wetting ridge rotates by $\varphi$. Republished with permission from [54]

Dervaux, *et al.* claimed that not only capillarity but also viscoelasticity of the soft substrate affect the wetting ridge dynamics [53]. Hence, they argued that the Neumann construction, which is solely based on capillarity, does not fully explain the motion of the triple contact line [53]. They instead suggested a non-linear force balance in which both non-linear localised capillary and viscoelastic forces oppose the motion of contact line:

$$\vec{f}_S = \vec{\gamma}_{LV} + \vec{\gamma}_{SV} + \vec{\gamma}_{SL} + \vec{f}_{ext}, \tag{2.27}$$

where $\vec{f}_{ext}$ indicates external forces other than surface tensions and viscoelastic stresses [53]. A schematic drawing of this non-linear force balance is shown in Figure 2.22 (a).

On the other hand, van Gorcum, *et al.* claimed that the contact line motion is still governed by Neumann's law. Figure 2.23 (a) shows the dynamic liquid contact angle of a water droplet moving on a soft PDMS surface ($\theta - \theta_{eq}$, open circles), and solid ridge rotation of the surface ($\varphi$, closed diamonds) as a function of the contact line speed $v$. At low speed, both the change of liquid contact angle and solid ridge rotation angle exhibit a power law dependence with an exponent $n$ being an exponent extracted from a fitting of power law relation to the rheological

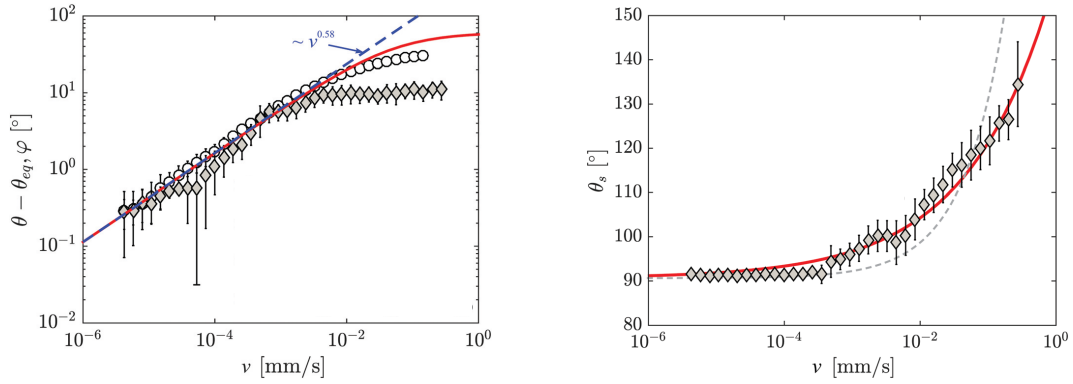


(a) (b)

Figure 2.23: (a) Evolution of the dynamic liquid angle $\theta - \theta_{\text{eq}}$ and the solid ridge rotation $\varphi$ with the contact line speed $v$. The blue dashed line shows a power law form with rheological exponent $n$, and the red solid line shows a prediction from the analytical solution. (b) Opening angle of the wetting ridge as a function of the contact line speed. The angles are described in Figure 2.22 (b). The red solid line and the gray dashed lines are best fits of power law of $v^{n/2}$ and $v^n$ respectively. Republished with permission from [54]

measurement of the substrate [54]. Also, both of these angles are in a good agreement with each other. Such finding provides a direct experimental evidence that Neumann's law is still valid at low velocity, and rejects the hypothesis on the existence of a viscoelastic contribution on the wetting ridge dynamics [54]. They also demonstrated theoretically that Neumann's law is relevant as long as $n < 1$. As discussed in Section 2.1.2, when the contact line is moving on a rigid solid surface, the viscous stress is non-integrable, leading to a singularity at the contact line region [24]. On the other hand, for soft solids, the stress displays a much weaker divergence and can still be integrated [55]. Van Gorcum, *et al.* suggested the stress ($\sigma$) form:

$$\sigma \sim \mu \left( \frac{v}{l} \tau \right)^n , \tag{2.28}$$

where $l$ is a distance from the contact line, $\mu$ and $\tau$ are respectively the complex modulus and the time scale extracted from rheological measurement of the soft solid [54]. The integrated stress vanishes when $n < 1$, and thus this shows that Neumann's relation is still valid.

Figure 2.23 (b) shows the evolution of the ridge opening angle $\theta_{\text{s}}$ as a function of the speed $v$. At larger contact line speed, $\theta_{\text{s}}$ increases with speed. Owing to the validity of Neumann construction, this shows that the solid surface tension is a dynamical quantity [54]. Van Gorcum *et al.* also observed a similarity between their velocity-dependent increase of $\theta_{\text{s}}$ and surface strain-dependent increase of the static solid angle of literatures [51, 52], further corroborating the existence of the Shuttleworth effect on dynamical wetting ridge.

Dervaux, *et al.* also compared their theory to the experimentally measured solid angle $\theta_s$, and dynamic liquid contact angle $\theta - \theta_{\text{eq}}$ from van Gorcum, *et al.* [54], as shown in Figure 2.24. The description of these angles are illustrated in Figure 2.22 (b). They found a better agreement between the experimentally measured angles with the suggested non-linear theory

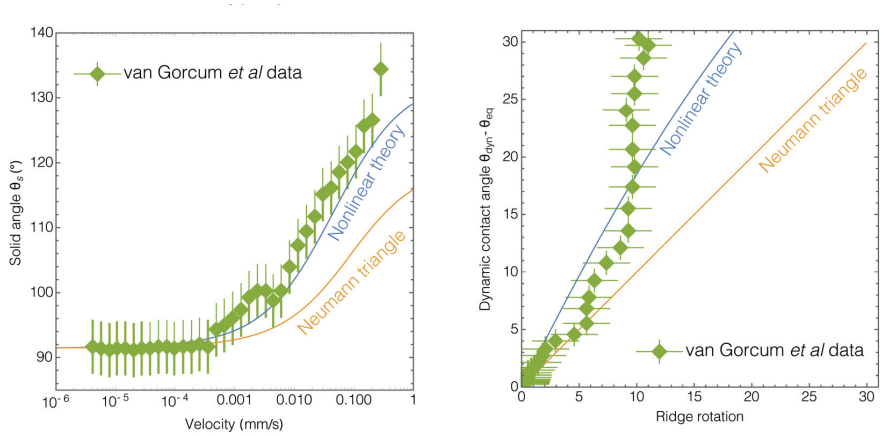


Figure 2.24: Comparison of experimental data from [54] (green diamonds) with non-linear theory from [53] (blue solid line) and Neumann construction (orange solid line). Left: solid angle $\theta_S$ as a function of velocity. Right: dynamic liquid angle as a function of ridge rotation. Republished with permission from [53]

than with Neumann triangle.

Such comparison of their theory with the experimental data of van Gorcum, *et al.* led to a conclusion that a model solely based on capillarity such as the Neumann force balance cannot fully describe the behaviour of dynamic wetting ridges on a soft surface, and viscoelastic contribution of the bulk solid has to be considered [53].

# Chapter 3

# Materials and experimental methods

## 3.1 Materials

### 3.1.1 PDMS preparation

Polydimethylsiloxane (PDMS) networks are usually prepared by mixing a base polymer and a cross-linker. We prepare PDMS networks by using different kinds of silicone elastomers from Gelest, Inc., and Dow Corning and varying the base/cross-linker mixing ratio.

The networks from Gelest, Inc. are formulated based on the recipe from Jensen, *et al.* [56], which involves two premixes: part A, and B. Part A is a mixture of a base polymer and a catalyst. Part B is obtained by diluting a cross-linker into the same base, which are unreactive without the presence of catalyst. This part allows to prevent local cross-linking that could happen if drops of cross-linker were directly added into the base premix A. Such local cross-linking can be visualised as lumps in a mixture and can form inhomogeneous structures and disturb the curing of bulk elastomer [34]. Once prepared, parts A and B are mixed together.

PDMS samples from Dow Corning are usually prepared by mixing CY52-276 components A and B that are already provided by the manufacturer. The two components are mixed with a mass ratio of 1.3:1.

### 3.1.2 Swelling and extraction

Toluene and dichloromethane (DCM) are used as the solvents to extract free uncross-linked molecules inside the PDMS complex.

| Solvent | Solubility parameter ($\delta$) [$\text{cal}^{1/2}\text{cm}^{-3/2}$] | Dipole moment ($\mu$) [D] |
|---|---|---|
| PDMS | 7.3 | 0.6-0.9 |
| Toluene | 8.9 | 0.4 |
| DCM | 9.9 | 1.6 |

Table 3.1: Solubility parameter $\delta$, and dipole moment $\mu$ of solvents

Table 3.1 shows the solubility parameter $\delta$, and dipole moment $D$ of each solvent. The solubility parameter and the dipole moment are important quantities to predict the degree of swelling and solubility of a polymer in a solvent [57]. $\delta$ estimates the degree of interaction

between materials numerically, and is thus a good indicator of solubility of the material [58]. There are two different ways to derive the solubility parameter $\delta$.

Hildebrand first introduced the numerical indication of the solvency behaviour of a liquid in 1936, known as the solubility parameter $\delta$, when $\delta$ is derived from cohesive energy density $c$ [58]. The equation is as followed:

$$c = \frac{\Delta H - RT}{V_{\mathrm{m}}} \tag{3.1}$$

$$\delta = \sqrt{c} \tag{3.2}$$

where $\Delta H$ is the heat of vapourisation of liquid, $R$ is the ideal gas constant, $T$ is the temperature, and $V_{\mathrm{m}}$ the molar volume of liquid [58]. Heat of vapourisation $\Delta H$ is correlated to solubility $\delta$ due to the van der Waals interaction between the molecules [58]. The van der Waals intermolecular interaction that has to be overcome when vapourising a liquid is assumed to be the same as that needs to be overcome when dissolving the liquid [58].

The advantage of Hildebrand solubility parameter is that finding the parameter of solvent mixtures is easy to calculate (via volume fraction of each solvent). However, deviation of the expected degree of swelling of a material with solvents according to the Hildebrand parameter from the actual experimental measurements was observed [59].

Hansen in 1967 then suggested a parameter that includes the contribution of dispersion, polar, and hydrogen bonding forces on the basis of Hildebrand solubility parameter [60]. The Hansen parameter is expressed as:

$$\delta^2 = \delta_D^2 + \delta_P^2 + \delta_H^2, \tag{3.3}$$

where $\delta_D$ is the dispersion force, $\delta_P$ the polar force, and $\delta_H$ the hydrogen bonding force [61].

Dipole moment occurs due to the unequal distribution of electrons between two atoms when there is a difference in electronegativity of atoms [62]. As the dipole moment of a bond is a vector quantity, the overall polarity $\mu$ of the molecule is a vectorial sum of these dipole moments [62].

The closer the $\delta$ and $\mu$ of the solvent to those of PDMS, the network is more miscible and will swell more in the solvent.

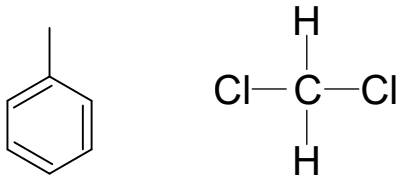


(a) (b)

Figure 3.1: Chemical structures of (a) toluene, and (b) DCM

Dichloromethane (DCM) has higher dipole moment than toluene due to the two chlorine atoms present as illustrated in Figure 3.1 (b). Lee et al, suggested four categories in solubility of PDMS in solvents. DCM belongs to a category of "moderate solvent" ($9.1 < \delta < 11.3$,

$0.46 < D < 2.78$), and tolune is a "good solvent" ($7.3 < D < 9.5$) in PDMS [57].

A swelling of PDMS network in a solvent can be explained thermodynamically on the basis of Flory-Huggins lattice theory.

Flory and Huggins first investigated the thermodynamics of binary polymer solutions by assuming that the molecules of a pure solvent and a polymer are distributed over $N_0$ lattice sites in a rigid lattice frame [63]. The total number of lattice sites $N_0$ can be expressed as:

$$N_0 = N_1 + r \cdot N_2, \tag{3.4}$$

where $N_1$ is the number of solvent molecules, and $N_2$ is the number of polymer molecules consisting $r$ repeated units. By using the standard theory of mixing and Stirling's approximation,they suggested an expression for the entropy of mixing, which is given as:

$$\Delta S_{\text{mix}} = -k(N_1 \cdot \ln \phi_1 + N_2 \cdot \ln \phi_2) \tag{3.5}$$

where $\phi_1$ and $\phi_2$ are the volume fractions of the solvent and polymer respectively. The Gibbs free energy of mixing $\Delta G_{\text{mix}}$ is expressed as:

$$\Delta G_{\text{mix}} = \Delta U_{\text{mix}} - T\Delta S_{\text{mix}} \tag{3.6}$$

where $\Delta U_{\text{mix}}$ is the enthalpy of mixing, which can be positive (endothermic) or negative (exothermic). The Flory Huggins interaction parameter $\chi$, a parameter that is used to describe the polymer-solvent interaction, is given by:

$$\chi = \Delta U_{\text{mix}}/(kTN_1\phi_2) \tag{3.7}$$

Substituting Equation 3.5, and 3.7 into the Equation 3.6 gives:

$$\Delta G_{\text{mix}} \approx \Delta F_{\text{mix}} = kT(\chi N_1\phi_2 + N_1 \ln \phi_1 + N_2 \ln \phi_2) \tag{3.8}$$

$$= RT(\chi n_1\phi_2 + n_1 \ln \phi_1 + n_2 \ln \phi_2), \tag{3.9}$$

where $N_1 = n_1N_A$,$N_2 = n_2N_A$, and $R = kN_A$, in which $N_A$ is an avogadro constant. When the two components are mixed, the free enthalpy of mixing is determined by chemical potential $\mu$ of both components, defined as:

$$\Delta\mu_i = \partial\Delta G_{\text{mix}}/\partial n_i. \tag{3.10}$$

On the basis of Flory-Huggins theory of mixing, Flory and Rehner developed a model that describes the isotropic swelling of rubber cross-linked in a dry state [64]. The polymer network can absorb a large amount of liquid when immersed in a"good solvent", and starts to swell. This swelling is opposed by elastic forces within the network due to the tendency of the network to recoil to its orginal shape [65]. The overall change of free energy upon the swelling of polymer gel thus is given as:

$$\Delta F = \Delta F_{\text{mix}} - \Delta F_{\text{el}}. \tag{3.11}$$

The maximum swelling occurs when the elastic and the polymer-liquid forces are in equilibrium [65]. Thus, $\Delta F = 0$, $\Delta F_{\text{mix}} = \Delta F_{\text{el}}$. Flory-Rehner equation also considers the effect of cross-linking degree on the elastic forces contribution [66]. The equation is represented as:

$$-[\ln(1-\phi_2)+\phi_2+\chi_1\phi_2^2] = V_1 n(\phi_2^{1/3} - \frac{\phi_2}{2}), \tag{3.12}$$

when $V_1$ is the molar volume of the solvent, $n$ is the number of network chain segments bounded on both ends by cross-links, and $\chi$ is the Flory-Huggins solvent-polymer interaction parameter [67]. Equation 3.12 can be expressed differently:

$$-[\ln(1-\phi_2)+\phi_2+\chi_1\phi_2^2] = \frac{V_1}{\overline{\nu}M_c}\left(1-\frac{2M_c}{M}\right)\left(\phi_2^{1/3}-\frac{\phi_2}{2}\right), \tag{3.13}$$

where $\overline{\nu}$ is the specific volume of the polymer, $M$ refers to the molecular mass of the initial polymer, $M_c$ the average molecular mass between cross-links [68].

### 3.1.3 Flat substrate preparation

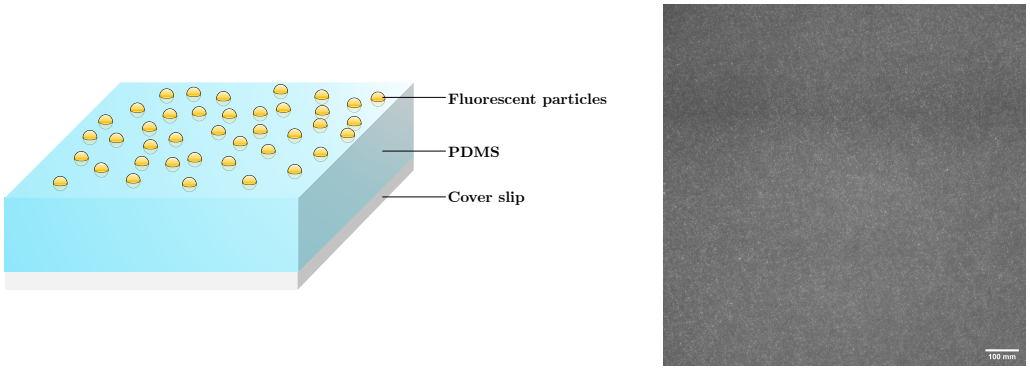


(a) (b)

Figure 3.2: (a) 3D representation of a prepared flat substrate. Fluorescent particles are partially engrained into the cured PDMS gel. (b) Bright field microscope image of a prepared flat substrate. White dots indicate coated fluorescent particles

A prepared uncured PDMS mixture of Dow Corning CY52-276 A and B with a mass ratio 1.3:1 is coated on a glass cover slip (dimension: 24 mm x 24 mm) with a spin coater with rotational frequency of 2000 rpm for 100 s. The coated PDMS layer has a thickness of around 100 µm. The coated substrate is cured in an 75$^o$C oven for two days. The cured substrate is then dip coated with a solution of fluorescent particles for a minute. The fluorescent particles are water-soluble FluoSpheres™ Carboxylate-Modified Microspheres with diameter of 100 nm from Invitrogen™, and the particle solution is prepared by dissolving 150 µL fluorescent particles in 30 mL 0.5M sodium chloride (NaCl) solution. The FluoSpheres are partially engrained into the PDMS gel after the coating process as illustrated in Figure 3.2 (a). Indeed the fluorescent particles sink as their radius (50 nm) is much less than the elastocapillary lengthscale defined as $\gamma_{\text{SA}}/E$, in which $\gamma_{\text{SA}}$ is the surface tension (or surface stress) of the PDMS gel, and $E$ is the elastic modulus of the gel [69].

Figure 3.2 (b) shows a bright field microscope image of a prepared flat PDMS substrate. We can observe that the fluorescent particles (white dots) are homogenously coated onto the substrate.

### 3.1.4 Cavity preparation

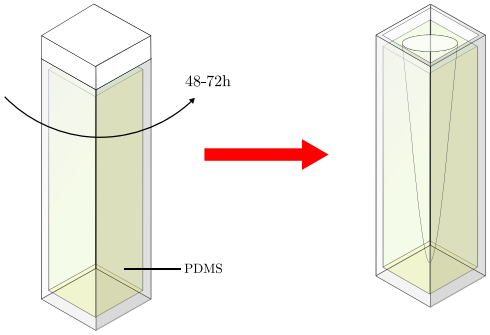


Figure 3.3: Cavity substrate preparation process. A 1 cm × 1 cm × 4 cm cuvette is filled with uncured PDMS mixture, and spun for 48 to 72 hours with a constant rotational speed. An empty parabolic cavity is eventually created in the middle of cuvette

We use the method from van Gorcum *et al.* [54] to prepare a PDMS parabolic cavity inside a cuvette. Prepared uncured PDMS mixture of part A and B is degassed with a vacuum pump and is poured into a 4 µL cuvette, leaving a small volume of air at the top. The cuvette is then covered with a lid, and spun for 2 to 3 days in room temperature until the network is completely cured. The spinning speed depends on the viscosity of elastomer mixture, ranging from 60 to 80 rpm. If the mixture is more viscous, a faster rotational speed is required. The centrifugal force extends the small air volume into a parabolic cavity as illustrated in Figure 3.3 [54].

## 3.2 Experimental methods

### 3.2.1 Rheometry

A rheometer is an important tool to measure mechanical properties of the prepared PDMS samples under an applied force. We use an oscillatory rheology for the measurement. The oscillatory measurement for scientific purposes was first introduced by Eisenschitz, *et al.* in 1933 to determine mechanical material constants of colloids [70].

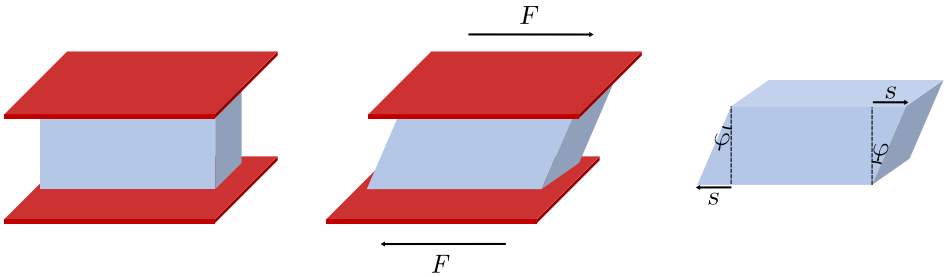


Figure 3.4: A simple illustration of a shear rheology. A sample is sandwiched between the top and bottom plates, and a shear force $F$ is applied parallel to the plates

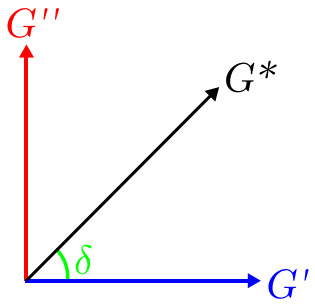


Figure 3.5: Geometric relation of complex modulus $G^*$ with storage modulus $G'$, and loss modulus $G''$. The phase shift $\delta$ is indicated as the angle between $G^*$ and $G'$. The $G'$ axis is a real axis while the $G''$ axis is an imaginary axis

In order to explain the oscillatory test of a rheometer, we use the two-plates model as illustrated in Figure 3.4. A sample is "sandwiched" between the top and bottom plates, and the upper plate attached to a rod that is connected to a rotor at the other end moves back and forth in a parallel direction to the lower plate with a shear force $F$. The bottom plate remains stationary in the meantime. Such motion of the upper plate gives rise to shearing of the sample with a deflection path $s$ and a deflection angle $\varphi$.

A rotational rheometer can either apply a torque and measure the rotational speed, or apply a rotational speed and measure the torque required to maintain that speed. There are two modes of oscillatory rheological measurements, known as controlled shear deformation (CSD), and controlled shear stress (CSS) modes.

For the CSD test mode, the angular displacement $\varphi$ is preset, and the torque $M$ required to give that displacement is measured from which the shear stress $\tau$ is calculated. On the other hand, in the CSS mode, the oscillating torque $M$ is applied from the rotor to the upper plate, and the resulting angular displacement $\varphi$ is measured, from which the shear strain $\gamma$ can be calculated.

The ratio of the applied (or measured) shear stress to the measured (or applied) shear strain gives the shear modulus $G^*$. As the shear modulus is in a complex form, it consists of a real part $G'$, a storage modulus, and an imaginary part $G''$, a loss modulus. The relationship is as follows:

$$G^* = G' + iG'' \tag{3.14}$$

Both stress and strain are time-dependent and thus are expressed in sinusoidal form. For a perfectly elastic solid, as the stress is proportional to the strain according to the Hooke's law, the maximum stress occurs at the maximum strain. The strain and the stress are then said to be "in-phase". For a pure viscous liquid, the Newton's law applies, and the maximum stress occurs at the maximum strain rate, and therefore the stress and the strain are "out-of-phase" by $\pi/2$rad. As a viscoelastic solid posseses characteristics of both purely elastic solid and perfectly viscous liquid, the phase difference between the stress and the strain is between 0 and $\pi/2$. This phase shift ($\delta$) determines the contribution from the viscous and elastic proportions to the characteristics of the viscoelastic material $G^*$.

As the rheometer is temperature controlled by a thermostat, high temperature curing of a

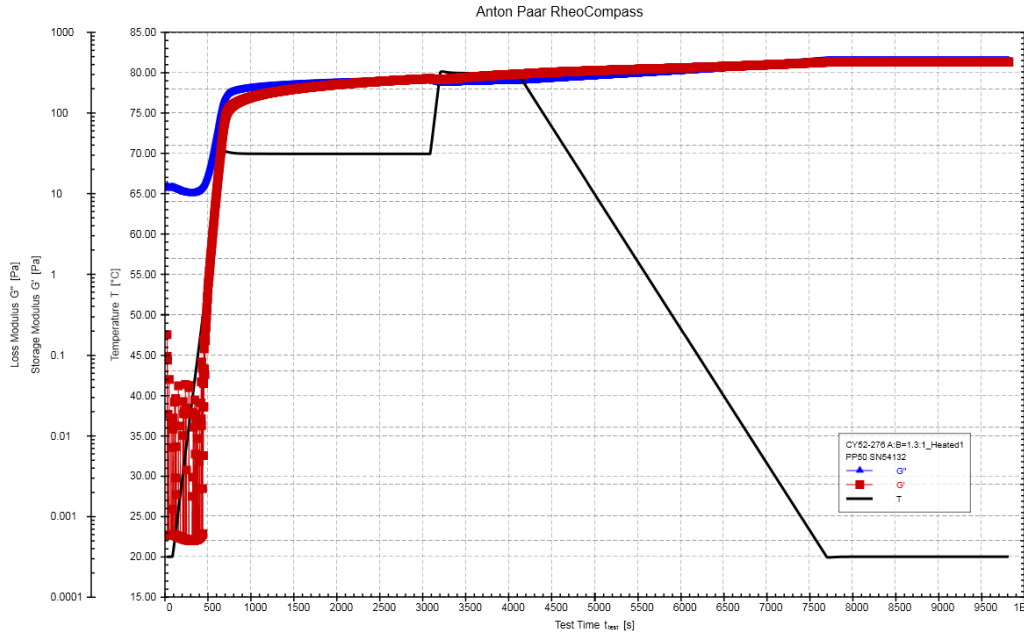


Figure 3.6: Curing protocol of a PDMS sample with the rheometer. The black solid line represents the set temperature, the blue triangles are the measured loss moduli $G''$ of the curing sample, and the red squares represent the measured storage moduli $G'$ of the sample while curing.

PDMS sample can be done within the instrument. Figure 3.6 shows an exemplary rheometer curing protocol for a prepared PDMS sample. The maximum temperature of the curing protocol was set as 80°C as the oven used for the PDMS curing is set at 75°C. The storage modulus $G'$, and the loss modulus $G''$ of the sample can be measured during the curing process, and we can observe their evolution as a function of temperature. Both storage and loss moduli of the PDMS mixture increase with an increase in temperature in the beginning. A cross-over of the two moduli occurs at high temperature, indicating that the elastic portion of the complex modulus is more dominant than the viscous portion, i.e. the sample is being cured successfully.

The viscoelastic materials show time dependence and thus G'and G" are not constants. Also, as mentioned in Section 2.2.1, PDMS gels have various time scales and we can obtain a spectrum of these time scales. Thus, the complex modulus of PDMS gels adopts a power law form:

$$G^* = G_0 \left(1 + (i\omega\tau)^n\right), \tag{3.15}$$

when $G_0$ is a low frequency storage modulus, $\omega$ is an angular frequency, $\tau$ a time scale, and $n$ is an exponent.

The time dependence of each modulus can be evaluated by changing the frequency of the applied stress or strain. Such rheological measurement is called a frequency sweep. High frequency corresponds to the short time scale, and the low frequency represents the long time scale. During the preparation of either flat or parabolic cavity substrate, a rheological measurement of the formulated elastomer mixture with Anton Paar MCR 502 rotational rhoemeter is always conducted.

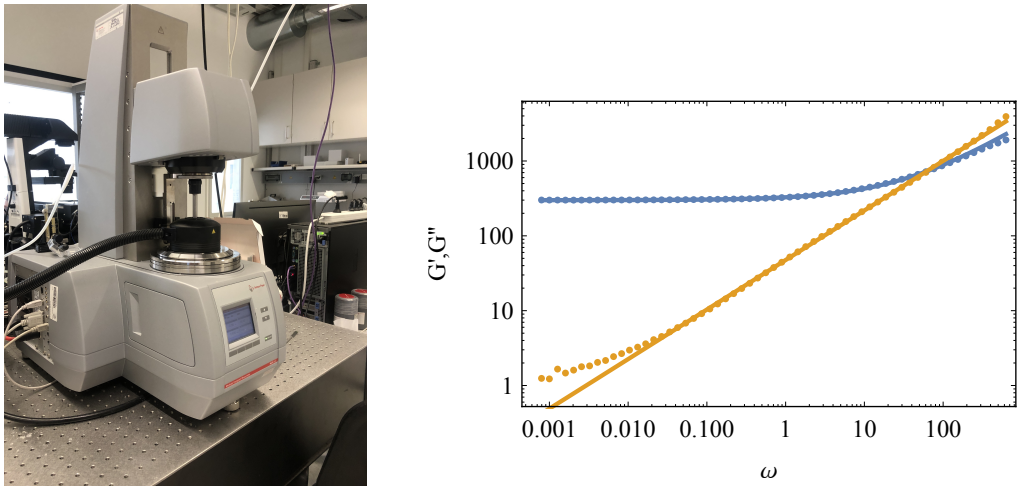


(a) (b)

Figure 3.7: (a) Anton Paar MCR 502 rotational rheometer in the lab (b) An examplary rheological plot of PDMS gel. Blue points: measured storage modulus ($G'$ of the gel as a function of rotational frequency $\omega$, indicates elastic portion. Dark yellow points: measured loss modulus ($G''$) of the gel as a function of rotational frequency $\omega$. The solid lines represent the fitting of data points with a power law equation.

Figure 3.7 (b) is an exemplary rheology plot of a PDMS gel. At higher frequency, loss modulus is more dominant, and as $\omega$ decreases, the loss modulus decreases linearly while the storage modulus starts to plateau. Solid lines indicate the fitting of data points with the above-mentioned power law equation. From the fitting, we get: $G_0 \approx 339$ Pa, $n \approx 2.13$, $\tau \approx 0.129$, and $n \approx 0.628$.

### 3.2.2 Surface tension measurement

A pendant drop tensiometer captures an image of a drop and uses the shape of the drop to calculate its surface tension. A pendant drop, that is suspended from a needle into an atmospheric phase or ambient liquid, is most commonly used to measure the surface tension. Surface tension tends to deform a drop into spherical shape, while gravity pulls down the drop from its spherical shape, leading to formation of pear-like shape of the drop.

The hydrostatic pressure is the pressure exerted by the fluid at an equilibrium at a certain point within the fluid, mainly due to the gravitational effect. The prssure $p$ at the vertical height $z$ within the pendant drop is described as:

$$p = \rho g h, \tag{3.16}$$

where $\rho$ is the fluid density, and $g$ is the gravitational acceleration.

The difference in the hydrostatic pressure $\Delta p - \Delta p_0$ between the two points within the drop with distance $z$ is thus described as:

$$\Delta p - \Delta p_0 = \pm \Delta g z. \tag{3.17}$$

The surface tension pulling the surface of the pendant drop increases the pressure inside

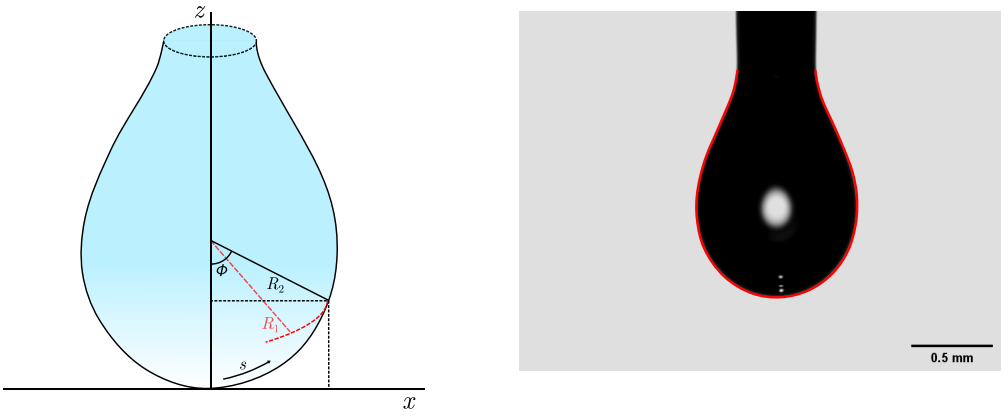


(a) (b)

Figure 3.8: (a) Schematic representation of a pendant drop. $R_1$ and $R_2$ are radii of curvature of the drop, and $s$ is the arc length of the drop. Adapted from Dataphysics-instruments.com. (b) Pendant drop of Dow-Corning CY52-276 A PDMS elastomer in air. The red line overlayed on the image shows an example of drop profile fitting by DataPhysics OCA tensiometer

the drop. According to Figure 3.8 (a), the Laplace pressure is the pressure difference between inside and outside of the drop, and is expressed as:

$$\Delta p = \gamma \left( \frac{1}{R_1} + \frac{1}{R_2} \right), \tag{3.18}$$

where $R_1$, and $R_2$ are the radii of curvature. $R_1 = R_2 = R_0$ at the lowest position of the drop, and thus by using the Equation 3.18, pressure at reference plane $\Delta p_0$ can be expressed as:

$$\Delta p_0 = \frac{2\gamma}{R_0}. \tag{3.19}$$

Combining Equations 3.17, 3.18, and 3.19 gives:

$$\Delta p = \frac{2\gamma}{R_0} \pm \Delta \rho g z \tag{3.20}$$

$$\gamma \left( \frac{1}{R_1} + \frac{1}{R_2} \right) = \frac{2\gamma}{R_0} \pm \frac{\Delta \rho g z}{\gamma} \tag{3.21}$$

$$\left( \frac{1}{R_1} + \frac{1}{R_2} \right) = \frac{2}{R_0} \pm \frac{\Delta \rho g z}{\gamma} \tag{3.22}$$

Figure 3.8 (a) shows that $\sin\phi = \frac{x}{R_2}$, i.e. $\frac{1}{R_2} = \frac{\sin\phi}{x}$. Thus, Equation 3.22 becomes:

$$\left( \frac{1}{R_1} + \frac{\sin\phi}{x} \right) = \frac{2}{R_0} \pm \frac{\Delta \rho g z}{\gamma} \tag{3.23}$$

Parametrisation with arc length $s$ gives:

$$\frac{d\phi}{ds} = -\frac{\sin\phi}{x} + \frac{2}{R_0} \pm \frac{\Delta\rho g z}{\gamma} \tag{3.24}$$

$$\frac{dx}{ds} = \cos\phi \tag{3.25}$$

$$\frac{dz}{ds} = \sin\phi \tag{3.26}$$

with boundary conditions $0 = x(s = 0) = z(s = 0) = \phi(s = 0)$. Figure 3.8 (b) shows a Dow Corning CY52-276 A pendant drop in air. The numerical fit of the shape of the drop (red solid line in the figure) gives the value of PDMS/air surface tension.

### 3.2.3 Confocal microscopy

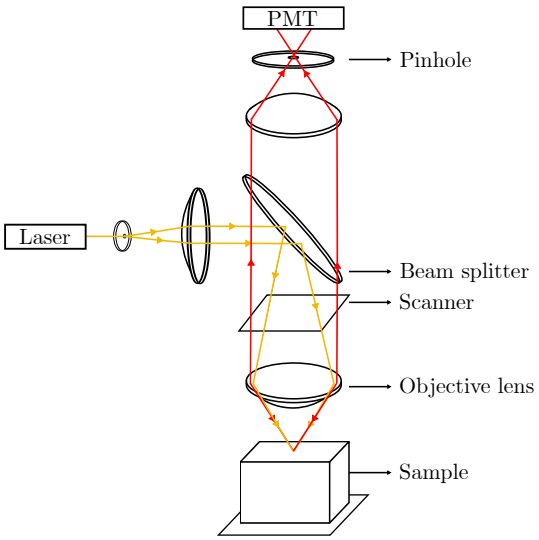


Figure 3.9: Illustration of laser confocal scanning microscope (LCSM). Yellow: excitation light pathways. Red: emission light pathways.

Laser confocal scanning microscopy (LCSM) has been widely used in biological sciences such as cell biology [71], and developmental biology [72] due to its ability to obtain high quality [71], controllable depth field, and elimination of out-of-focus information [73].

Figure 3.9 describes the components of the laser confocal scanning microscope (LCSM) and the excited and emitted light pathways. The laser produces a high intensity excitation light that reflects off the dichroic mirror (beam splitter). The light beams are scanned across the sample and dye in the sample fluoresces. This leads to an emission of fluorescent light. The emitted fluorescent light from the in-focus point is focused into the pinhole and is detected by a photomultiplier tube (PMT). However, the emitted light from the out-of-focus point does not go through the pinhole and is thus largely excluded from the detector. The pinhole diameter is thus an important parameter to decide the signal to noise ratio and the resolution of the image. The larger the diameter, the more out-of-focus emitted light will pass through the pinhole, leading to a brighter image with larger signal to noise ratio, but the resolution will be worse.

A confocal microscope can scan throughout the sample slice by slice through the vertical

axis. Thus, we can re-build a 3D image of the sample (usually via Fiji ImageJ) after the data acquisition.

### 3.2.4 Shadowgraphy

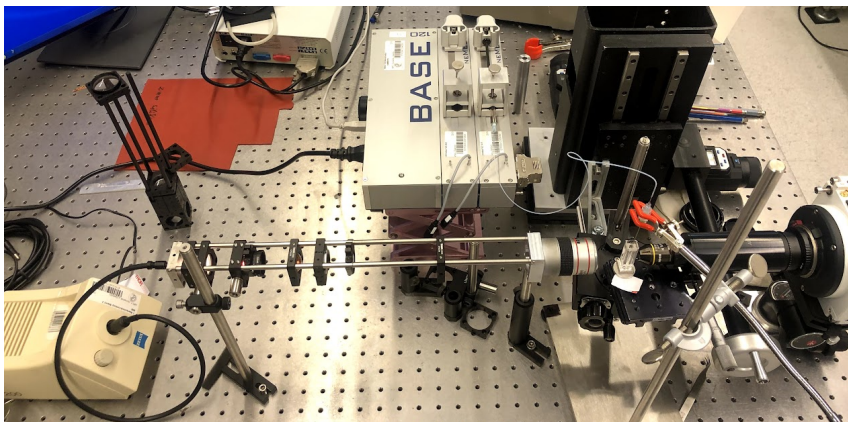


Figure 3.10: Picture of our shadowgraphy set up. The left hand side of the photo shows the light source, and the right hand side shows the camera

In our soft wetting experiments, the deformation of a very soft PDMS surface is achieved by filling our previously described cuvette with two different fluids. A heavy liquid is first injected into the bottom of the cavity until the meniscus reaches about a third to a half of the cuvette height. The rest of the cavity is then filled with a lighter liquid (or not filled with any liquid if we measure with air as the second fluid). These two liquids are immiscible such that they form a triple contact line with the PDMS surface. The motion of the resulting liquid contact line is induced by a constant flow of the heavier liquid generated with a Nemesys low pressure syringe pump. The corresponding flow rate of the liquid typically ranges from 0.005 µL/s to 50 µL/s.

Images of the wetting ridge moving along the cavity are acquired with a high-speed camera placed in front of the cuvette, which is illuminated from behind as presented in Figure 3.10. The wetting ridge is imaged in the plane of symmetry of the cavity, perpendicular to the optical axis. This configuration allows to improve the contrast of our images by producing a shadow due to refraction of the incident light at the surface of the cylindrical cavity. Thus our home-made shadowgraphy set up allows us to collect images with high spatio-temporal resolution, with only a limit of optical resolution from the set up itself.

Our setup consists of a combination of different lenses and diaphragms in order to produce a collimated Köhler illumination, focused into the imaging plane with a 5x microscope objective. To briefly describe, we form an intermediate image of the light source (the core of an optical fiber in this case) by focusing the diverging light beams with a first lens called collector. A first diaphragm (field diaphragm) is placed right after the lens and is used to control the size of the illuminated area on our sample without changing the intensity. A second diaphragm (aperture diaphragm) is placed in the focal plane where the intermediate image of the light source is formed. This aperture diaphragm affects the light intensity via the angles of transmitted light. Thus, tuning the aperture of this diaphragm controls the image resolution. After

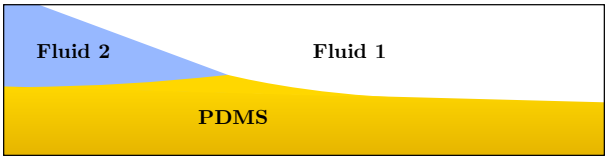


(a)

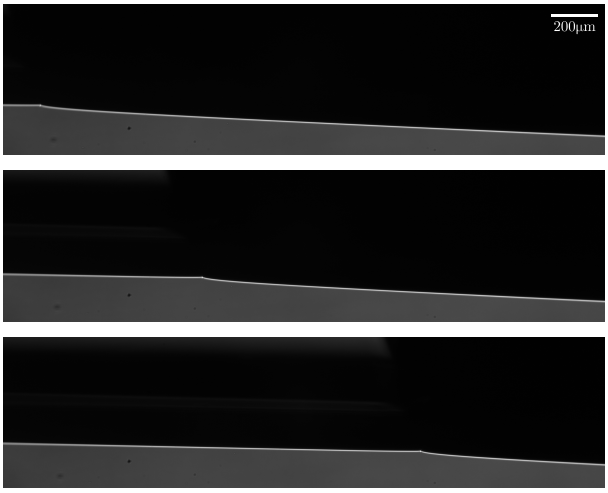


(b)

Figure 3.11: (a) Schematic representation of wetting ridge of the PDMS gel cavity (b) Dynamics of wetting ridge of gel cavity

the aperture diaphragm, we have built a condenser by using several lenses to ensure a homogeneous illumination. Finally the light is focused by a 5x microscope objective placed after this condenser.

The final image of the wetting ridge is formed on the sensor of a camera by a 10x microscope objective equipped with a tube lens that creates an intermediate focal plane. Typical images of a moving wetting ridge obtained with this setup are shown in Figure 3.11.

The exemplary images presented in Figure 3.11 (b) are rotated by 90°. As described in Figure 3.11 (a), heavier liquid (Fluid 2) is on the left hand side of the wetting ridge, and lighter fluid (Fluid 1) is on the right hand side. When the heavier liquid is injected into the cavity i.e. from right hand side to the left hand side of Figure 3.11 (b), the contact line moves to the right.

### 3.2.5 Image analysis

Images like the ones presented in Figure 3.11 are analysed with an in-house developed Python code for a sub-pixel edge detection technique. As the prepared cavity itself has an inclination angle (see Figure 3.3), the undeformed profile of the gel is determined and is then fitted with a second degree polynomial function. The horizontal and vertical positions of the undeformed surface are extracted. The detected points of the deformed profile are subtracted with the extracted undeformed points, resulting in the profile of the wetting ridge as shown in Figure 3.12. The imaging scale is 0.800 µm/pixel. The region within 4 µm left and right side away from the tip of the wetting ridge look rounded in the detected profile due to the optical resolution limit.

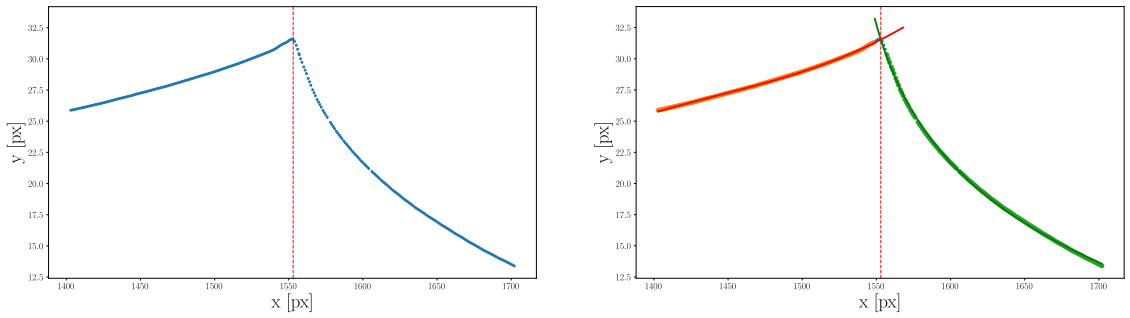


(a) (b)

Figure 3.12: (a) Detected profile of a wetting ridge. (b) Fitting of the profile with the suggested Equations 3.27, and 3.28

The horizontal liquid-solid contact line position is determined by the minimum curvature of moving window linear fit to the extracted data points. The contact line position is indicated by the red dashed lines in Figure 3.12.

Due to the apparent asymmetry of the wetting ridge, we fit each side of the contact line with a fitting equation respectively by using the horizontal contact line position obtained by the earlier method. For the left hand side that is in contact with bottom fluid the profile is fitted with a third order polynomial function:

$$y = a_1 + b_1 x + c_1 x^2 + d_1 x^3. \tag{3.27}$$

For the right hand side profile in contact with either air or top liquid we used:

$$y = a_2 + b_2 \log\left(c_2 + x\right). \tag{3.28}$$

When performing thse two fits, a few points (4-6 pixels) at the tip of the ridge within the resolution limit were not taken into account. Intersection of two fitting curves estimates the vertical location of the ridge tip, and we can find the solid angles from the slopes of these two curves. The two important solid angles here are $\theta_s$, and $\varphi$.

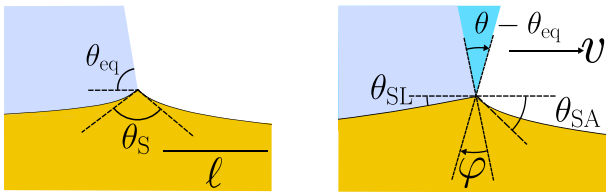


Figure 3.13: Rotation of a wetting ridge when liquid contact line moves with velocity $v$. $\theta_S$ is an opening angle, and $\varphi$ is a rotational angle of a solid wetting ridge. $\theta - \theta_{eq}$ is a dynamic liquid angle

Figure 3.13 describes how these angles are defined. $\theta_s$, is an opening angle of the wetting ridge. $\varphi$ represents a rotation of bisector when the liquid meniscus moves with a constant velocity $v$. The change of liquid contact angle $\theta - \theta_{eq}$, when $\theta_{eq}$ is the stationary liquid angle, was also recorded in our study.

# Chapter 4

# Tailoring polydimethylsiloxane (PDMS) elastomers of different mechanical properties

## 4.1 Introduction

Silicone elastomers such as polydimethylsiloxane (PDMS) have a wide range of real-life applications. Their chemical inertness (except when exposed to strong acids or bases [74]), biocompatibility, hydrophobicity, and other properties have attracted researchers of various fields such as biomedicine [75], electronics, and microfluidics [76].

There are various reactions known for the synthesis of polymers including Michael addition [77], thio-lene [78, 79], and Diels-Alder [80] reactions. PDMS undergoes catalytic hydrosilylation reaction which involves an addition of Si-H bonds into unsaturated C=C bonds [81] in the presence of late-transition metal complex catalyst. Ideally, the molecular weight of the network are equal to the molecular weight of the pre-polymers (the base polymer and the cross-linker)[82, 83]. In reality, the PDMS network can deviate from the ideal case due to the unbalanced stoichiometry of the reticulation and steric hindrance [66].

PDMS network formulation is done via mixing a base polymer with a cross-linker, and curing the mixture under high temperature for a certain period of time (also known as reticulation). It is well-known that the mechanical properties of these networks change according to the degree of cross-linking (mixing ratio of a base polymer to cross-linker) within the network. The lower the degree of cross-linking, the softer the network is [84]. The distance between each cross-linked chain needs to be increased in order to form soft PDMS gels. There are several approaches to do so, such as decreasing the concentration of reactive functional group [85], changing the molecular weight of ingredients [86], or even by using bottlebrush polymers [87].

Commercially available silicone elastomers such as Dow-Corning CY52-276, and Sylgard 184 are the most commonly used materials in microfluidics, electronics encapsulants or pharmaceutical research [34]. Such elastomer kits usually have two different parts named“A”, and “B”, where one of them is designated as a base polymer and the other as a cross-linker. PDMS networks formulated with Sylgard 184 are relatively stiff with elastic moduli of a few MPa. The

elastocapillary length of these networks even under a high surface tension liquid such as water will be in nanometer scale. Thus, these networks are not compatible with our study on the wetting ridge of the soft surface. Dow-Corning CY52-276 elastomer kit allows us to prepare networks with elastic moduli ranging from a few kPa to a few tens of Pa, giving rise to the elastocapillary length of µm. The deformation of these soft surfaces will thus be visible with our imaging set up.

However, information on the chemical structures or molecular weights on CY52-276 polymers is rarely given. It is certainly not easy to formulate PDMS gels of different mechanical properties without sufficient information on the ingredients. We instead use combinations of various base polymers and cross-linkers of different molecular weight from Gelest, Inc. The PDMS samples are prepared by varying the mixing ratio between these base and cross-linkers.

The corresponding stoichiometric ratio of each sample is also calculated. The stoichiometric ratio here refers to the ratio of the initial number moles of vinyl functional group to that of silane functional group present in the mixture. The stoichiometric ratio can be calculated in two different ways, firstly by using molecular weights and the functionality of the reactants, and also by the concentration of reactive functional group in the materials [88].

Mechanical properties of such prepared samples are quantified with a rheometer. Our results show that the low frequency storage modulus ($G_0$) of the network decreases with increasing stoichiometric ratio.

When the stoichiometric ratio is larger than 1, there are more number of moles of vinyl functional group present in the network than that of silane group. Such vinyl group molecules that are not cross-linked during the reticulation process, remain within the network. These molecules can migrate freely inside the network and are known to affect the wetting properties of soft surfaces [89]. For instance, Hourlier-Fargette, *et al.* showed that the free silicone oil molecules are extracted by a liquid droplet sliding on a soft PDMS surface, and change the dynamics of the sliding droplet [48]. Also, Jensen, *et al.* observed that the PDMS gel phase separates near the contact line during the adhesion with a rigid object and creates a four-phase contact zone with three contact lines [56]. Thus, it is important to quantify the amount of free uncross-linked silicone molecules present in the PDMS network in order to understand their role in wetting on soft surfaces. Extraction of the free silicone oil with solvent has been proved the most effective way to quantify the amount of uncross-linked molecules [89, 90, 91]. However, most of the literatures on the extraction of uncross-linked silicone oil mainly focused on stiff PDMS gels with elastic moduli between MPa and kPa. We will extend this technique to softer networks with tunable stoichiometric ratio, in the range of a few tens of Pa to kPa in elastic moduli.

Extraction ratio of soft PDMS samples in toluene and dichloromethane are recorded respectively. We show that the amount of extracted uncross-linked molecules remain constant within the error bar regardless of the stoichiometric ratio as long as the ratio is larger than 1.

## 4.2 Experimental methods

### 4.2.1 PDMS sample preparation

We use vinyl-terminated base polymers and trimethylsiloxane terminated (Methylhydrosiloxane)-dimethylsiloxane copolymer cross-linkers from Gelest, Inc. for preparation of samples. A small amount of platinum complex catalyst is also added to initiate the cross-linking. The chemical structures of the two polymers, and the catalyst are illustrated in Figure 4.1, and 4.2. The vinyl groups at both ends of a base polymer and a silane group of a cross-linker undergo a catalytic hydrosilylation reaction in the presence of platinum catalyst.

The samples are formulated based on the recipe from Jensen, *et al.* [56], which involves two premixes - part A, and B. Part A is a mixture of a base polymer and a catalyst. Part B is obtained by diluting a cross-linker into the same base, which are unreactive without the presence of catalyst. This part allows to prevent local cross-linking that could happen if drops of cross-linker were directly added into the base premix A. Such local cross-linking can be visualised as lumps in a mixture and can form inhomogeneous structures and disturb the curing of bulk elastomer [34]. Both parts A and B are degassed in a vacuum pump for approximately 1 minute. Once prepared, parts A and B are mixed together. The mixture is again degassed in a vacuum pump to prevent any change in cross-linking density due to the presence of air bubbles.

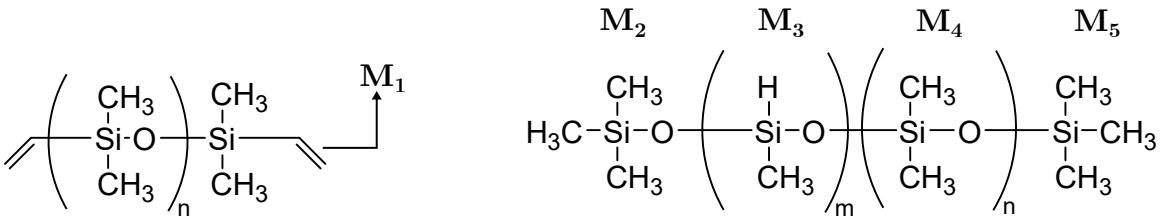


(a) (b)

Figure 4.1: Chemical structures of (a) a base polymer, and (b) a cross-linker from Gelest, Inc. Labels $M_1$ to $M_5$ refer to molecular weight of corresponding molecules

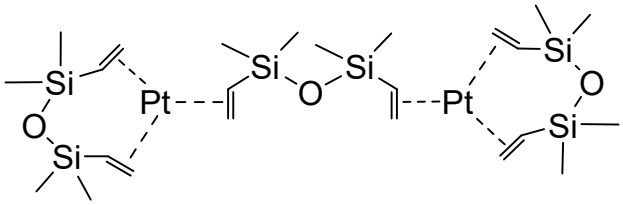


Figure 4.2: Chemical structure of platinum-divinyltetramethyldisiloxane complex catalyst (SIP6831.2)

| Label | Molecule | Molecular weight (g/mol) |
|---|---|---|
| $M_1$ | $CH{=}CH_2$ | 27.0 |
| $M_2$ | $SiO(CH_3)_3$ | 89.2 |
| $M_3$ | $SiOCH_3H$ | 60.1 |
| $M_4$ | $SiO(CH_3)_2$ | 74.2 |
| $M_5$ | $Si(CH_3)$ | 73.1 |

Table 4.1: Molecular weight of labelled molecules

| Base | Molecular weight, $M_{DMS}$ (g/mol) | Viscosity (mPa · s) | Number of reactive functional group |
|---|---|---|---|
| DMS-V22 | 9400 | 200 | 2 |
| DMS-V31 | 28000 | 1000 | 2 |
| DMS-V33 | 43000 | 3500 | 2 |

Table 4.2: Molecular weight, viscosity and the number of functional group in base polymers

| Cross-linker | Molecular weight, $M_{HMS}$ (g/mol) | Viscosity (mPa · s) | Mole % of reactive functional group, $N_{func}$ (%) | Equivalent weight, $W_{equiv}$ |
|---|---|---|---|---|
| HMS-053 | 22500 | 875 | 5.00 | 1475 |
| HMS-082 | 6000 | 130 | 8.00 | 925 |
| HMS-301 | 1950 | 30 | 30.0 | 245 |

Table 4.3: Molecular weight, viscosity, mole % of reactive silane functional group, and equivalent weight in cross-linkers

Molecular weight, viscosity, mole % of silane functional group, and equivalent weight of each materials are obtained from Reactive Silicones document from Gelest Inc. [92], and are recorded in Tables 4.2, and 4.3.

There are two different ways to find the number of moles of silane group m in a cross-linker. We will label those obtained from each method as $m_1$ and $m_2$.

### Equivalent weight ($W_{equiv}$) method

First method is by using an equivalent weight $W_{equiv}$. The equivalent weight of a polymer is the mass of polymer with one mole of reactive group (silane group in this case). $W_{equiv}$ of each cross-linkers are provided by Gelest, inc. [92]. Thus, we can easily calculate the number of moles of silane groups present by dividing the molecular weight of a cross-linker $M_{HMS}$ with its equivalent weight:

$$m_1 = \frac{M_{HMS}}{W_{equiv}}. \tag{4.1}$$

**Method with mole % amount of silane group ($N_{func}$)**

The second method is by using the percentage amount of silane group in a cross-linker $N_{func}$. The molecular mass contribution of the backbone ($m \times M_3 + m \times M_4$) of a cross-linker is equal to the molecular mass of the cross-linker substracted by molecular weights of two side molecules ($M_2$ and $M_5$):

$$m \times M_3 + n \times M_4 = M_{HMS} - M_2 - M_5. \tag{4.2}$$

The number of moles of backbone molecules in a cross-linker ($m + n$) is calculated by dividing total mass contribution of the backbone ($m \times M_3 + m \times M_4$) with the molecular mass of each backbone molecules times their mole percentage:

$$\begin{aligned} m + n &= \frac{(m \times M_3 + n \times M_4)}{\frac{N_{func}}{100} \times M_4 + \left(1 - \frac{N_{func}}{100}\right) \times M_3} \\ &= \frac{100 \times (m \times M_3 + n \times M_4)}{N_{func} \times M_4 + (100 - N_{func}) \times M_3}. \end{aligned} \tag{4.3}$$

Substituting Equation 4.2 into Equation 4.3 gives:

$$m + n = \frac{100 \times (M_{HMS} - M_2 - M_5)}{N_{func} \times M_4 + (100 - N_{func}) \times M_3}. \tag{4.4}$$

$m_2$ is then the total number of moles of backbone multiplied with the mole percentage of silane functional group:

$$m_2 = \frac{N_{func} \times (m + n)}{100}. \tag{4.5}$$

For accuracy of our calculation, we use an average of $m_1$ and $m_2$ as m.

| Cross-linker | $m_1$ | $m_2$ | m |
|---|---|---|---|
| HMS-053 | 15.3 | 15.2 | 15.2 |
| HMS-082 | 6.49 | 6.39 | 6.44 |
| HMS-301 | 7.96 | 7.67 | 7.81 |

Table 4.4: $m_1$, $m_2$, and m of cross-linkers used

All of the base polymers only have two vinyl functional groups at both end of their chain as illustrated in Figure 4.1(b), and thus, the number of moles of reactive functional group in base polymers is simply 2.

Ratio of the number of moles of silane group to that of vinyl group is expressed as:

$$\text{Mole ratio} = \frac{m}{2}. \tag{4.6}$$

Mass ratio of base polymer to that of cross-linker is the mole ratio multiplied with the ratio of

molecular mass of a base to that of a cross-linker:

$$\text{Mass ratio} = \text{Mole ratio} \times \frac{\text{M}_{\text{DMS}}}{\text{M}_{\text{HMS}}} \tag{4.7}$$

| Cross-linker | Mole ratio |
|---|---|
| HMS-053 | 7.61 |
| HMS-082 | 3.22 |
| HMS-301 | 3.91 |

Table 4.5: Mole ratio

| | HMS-053 | HMS-082 | HMS-301 |
|---|---|---|---|
| DMS-V22 | 3.18 | 5.05 | 18.8 |
| DMS-V31 | 9.48 | 15.0 | 56.1 |
| DMS-V33 | 14.6 | 23.1 | 86.1 |

Table 4.6: Mass ratio

Using the mole ratio from Table 4.5, we can calculate the mass ratio of base polymer and cross-linker and is recorded in the Table 4.6.

The stoichiometric ratio nA/nB is expressed as:

$$\frac{\text{nA}}{\text{nB}} = \frac{\frac{\mu_{\text{DMS}}}{\mu_{\text{HMS}}}}{\text{Mass ratio}} \tag{4.8}$$

when $\mu_{\text{DMS}}$ is the total mass of a base polymer and $\mu_{\text{HMS}}$ that of a cross-linker used. If $\frac{\text{nA}}{\text{nB}} > 1$, there is more vinyl group than silane group present in the mixture.

| Sample | Ingredients | nA/nB |
|---|---|---|
| 1 | 80.0wt% DMS-V22, 20.0wt% HMS-082 | 0.79 |
| 2 | 83.3wt% DMS-V22, 16.6wt% HMS-082 | 0.99 |
| 3 | 96.0wt% DMS-V33, 4.00wt% HMS-082 | 1.04 |
| 4 | 98.9wt% DMS-V31, 1.01wt% HMS-301 | 1.76 |
| 5 | 96.7wt% DMS-V31, 3.22wt% HMS-082 | 2.00 |
| 6 | 97.5wt% DMS-V22, 2.50wt% HMS-301 | 2.07 |
| 7 | 96.9wt% DMS-V31, 3.02wt% HMS-082 | 2.13 |
| 8 | 97.0wt% DMS-V31, 2.95wt% HMS-082 | 2.18 |
| 9 | 97.2wt% DMS-V31, 2.77wt% HMS-082 | 2.33 |
| 10 | 94.0wt% DMS-V22, 6.01wt% HMS-082 | 3.10 |
| 11 | 98.5wt% DMS-V22, 1.50wt% HMS-301 | 3.49 |
| 12 | 97.3wt% DMS-V31, 2.70wt% HMS-053 | 3.80 |
| 13 | 89.9wt% DMS-V31, 2.51wt% HMS-053 | 4.10 |

Table 4.7: Recipe of each samples in an increasing order of stoichiometric ratio nA/nB

PDMS samples are prepared with the ingredients listed in Table 4.7 and the stoichiometric ratio of each formulated sample is calculated with the above-mentioned methods.

### 4.2.2 Rheometry of prepared PDMS samples

Mechanical properties of each sample are measured with Anton Paar MCR 502 rheometer.

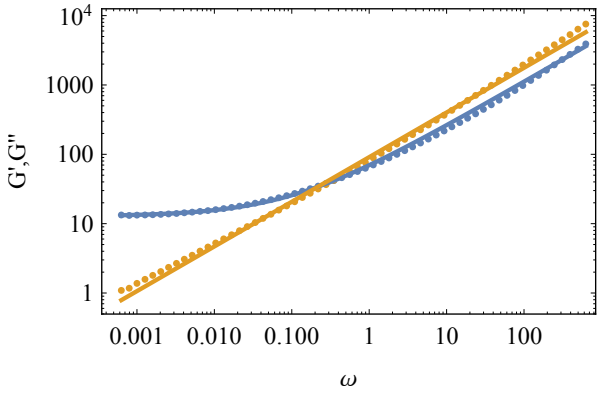


Figure 4.3: An examplary rheological measurement of a PDMS network. Storage modulus $G'$ (blue dots), and loss modulus $G''$ (dark yellow dots) are measured with varying rotational frequency $\omega$. Solid lines are fitting of measured data with a power law equation. We can extract low frequency storage modulus $G_0$, and relaxation time $\tau$ from this rheological data

An uncured mixture of elastomers is deposited between a ceramic (bottom) plate of the rheometer and the upper parallel plate (PP50 or PP25, according to their diameter) attached to the rotor of the rheometer. As the temperature of the rheometer can be controlled by a thermostat connected to it, the reticulation of this mixture is done within the apparatus. The curing protocol is described in Section 3.2.1.

Once the curing process completes, the tempearature of rheometer decreases to 20°C, and the rotor in which the upper plate is connected to shears the PDMS network with varying angular frequency $\omega$.

Figure 4.3 shows an exemplary frequency sweep rheological data of a PDMS gel. Blue datapoints indicate the measured storage moduli $G'$ and dark yellow points represent the measured loss moduli $G''$ with a change in angular frequency $\omega$.

At high frequency, the loss modulus $G''$ (yellow data) is higher than the storage modulus $G'$ (blue data), which indicates that the viscous portion of the sample is more dominant. As the rotational frequency decreases, the two moduli curves eventually intersect, and the elastic portion of the solid becomes more dominant (i.e. $G' > G''$). $G'$ starts to plateau after the intersection point. The frequency at which $G'$ and $G''$ cross is equal to $1/\tau$, when $\tau$ is the relaxation time. When a viscoelastic material is deformed by a high angular frequency, the elastic stress is stored within the material and is relaxed through a rearrangement of the molecules or particles. During the relaxation, the elastic stress is converted to a viscous stress due to the friction between these microstructures. The viscous stress is dissipated within the material as a form of heat. As discussed in Section 3.2.1, real viscoelastic materials such as PDMS have a spectrum of relaxation times, and their complex moduli can be expressed in a power law form with an exponent $n$:

$$G^* = G_0(1 + (i\omega\tau)^n), \tag{4.9}$$

where $G_0$ is a low frequency storage modulus (a $G'$ at $\omega = 0$). The rheological spectrum such

as Figure 4.3 is then fitted with the Equation 4.9 to extract the quantities of $G_0$, $\tau$, and $n$. The fit is represented by the two solid lines in Figure 4.3.

$G_0$ lets us to predict the stiffness of the sample, and the longest relaxation time of the material $\tau$ can be useful for predicting the viscoelastic response of the material when stressed for a given period of time.

The entanglement molecular weight of a polymer is defined as the molecular weight between entanglements (see Section 2.3.1). For the base polymers with molecular weight below the entanglement threshold, they tend to produce PDMS gels with exponents $n$ between 0.4 and 0.7 [93]. In contrast, the pre-polymers above the entanglement molecular weight form gels with lower rheological exponents between 0.2 and 0.4 [93]. The stoichiometry between the two reactive functional groups are known to affect the exponent $n$ of these two categories [93] .

We also observe a deviation of measured loss modulus from power law at small angular frequency $\omega$ as illustrated in Figure 4.3. Such deviation can be explained by a minimum instrument torque limit. The rheometer instrumental limit will be further discussed in Section 4.4.

### 4.2.3 Extraction of uncross-linked molecules

Approximately 4 g of uncured PDMS sample mixture is poured into a glass bottle of volume 50 mL and is reticulated in the oven for two days. A solvent is then poured onto the cured PDMS network. We use toluene and dichloromethane (DCM) as extracting solvents, as PDMS is soluble in both solvents [57].

The degree of swelling of silicone network is determined by the balance between the elastic force of the networks and the thermodynamic mixing interaction between the swelling solvent and the network as explained earlier in Section 3.1.2 [65]. According to the Flory-Rehner theory (see Equation 3.13), The larger the degree of cross-linking (i.e. smaller molecular mass between the cross-links indicated as $M_c$ in Equation 3.13), the less swelling of the PDMS is observed [65]. The complete swelling occurs when these two contributions (thermodynamic and elastic) are in equilibrium. The maximum swelling of the network creates a chemical potential gradient between the network and the solvent, leading to the migration of the uncross-linked molecules to reduce the difference of chemical potential between the swelling solvent and the PDMS gel. Hence, it is necessary to have a large amount of solvent compared to the sample (around 10 times more in volume) to maintain the difference in chemical potential [89].

The glass bottle is closed with a screw cap afterwards to prevent any solvent evaporation. After 72 hours, the solvent is poured out from the bottle, and the swelled PDMS gel is dried under a fumehood for 48 hours (without the cap) to let the remaining solvent to evaporate. The 48 hours of minimum solvent evaporation period is determined by the plateau of the final mass of the gel measured over a period of a week. The mass of the gel before and after swelling is measured, and the swelling ratio $n_{swell}$ is determined as:

$$n_{swell} = \frac{M_{sf}}{M_{ef}}, \tag{4.10}$$

where $M_{sf}$ is the final mass of the gel after swelling and pouring the solvent out, and $M_{ef}$ refers to the final mass of the gel after an evaporation of the solvent. Similarly, the extraction ratio $n_{ext}$ is given as:

$$n_{ext} = 1 - \frac{M_{ef}}{M_i}, \tag{4.11}$$

when $M_i$ is the initial mass of the gel before adding the solvent. The same swelling and extraction processes are repeated three times for every measurement until the mass remains constant, and the final $n_{swell}$, and $n_{ext}$ are the average of the ratio obtained after every measurement.

## 4.3 Results and discussion

### 4.3.1 Mechanical properties of prepared PDMS samples

| Sample | 1 | 2 | 3 | 4 | 5 | 6 | 7 | 8 | 9 | 10 | 11 | 12 | 13 |
|---|---|---|---|---|---|---|---|---|---|---|---|---|---|
| nA/nB | 0.79 | 0.99 | 1.04 | 1.76 | 2.00 | 2.07 | 2.13 | 2.18 | 2.33 | 3.10 | 3.49 | 3.80 | 4.10 |
| $G_0$[Pa] | 332000 | 136000 | 13600 | 2180 | 343 | 9580 | 185 | 118 | 24.0 | 29.1 | 94.7 | 301 | 157 |
| $\tau$[s] | - | - | 0.00781 | 0.0250 | 0.129 | - | 0.276 | 0.518 | 3.76 | 0.608 | 0.0943 | 0.0776 | 0.184 |

Table 4.8: Low frequency storage modulus $G_0$, and relaxation time $\tau$ in an increasing order of stoichiometric ratio nA/nB

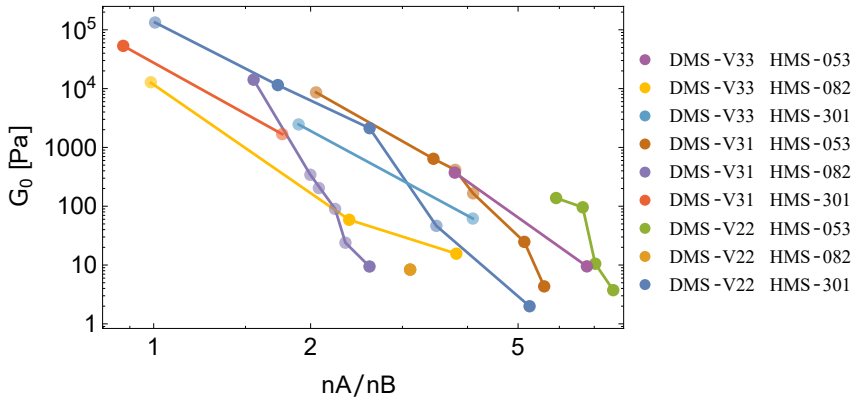


Figure 4.4: Low frequency storage modulus ($G_0$) vs stoichiometric ratio nA/nB for each material combination. Data from Table 4.8 are represented as the transparent points

In Figure 4.4, we present the stoichiometric ratio dependence of the PDMS network stiffness. This also includes the samples that are not used in the swelling and extraction experiments. The datapoints of the 13 samples mentioned in the Table 4.8 are represented as the transparent points in this plot. The low frequency storage modulus $G_0$ of our PDMS samples decreases with an increase in the stoichiometric ratio nA/nB between vinyl and silane functional groups for every material combination.

As already discussed in Section 4.2.1, the uncross-liked chains are still present within the network when nA/nB $>$ 1, i.e. there is an excess of vinyl funtional group. With very few cross-linked polymers, we expect these gels to be soft. In other words the smaller the cross-linking density, the smaller the elastic modulus. The measurements we have obtained for the samples

presented above are thus consistent with our expectation.

Furthermore, Figure 4.4 highlights that we can formulate elastomers with stiffness spanning over almost four decades of elastic moduli by using the same ingredients but simply by altering their mass percentage in the mixture.

The effect of the mole % of a reactive functional group in the cross-linker and the base polymer molecular weight on the stiffness of samples will be discussed in detail later in Section 4.4.

### 4.3.2 Degree of swelling and extraction of PDMS networks

As mentioned in the beginning, the presence of uncross-linked silicone molecules within the PDMS network is known to affect the wetting behaviour of the PDMS surface. Since our formulated PDMS networks are expected to contain a large amount of uncross-linked chains, it is important to quantify their amount.

It has been already studied that the swelling of PDMS changes significantly with a change of base polymer/cross-linker ratio [94, 95, 96]. Stafie, *et al.* observed the degree of swelling of PDMS membranes ($G_0$ =0.35, 0.50, and 0.77 MPa) in hexane according to the base polymer/cross-linker ratio [66]. When the chain length between the networks is shorter (i.e. higher storage modulus), the elastic resistance to the swelling stress get stronger, and thus the amount of swelling will be less [66].

| Sample | $n_{swell}$ | $n_{ext}$ |
|---|---|---|
| 1 | 5.38 | 0.0380 |
| 2 | 6.35 | 0.106 |
| 3 | 11.05 | 0.282 |
| 4 | 7.16 | 0.410 |
| 5 | 6.85 | 0.374 |
| 6 | 8.27 | 0.583 |
| 7 | 8.64 | 0.491 |
| 8 | 6.28 | 0.305 |
| 9 | 7.18 | 0.339 |
| 10 | 12.2 | 0.519 |
| 11 | 4.68 | 0.313 |
| 12 | 6.07 | 0.431 |
| 13 | 6.28 | 0.407 |

Table 4.9: Swelling and extraction ratio of elastomer samples in Toluene

| Sample | $n_{swell}$ | $n_{ext}$ |
|---|---|---|
| 1 | 7.50 | 0.0329 |
| 2 | 6.81 | 0.169 |
| 3 | 16.0 | 0.197 |
| 4 | 8.23 | 0.331 |
| 5 | 13.5 | 0.617 |
| 6 | 9.60 | 0.438 |
| 7 | 7.63 | 0.302 |
| 8 | 12.4 | 0.550 |
| 9 | 12.2 | 0.468 |
| 10 | 9.38 | 0.507 |
| 11 | 6.53 | 0.367 |
| 12 | 9.25 | 0.520 |
| 13 | 10.1 | 0.559 |

Table 4.10: Swelling and extraction ratio of elastomer samples in DCM

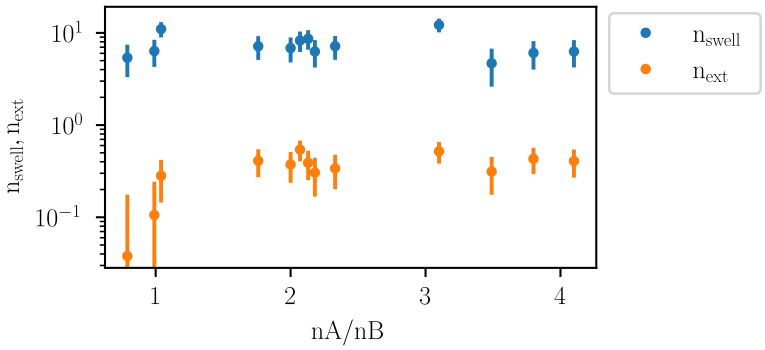


(a)

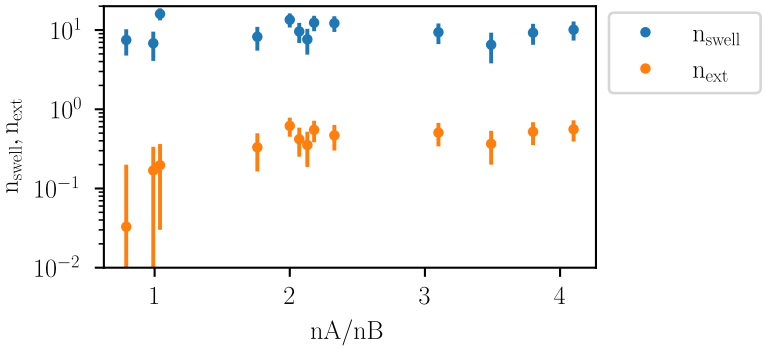


(b)

Figure 4.5: $n_{swell}$, and $n_{ext}$ of PDMS samples with their corresponding stoichiometric ratio nA/nB in (a) toluene, and (b) DCM

Figure 4.5 shows the swelling and extraction ratios as a function of the corresponding nA/nB, for our samples immersed in toluene and DCM. The error bar has been obtained by determining the standard deviation of the presented data. We can observe two distinct regimes for $n_{ext}$. For nA/nB $< 1$, almost no free oligomer chains are extracted by the both solvents, and the amount starts to drastically increase with an increase in stoichiometry. On the other hand, the extraction ratio of PDMS elastomers starts to saturate from nA/nB $> 2$, regardless of the solvent used. This implies that the degree of extraction does not depend on nA/nB when there is a large stoichiometric unbalance in the PDMS mixture.

In order to study the effect of elastic moduli on $n_{swell}$ of PDMS samples, we also present the ratios as a function of storage modulus $G_0$ in Figure 4.6. Our result shows that the degree of swelling $n_{swell}$ is independent of $G_0$, being inconsistent with the observation of Stafie, *et al.* However, we need to note that the experiment by Stafie, *et al.* only used very stiff gels with $G_0$ in magnitude of MPa, at least ten times larger than the stiffest PDMS sample prepared by us.

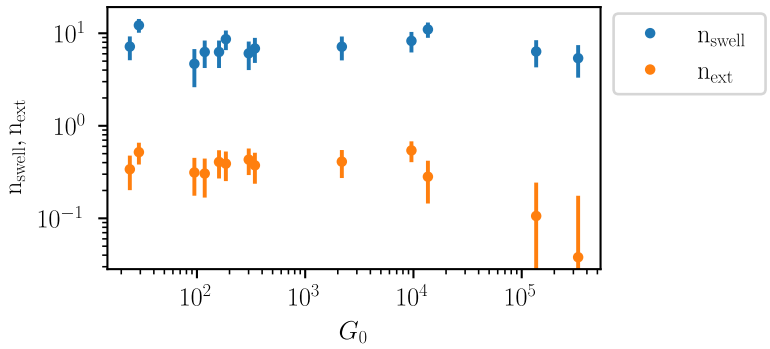


(a)

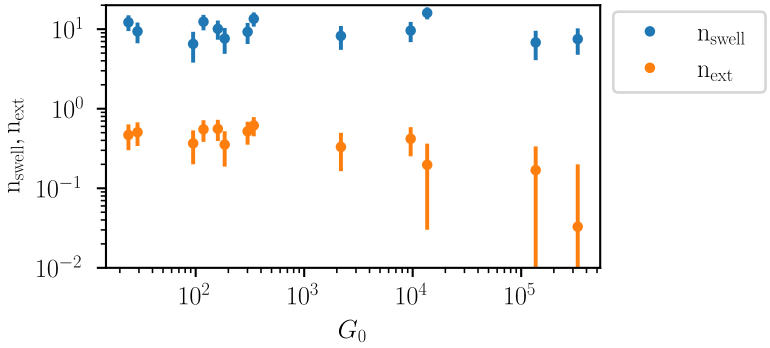


(b)

Figure 4.6: Swelling ratio, and extraction ratio of gels with corresponding $G_0$. Top: Toluene, Bottom: DCM

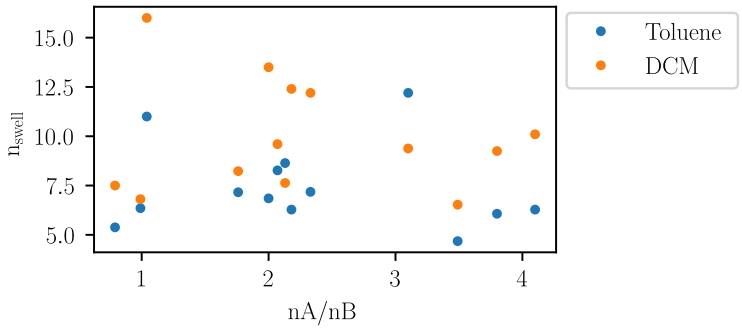


Figure 4.7: $n_{swell}$ of samples swollen in toluene and DCM as a function of stoichiometric ratio nA/nB

Continuing the study of the degree of swelling of samples, we compare $n_{swell}$ of PDMS networks in toluene and DCM in Figure 4.5. The swelling ratio of most of the samples swelled in DCM is approximately 1.5 times higher than that swelled in toluene.

On the other hand, Lee, *et al.* found that the degree of swelling of solid Sylgard 184 PDMS ($G_0 \approx 1628\,kPa$) is slightly higher in toluene ($n_{swell}$=1.31) than in DCM ($n_{swell}$=1.22) [57]. It is important to note here that they determined the swelling ratio by comparing the length of PDMS samples before and after swelling, instead of comparing the mass like in our study. Such approach is not feasible with our very soft gels, as they cannot be detached easily from the glass bottles. The difficulty of removing the soft gels from the glass surface is not a surprising phenomenon, as studied by Tiwari, *et al.* in 2017 [97]. They investigated the adhesion between PDMS elastomers and glass or acryllic balls based on Johnson-Kendall-Roberts (JKR) theory. It was found that the work of adhesion increased by a factor of two for the glass ball pulled away from a soft PDMS surface when compared to that for the smooth acrylic ball [97]. On the other hand, the opposite trend of the work of adhesion was observed in a rigid PDMS surface, in which it decreased by a factor of 700 for the glass ball [97].

Also, fracture of our prepared PDMS samples is observed during the swelling procedure. For the soft PDMS gels, the degree of swelling (between 5.0 and 15.0 for most of our samples) is much higher than that of stiff networks from Lee, et al (around 1.3). Thus, they need a large container to accommodate such large amount of swelling. Fracture of the samples can occur if the container is not large enough [89]. When the small fractions of fractured soft gels are present on the surface of swollen PDMS network within the solvent, it becomes more difficult for us to pour away the remaining solvent without removing those small fractions of gels at the same time. Thus, we always leave a small portion of solvent inside the sample before evaporating the sample to measure extraction ratio to prevent any loss of swollen gels. This affects the final mass of swollen samples, possibly explains the discrepancy of our data from the literature of Lee, *et al.* [57], and Stafie, *et al* [66].

| | Toluene | DCM |
|---|---|---|
| $n_{swell}$ | 6.12 | 12.4 |
| $n_{ext}$ | 0.411 | 0.462 |

Table 4.11: Degree of swelling and extraction of CY52-276 A:B=1:1

The swelling and extraction ratio of Dow-Corning CY52-276 sample with a mixing ratio A:B=1:1 ($G_0 = 1050\,Pa$) are also measured and recorded in Table 4.11. Looking at the high $n_{ext}$ of the sample in both solvents, we can deduce that the stoichiometric ratio of the gel is above 1. The degree of network swelling is again a few times larger than that presented by Lee, *et al.*, and $n_{swell}$ of the sample in DCM is approximately 2 times larger than that swollen in toluene. This again emphasises that the swelling ratio depends on the storage modulus of the sample.

### 4.3.3 Conclusion

We have successfully formulated PDMS networks of different mechanical properties with a in-house recipe involving a stoichiometric ratio of vinyl and silane functional groups. A wide range of achievable gel stiffness highlights the versatility of our method.

With such gels, we observe an increase in the amount of extracted uncross-linked molecules at lower stoichiometric ratio and a saturation of this quantity at higher ratio. This result shows that the extraction of free oligomers by using a large amount of solvent can not be used to determine the degree of cross-linking for soft PDMS gels. Also, the degree of swelling that is a few times larger than that reported in the literature shows that the swelling ratio heavily depends on the stiffness of the PDMS network.

### 4.3.4 Outlook

There has been a growing interest in the role of uncross-linked silicone oils at the contact line of soft deformable PDMS surfaces [48, 49, 50]. In order to understand this phenomenon, quantifying the mechanical properties of PDMS networks without the excess uncross-linked molecules is necessary. For very soft PDMS materials, extraction of free oligomers inside a closed container leads to destruction of the orignial shape of the PDMS solid [89], as already explained in Section 4.3.2. Also, the gel can exfoliate during its rapid drying process (as the solvent evaporates) [98]. Cracks on the surface of the swollen gel are formed due to the shrinking of the gel upon drying, and propagate into the bulk of the gel as the drying progresses. A thin superficial layer peels off and exposes the bare surface of the gel underneath [98].

Thus, the extracted PDMS samples can not be used for further analysis of their mechanical properties due to the failure to retain their original shape.

Glover, *et al.* recently suggested an interfacial extraction set up that yields a similar amount of extracted molecules as the closed container method but retains the original shape of the network for Sylgard 184 PDMS samples with elastic moduli up to 7 kPa [89]. A water soluble layer of polyacrylic acid (PAA) is coated on a glass substrate, followed by a thin film of PDMS layer via spin coating. After reticulation of the PDMS layer, the prepared substrate is floated on a water bath, and the PAA layer dissolves over time, leaving the cured PDMS thin layer floating alone on top of the water surface (as the density of PDMS is similar to that of water) [49]. A solvent is then introduced onto the PDMS surface to swell the network. The water bath is sealed with a lid (or aluminum foil) to prevent evaporation of the solvent [89].

The same methodology could also be used for swelling and extraction of very soft PDMS solids from our formulation recipe. The mechanical properties of the soft gels after a removal of free silicone chains will then be quantified with a rheometer.

Beyond the high potential of such deformable surfaces to tackle soft wetting problems as will be presented in Chapter 6, there is also a strong relevance of the soft gels for biological implication. Indeed, a soft PDMS surface can serve as a model soft in-vitro environment with its stiffness comparable to the brain tissues, as we will describe in the next chapter.

## 4.4 Appendix

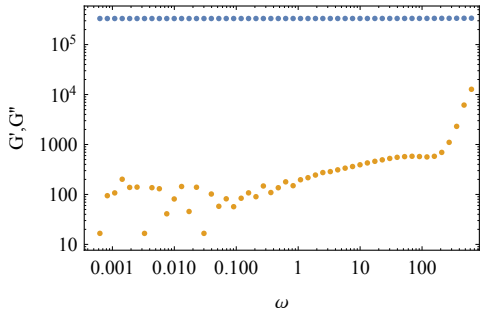


(a) $G_0 = 332000$ Pa

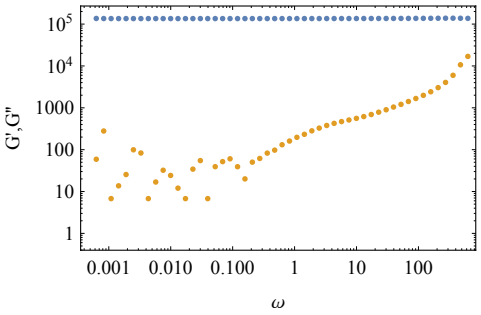


(b) $G_0 = 136000$ Pa

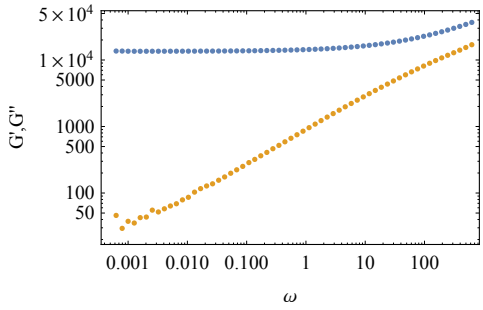


(c) $G_0 = 13600$ Pa

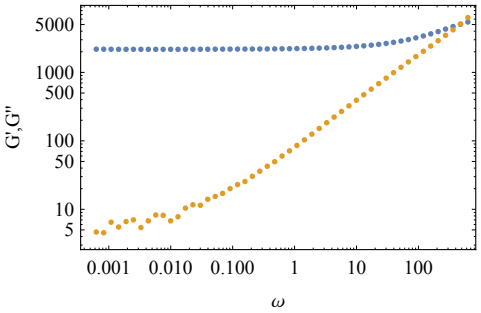


(d) $G_0 = 2180$ Pa

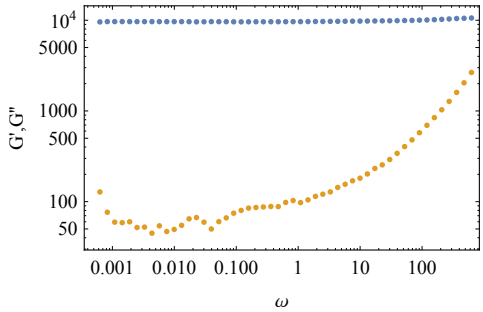


(e) $G_0 = 9580$ Pa

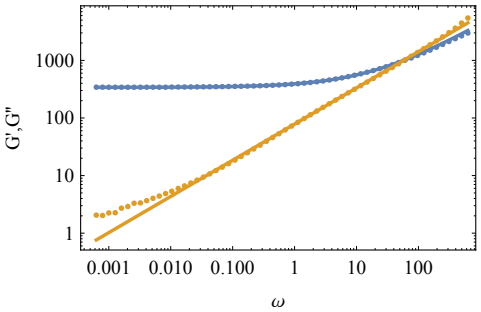


(f) $G_0 = 343$ Pa

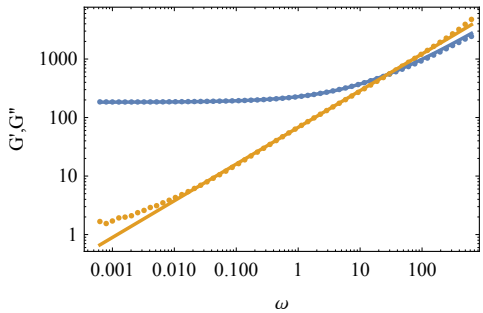


(g) $G_0 = 185$ Pa

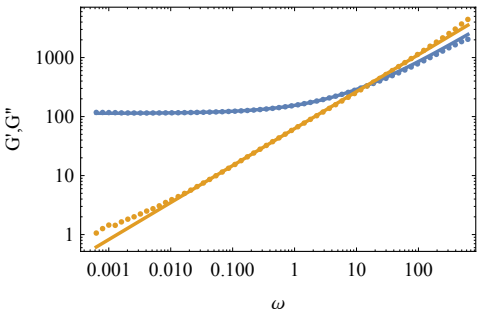


(h) $G_0 = 118$ Pa

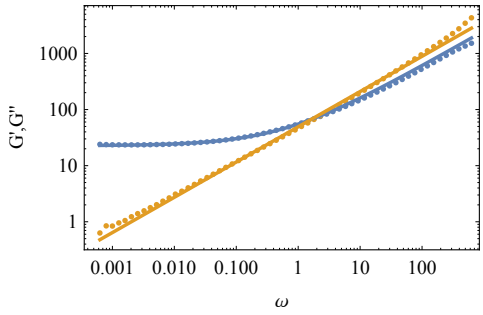


(i) $G_0 = 24.0$ Pa

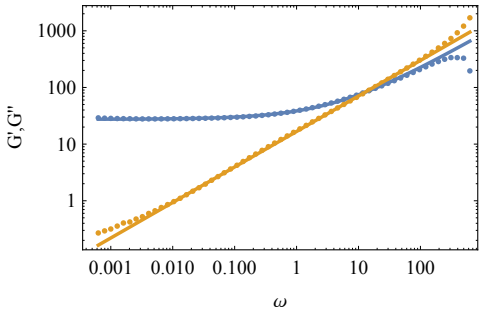


(j) $G_0 = 29.1$ Pa

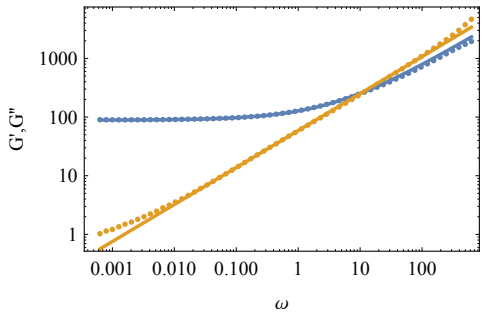


(k) $G_0 = 94.7$ Pa

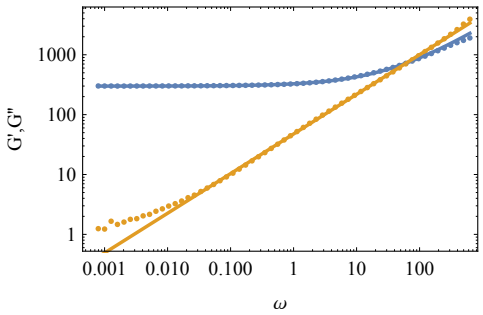


(l) $G_0 = 301$ Pa

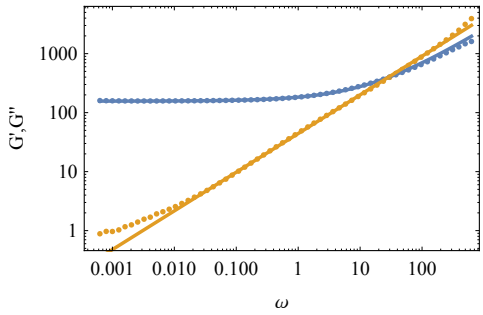


(m) $G_0 = 157$ Pa

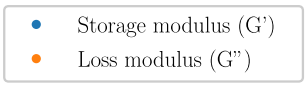


Figure 4.8: Rheology of prepared samples in order of decreasing stoichiometric ratio

The solid lines in the rheology plots of softer samples indicate the fit of power law equation $G^* = G_0\,(1 + (i\omega\tau)^n)$ with the measured moduli. As mentioned briefly in Section 4.2.2, the loss moduli of most of the PDMS samples deviate from power-law behaviour at low angular frequency $\omega$ region, typically below $\omega = 0.010\,\text{rad/s}$, when $G'' < 10\,\text{Pa}$.

Ewoldt, *et al.* described commonly faced challenges when measuring the mechanical properties of materials with a rotational rheometer [99]. Figure 4.9 indicates instrumental error regions for the rheometry of hagfish gel ($G'' \approx 0.2\,\text{Pa}$ in a concentric cylinder measurement geometry. The possible sources of measurement error are insturmental low torque limit for small angular frequency $\omega$ region, and inertial effects from the instrument at high $\omega$ region.

For our system the main error arises from the instrumental torque limit [99]. This torque limit is usually provided by the manufacturers. For our Anton Paar MCR 502 rheometer, the given minimum rotation torque limit is as $100\,\text{nN m}$. The minimum measurable shear stress $\tau$

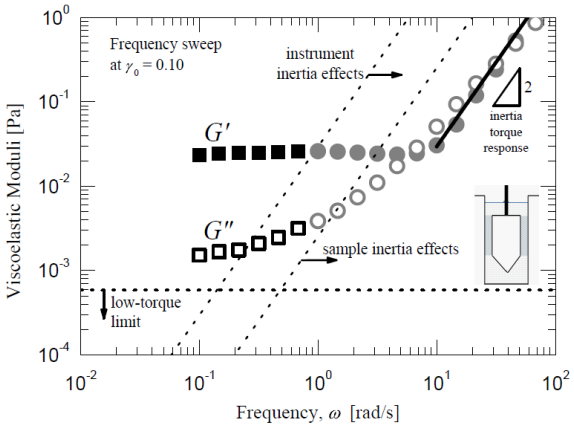


Figure 4.9: Low torque and instrument limit for oscillatory frequency sweep measruement of soft hagfish gel. Republished with permission from [99]

is proportional to the minimum torque $T_{\min}$ with conversion factor $F_\tau$:

$$\tau = F_\tau T_{\min}. \tag{4.12}$$

For a frequency sweep rheology with constant shear strain $\gamma_0$ (0.01 for our case), the minimum measurable moduli $G_{\min}$ is expressed as:

$$G_{\min} = \frac{F_\tau T_{\min}}{\gamma_0}, \tag{4.13}$$

$G_{\min}$ can be either $G'$ or $G''$ but is usually the loss moduli $G''$ for our system.

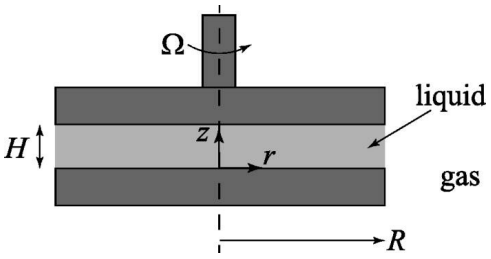


Figure 4.10: Dimensions of a sample sandwiched between a top parallel plate and bottom ceramic plate, Ω here refers to the torque $T$. Republished with permission from [100]

The conversion factor $F_\tau$ is expressed as:

$$F_\tau = \frac{1}{2\pi R^2 L}. \tag{4.14}$$

Referring to the schematic description of parallel plate geometry in Figure 4.10, $R$ refers to the radius of upper parallel plate for our geometry, and $L$ is the minimum gap (the height of the deposited sample). For our rhelogical measurement set up, $R = 25\,\text{mm}$, and $L = 0.5\,\text{mm}$. Calculating the Equation 4.13 by plugging in the given values gives $G_{\min} = 5.10\,\text{Pa}$, which indeed falls into the region below which the loss moduli deviates away from the power-law.

The same estimation can then possibly be used for the maximum measurable moduli. Look-

ing at the measurable moduli dependence of geometry plate radius $R$, $G$ increases with a decrease in $R$. Thus, a measuring geometry with smaller plate radius can be used for more precise measurement of stiff gels.

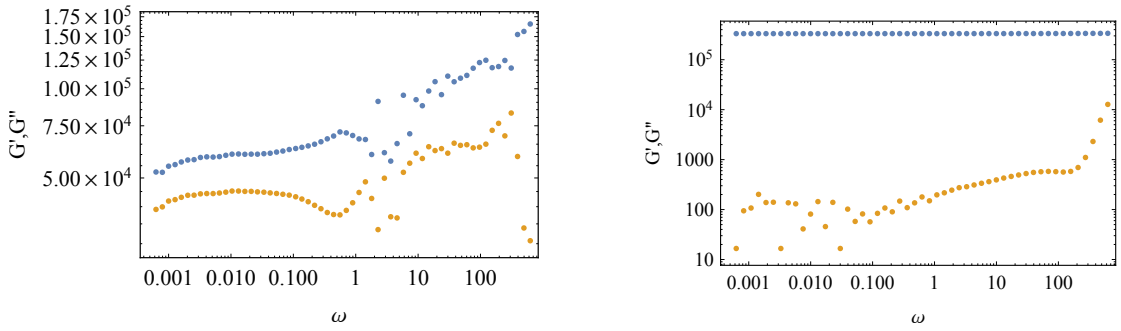


Figure 4.11: Rheological measurement of Sample 1 with (a) PP50 ($R = 25\,\text{mm}$), and (b) PP25 ($R = 12.5\,\text{mm}$

Indeed, as depicted in Figure 4.11, we obtain a more reliable rheological data of the stiffest gel of the samples when measured with a parallel geometry plate (PP25) with $R = 12.5\,\text{mm}$. Also, larger low frequency storage modulus $G_0$ is obtained from the measurement with PP25.

Figure 4.12 shows $G_0$, $\tau$, and exponent n of PDMS gels from the rheological measurements. Datapoints of the samples that are used for swelling and extraction experiments are made transparent in Figure 4.12 (a). As these experiments require a large volume of solvents in every step, not all of the prepared elastomers are used in these measurements. The samples from almost every material combination, and those with very different stoichiometric ratio are chosen for the swelling and extraction process.

In order to describe how does the storage modulus of the gel depend on the base polymer molecular weight or the concentration of reactive functional group in cross-linker, a red dashed vertical line that crosses the most number of ingredient combinations is drawn across the plot in Figure 4.12 (a). When we compare the storage moduli along this vertical line of different material combination, we find that networks formed with DMS-V22 base polymer have the smallest storage moduli, followed by DMS-V31, and DMS-V33. Referring to Table 4.2, we can conclude that $G_0$ of the network depends on the molecular weight of base polymer. The higher the molecular weight of the base polymer, the stiffer the network.

On the other hand, the concentration of silane group in a cross-linker does not seem to affect the storage modulus of the network. PDMS elastomers formulated with HMS-082 have the smallest $G_0$, followed by those with HMS-301, and HMS-053. However, the mole percentage of reactive silane group of HMS-053 is the smallest, and that of HMS-301 is the largest.

The amount of reactive functional group per molecule, though, seem to affect the storage modulus of the gel. HMS-053 has almost double the amount of silane functional group per molecule as compared to HMS-082 and HMS-301 (see Table 4.5). Thus, it is reasonable to observe higher storage moduli of the PDMS gels prepared with HMS-053 cross-linker than the others with HMS-082 and HMS-301.

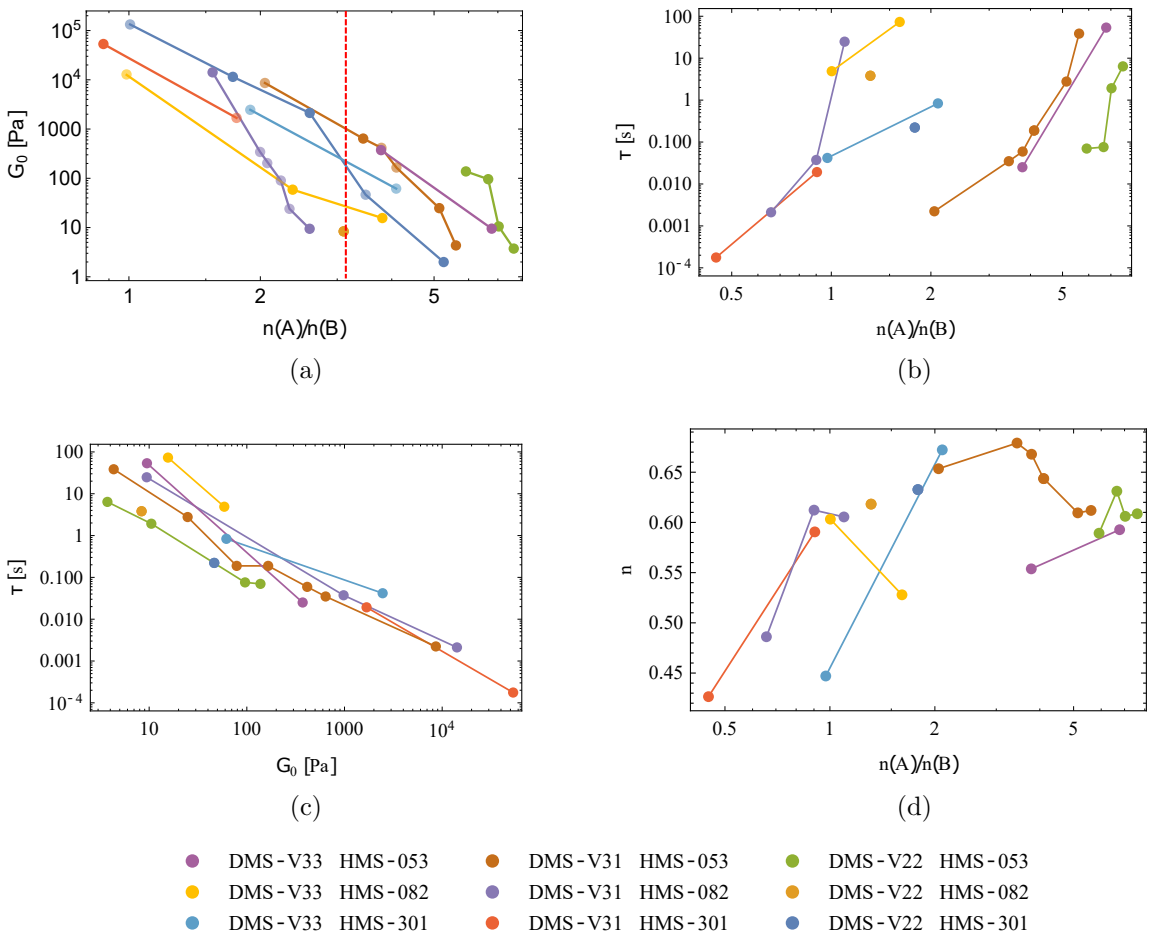


Figure 4.12: Plots of rheological quantities (a) low frequency storage modulus $G_0$, (b) relaxation time $\tau$, and (d) exponent n of PDMS gels as a function of stoichiometric ratio between vinyl and silane groups nA/nB. (c) Relationship between $\tau$ and $G_0$. These four plots also include rheological measurements from the gels that were not used in the extraction process. For (a): measurements from the samples used for swelling and extraction are blurred, and the red dashed line crosses the most number of ingredient combinations and will be used later in this section

Figure 4.12 (b), and (c) show an increase of relaxation time $\tau$ as a function of stoichiometric ratio, and a linear decrease as a function of $G_0$, as already explained in 4.2.2.

# Chapter 5

# Liquid-liquid phase separation of tau protein droplets on a soft PDMS surface

## 5.1 Motivation

Within any eukaryotic cell, a plethora of organelles can be found. These organelles, acting as compartments, contain elements of the biomolecular machinery of the cell and carry specific functions. Organelles are usually enclosed by their own membrane, composed of a phospholipid bilayer [101]. There are also organelles that are not bound by these traditional lipid bilayers, and thus they are called membrane-less organelles [102]. Membrane-less organelles such as P granules, nucleoli, or stress granules possess the typical characteristics of liquids and are formed via liquid-liquid phase separation [103]. This process allows rapid and reversible condensation of specific proteins and nucleic acid molecules into compartments in which biomolecular exchanges with the surrounding cytoplasm and nucleoplasm occur [104].

Among these different proteins, we can find tau proteins which are microtubule-associated and located in the membrane-less organelles of human brain cells. Wegmann, *et al.* suggested that tau proteins can undergo liquid-liquid phase separation within the cellular environment and that phase separated tau droplets can cause aggregation of these proteins [105]. Such abnormal changes of the proteins conformation are known to cause neuro-degenerative diseases like Alzheimer's and dementia [104].

In this context, we aim to understand the liquid-liquid phase separation of tau proteins on brain tissues. Owing to their liquid-like behaviour, it is reasonable to use liquid droplets as a simple model system to mimic membrane-less organelles. Brain tissues on the other hand are very complex biological structures made of many different types of cells. These tissues are among the softest ones within the human body with a typical elastic modulus of 0.5-1 kPa [106, 107, 108]. The production of model systems that are able to capture the complexity of brain tissues usually requires heavy tissue engineering or microfluidic tools [109]. In our approach, we propose a soft in-vitro model environment with a stiffness comparable to the brain tissue.

## 5.2 Experimental methods

### PDMS substrate preparation

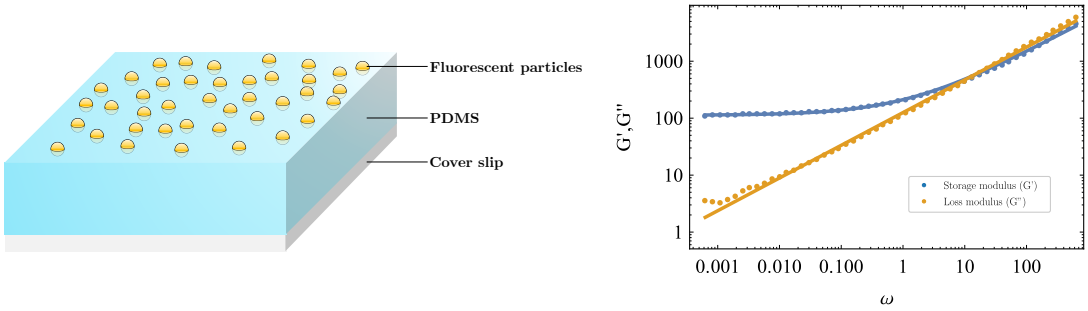


(a) (b)

Figure 5.1: (a) 3D representation of a model system for soft in-vitro environment: a flat PDMS substrate is coated on a glass slide and fluorescent particles are deposited at the gel surface. (b) Rheology of the soft silicone mixture used. The stiffness of the gel is $G_0 = 113\,\text{Pa}$.

In order to prepare very soft surfaces, Dow-corning CY52-276 PDMS A and B are mixed in a ratio of 1.3:1 to form a silicone gel. The prepared and still uncured PDMS mixture is then coated on a glass cover slip (dimension: 24mmx24mm) with a spin coater at a rotational frequency of 3000 rpm for 38 s to achieve a final thickness of about 100 µm. Finally the gel is cured in an oven at 75°C for two days. The cured PDMS substrate is then dip coated in a solution of fluorescent particles for one minute, to form a layer of tracers at the top of the gel as illustrated in Figure 5.1 (a). The fluorescent particles are water-soluble carboxylate-modified microspheres with a diameter of 100 nm (FluoSpheres™ from Invitrogen™). The presence of these particles allows to track the deformation of the soft surfaces with a confocal microscope, as described later.

To characterise the mechanical properties of our PDMS surfaces, we have extracted the rheology of a small amount of the very same cured gel with a rheometer (Anton Paar MCR 502). Figure 5.1 (b) shows a typical rheology of this PDMS mixture. The low frequency storage modulus ($G_0$) of the elastomer is 113 Pa, which is compatible with the stiffness of brain tissues. We note here that the rheology of the gel is obtained without any fluorescent particles added to the PDMS. As the size of the fluorescent particles is negligible compared to the thickness of the substrate, we assume that they do not affect the rheology of the PDMS gel.

### Tau protein droplet formation

Tau proteins are fluorescently labelled with a Microscole Protein Labeling Kit (Alexa Fluor™ 488 from Invitrogen™). An assay buffer, made of a mixture of 25mM HEPES and 2mM DTT, is mixed with the labelled tau proteins and 60nM Polyuridylic acid (from Sigma-Aldrich). The phase separation of tau proteins is induced by addition of 2.5% crowding agent dextran T500 (from Pharmacosmos).

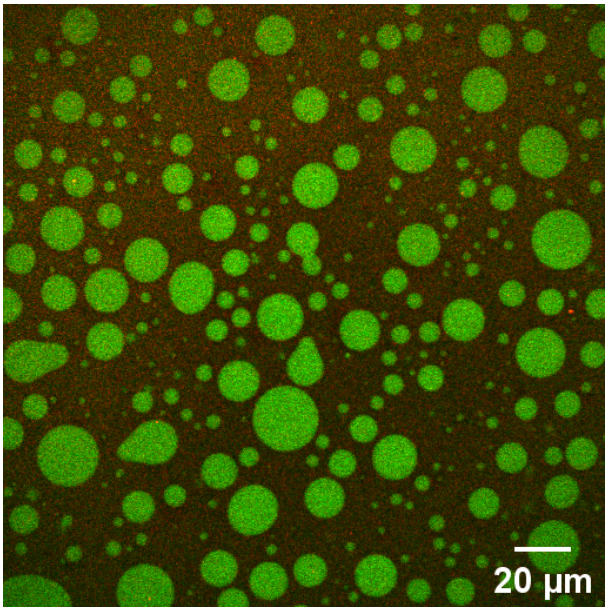


Figure 5.2: Laser confocal microscope image of tau protein droplets sitting on a PDMS substrate. On this image, the droplets are seen in green and the surface in red. Non-spherical droplets are the coalescing droplets

A drop of the prepared mixture is finally deposited on the PDMS substrate. Due to the immiscilibity of tau protein droplets in the buffer solution, the freshly deposited drop then phase separates into smaller droplets. Coalescence events of these droplets and their corresponding z-stack profiles are recorded at 0.9 fps with an Olympus Fluoview laser fluorescence confocal microscope equipped with 60x objective. An example of acquired confocal image in the plane of the gel surface is shown in Figure 5.2. The surface of the PDMS substrate is observed in the red fluorescent channel and the green fluorescent channel of the image shows tau protein droplets. These droplets exhibit a spherical shape before or after a coalescence event, and an elliptical (or non-spherical) shape during the process of coalescence.

## 5.3 Results and discussion

The coalescence dynamics of liquid drops, or membrane-less organelles, is mainly determined by two important parameters: surface tension and viscosity [103]. This ubiquitous phenomenon have been the subject of numerous studies, especially on the initial coalescence of two liquid droplets [110, 111, 112]. Let us now briefly summarise the main theoretical elements needed to understand droplet coalescence.

Two distinct stages are observed during the coalescence of sessile drops on a substrate: a rapid initial growth of the liquid meniscus bridge between the drops, followed by a slow rearrangement of the shape of the combined drop from elliptical to circular shape [113].

The coalescence phenomenon of sessile drops is different from that of suspended drops due to the geometry. Suspended drops are axisymmetric [110, 114], whereas sessile drops are anisotropic as the symmetry breaks due to the presence of a substrate and thus a contact line [115]. For instance, the growth rate of the meniscus bridge between two suspended drops

depends very weakly on the size of the drop, however the size dependence is more significant for the sessile drops.

Ristenpart, *et al.* investigated the early stage of the coalescence dynamics of viscous liquid droplets, for which spreading on a substrate is driven by surface tension [113]. They observed, both experimentally and numerically, that the width $d$ of the liquid meniscus bridging two merging droplets is governed by a simple scaling law:

$$d = \left(\frac{\gamma h_0^3}{\mu R_0^2} t\right)^{1/2} \tag{5.1}$$

where $\gamma$ is the surface tension, $\mu$ is the dynamic viscosity, $R_0$, and $h_0$ are the drop radius, and height respectively.

In our experiments, we characterise the coalescence of two tau protein droplets by measuring the associated temporal evolution of the diameter of liquid meniscus bridge. Also, we show how the capillary velocity $\gamma/\mu$ of the coalescing droplets can be calculated from our measurements.

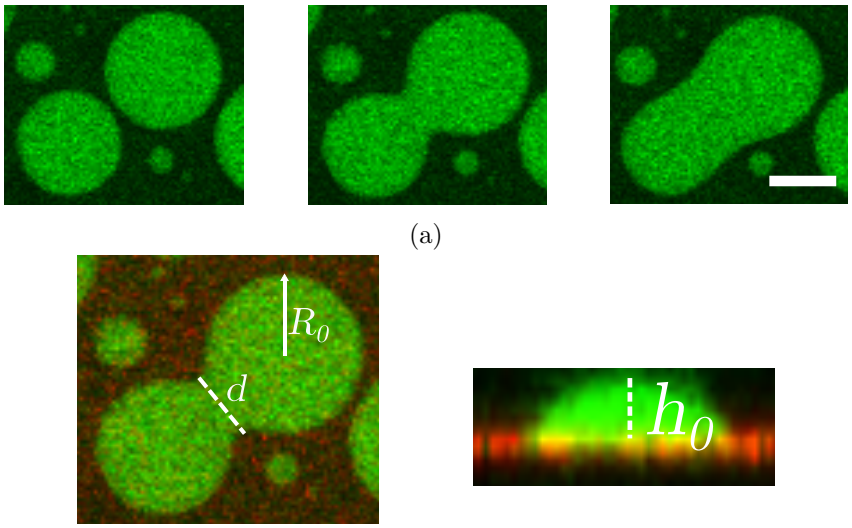


Figure 5.3: (a) Coalescence dynamics of tau protein droplets, scale bar: 10 µm, timestep: 1.10 s. Fluorescently labelled protein droplets appear in green, and the small red dots correspond to the fluorescent particles in the PDMS gel (b) Two coalescing protein droplets with a meniscus bridge width $d$, and initial radius $R_0$. (c) Side view of a tau protein droplet on the PDMS surface reconstructed by z-stack imaging of laser confocal microscopy. The height of the droplet is $h_0$.

A typical series of images of protein droplets coalescing on a PDMS substrate is presented in Figure 5.3 (a). When two protein droplets are close enough to each other, and with negligible initial velocities, they eventually merge into a bigger droplet [116]. A small liquid meniscus bridge (or neck) is then formed, as shown in the time series images, and grows rapidly over time under the influence of capillarity in this meniscus. The velocity at which the bridge widens

decreases over time, as the merged droplet increases in volume and becomes more circular [113].

In our experiments, the neck width $d$ and the initial radius $R_0$ of the droplets are measured by a visual analysis of the confocal images, as presented in Figure 5.3 (b). The initial radius of the droplet is obtained by averaging the radii of two merging droplets before their coalescence. By scanning the droplet along the z-axis with the confocal microscope, we are able to virtually reconstruct a side view of the drop, allowing us to determine the droplet height $h_0$ (see Figure 5.3 (c)). Although it is possible to obtain a z-stack image of a droplet while the time series acquisition is running, due to the low frame rate of the confocal microscope (about 0.9fps), we cannot track the height evolution of the two droplets during their coalescence. Instead, we acquire the z-stack images of the protein droplets at equilibrium, i.e. after their coalescence has ended. Assuming that the total volume of each protein droplet remains constant, we determine the height $h_0$ of tau protein droplet that has similar radius as $R_0$ of coalescing droplet.

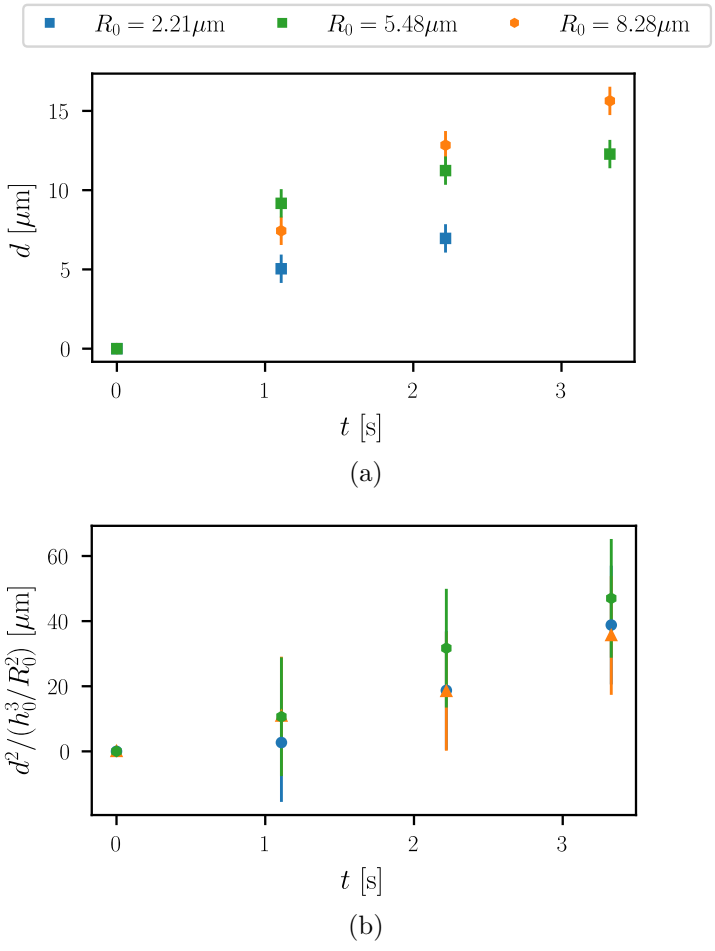


Figure 5.4: (a) Time evolution of the width $d$ of the liquid meniscus formed between two merging protein droplets. Different droplet sizes are presented. (b) Re-scaled width as a function of time for the same droplet sizes.

In Figure 5.4 (a), we present the time evolution of the meniscus bridge width $d$ of two coalescing droplets of similar radii, measured for different droplet sizes. For the sake of clarity, we only show the measurements for three different droplets radii here, ranging from the smallest

coalescing droplets observed to the largest ones. The full set of measurements for 16 different droplet radii can be found in appendix. droplet Due to the low frame rate of the confocal microscope and the relatively fast coalescence dynamics, our measurements are basically limited to four consecutive frames. The first frame ($t = 0$) corresponds to the frame before the meniscus bridge is observed and thus $d = 0$. As we can see, the radius $d$ increases with $t$, and starts to saturate at longer time. This implies that the growth rate of the bridge decreases over time for two coalescing protein droplets, just as observed for the pure liquids.

To unravel the time dependence of the liquid meniscus bridge width of coalescing tau protein droplets, one would naturally plot $d$ in a log-log scale. This would then allow us to easily identify the exponent associated to the power law followed by the meniscus bridge width.

However, due to the aforementioned limitations in temporal resolution, it appears very complicated to differentiate the two regimes as our data points barely span half a decade in $t$ properly. Therefore, we use a different approach which consists of scaling our data with the initial droplet radius $R_0$ and height $h_0$ instead. By plotting the scaled meniscus bridge width $d^2/(h_0^3/R_0^2)$ against time, according to the dependence presented in Equation 5.1, we obtain a nice collapse of the different data points within the error bar (see Figure 5.4 (b)). This implies that the tau protein droplets can be treated as viscous liquid droplets, and that their early stage coalescence dynamics is similar.

Using the above-mentioned Equation 5.1 and our measurements of the meniscus bridge width $d$, we can also estimate the capillary velocity $\gamma/\mu$ for each set of coalescing droplets. Indeed, knowing the height $h_0$ of the droplet, the capillary velocity can be calculated directly from the slope of the scaled width as a function of time presented in Figure 5.4 (b). We find that the capillary velocity of tau protein droplets is $\gamma/\mu = (8.90 \pm 3.77)\,\mu m/s$ (see Table 5.1), which is in a very good agreement with the value $8.33\,\mu m/s$ found in P granules proteins of *Caenorhabditis elegans* by Garfinkle, *et al.* [117].

## 5.4 Conclusion and outlook

In summary, we studied the liquid-liquid phase separation of tau protein droplets on a soft PDMS surface, and more specifically we investigated the coalescence of these droplets.

We show that tau protein droplets behave similarly to viscous liquid droplets and therefore that their coalescence dynamics can be described by using the same scaling law. For instance, we highlight the characteristic signature of this viscous regime by showing that the width of the liquid meniscus bridging two coalescing tau proteins droplets clearly depends on the drop radius. Furthermore, we show that our measurements can be used to indirectly estimate the capillary velocity $\gamma/\mu$, without the need of knowing any of these two quantities. For example, one could imagine a similar procedure using the extracted capillary velocity to estimate either the surface tension or the viscosity, knowing the other characteristics. Such approach could represent an interesting alternative to current techniques, not necessarily adapted to micron-sized droplets.

Initially, we expected to determine the surface tension of tau protein droplets by resolving the wetting ridge of the deformed soft PDMS surface underneath the droplet. However, we observed almost no deformation of our formulated soft gels, which implies that the surface tension of the tau proteins is then extremely small. Indeed, Brangwynne, *et al.* estimated the surface tension between the *C. elegans* protein found in P granules and the cytoplasm around 1 µN/m [103]. This is more than 4 orders of magnitude smaller than the interfacial tension between the buffer (which is mainly water) and a soft PDMS substrate ($\gamma = 42.4\,\mathrm{mN/m}$). Thus, the unbalance of these two interfacial tensions in vertical direction will lead to almost no deformation of the surface.

We can also realise the difficulty of inducing a surface deformation by estimating the corresponding elasto-capillary length of a soft PDMS substrate of elastic modulus $G_0 = 100\,\mathrm{Pa}$. We found that the elasto-capillary length is 10 nm, very small compared to the substrate thickness of 100 µm. Thus, the elasto-capillary length is too small to see any deformation (this is equivalent to the case of water droplet on a rigid glass surface).

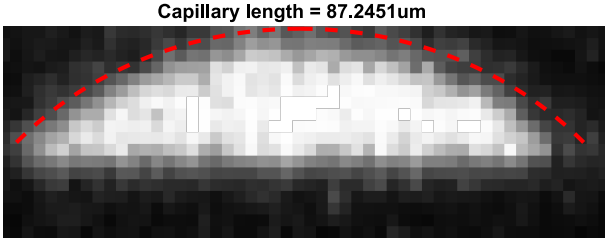


Figure 5.5: Capillary length of a tau protein droplet from the acquired experimental data. The capillary length was calculated from the droplet shape with a MATLAB code developed by Ijavi, *et al.* [118]. The red dashed line shows the detected profile of the droplet.

Ijavi, *et al.* measured the surface tension of protein and polymer droplets based on the analysis of the shape of an axisymmetric sessile droplet [118]. Figure 5.5 shows a reconstructed black-and-white z-stack image of one of our tau protein droplets. The MATLAB script developed by Ijavi, *et al.* is used to find the capillary length of the droplet. We obtain a capillary length of 87.2 µm.

In the beginning of the phase separation process, the protein droplets actually first sink onto the substrate plane before coalescing. By using a confocal microscopy to track droplets over time as they sink through an image plane, we can determine the sinking speed of droplets with different size. This will allow us to deduce the density contrast $\Delta\rho$ between the protein droplets and the buffer solution. The capillary length $l_c$ is given as:

$$l_c = \sqrt{\frac{\gamma}{\Delta\rho g}}, \tag{5.2}$$

where $\gamma$ the surface tension between the protein droplet and the buffer solution, $\Delta\rho$ the density difference between this interface, and $g$ the gravitational acceleration.

Knowing $\Delta\rho$ experimentally, we will deduce the interfacial tension between the protein droplets and the buffer solution. We can then find the viscosity of the protein droplet from the measured capillary velocity.

As presented in this chapter, soft PDMS surfaces can serve as a soft in-vitro model environment to study biological processes such as liquid-liquid phase separation. In the next chapter, we will introduce simple liquid systems with higher surface tension than the biological fluids wetting on a soft PDMS surface to address the recent debate in dynamical soft wetting.

## 5.5 Appendix

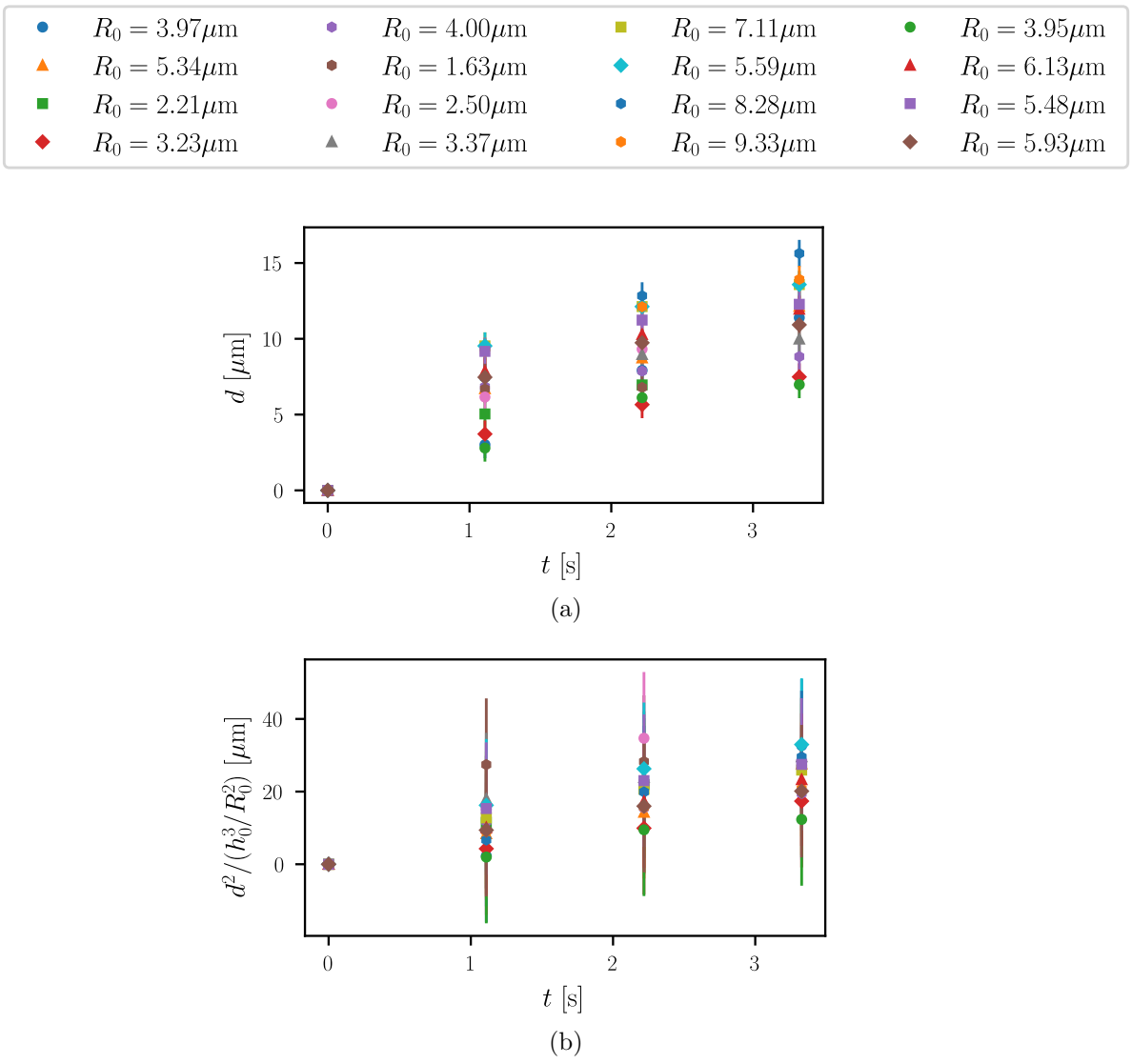


Figure 5.6: (a) Time evolution of the width $d$ of the liquid meniscus formed between two merging protein droplets. Different droplet sizes are presented. (b) Re-scaled width as a function of time for the same droplet sizes.

| Droplet | $R_0$[µm] | $h_0$[µm] | $\frac{\gamma}{\mu}$[µm/s] |
|---|---|---|---|
| 1 | 3.97 | 3.75 | 10.1 |
| 2 | 5.34 | 4.90 | 9.95 |
| 3 | 2.21 | 2.77 | 5.07 |
| 4 | 3.23 | 3.34 | 4.44 |
| 5 | 4.00 | 3.75 | 7.88 |
| 6 | 1.63 | 2.38 | 4.87 |
| 7 | 2.50 | 2.94 | 9.32 |
| 8 | 3.37 | 3.61 | 8.07 |
| 9 | 7.11 | 5.72 | 16.3 |
| 10 | 5.59 | 6.05 | 8.52 |
| 11 | 8.28 | 7.09 | 13.9 |
| 12 | 9.33 | 7.13 | 14.9 |
| 13 | 3.95 | 4.76 | 2.13 |
| 14 | 6.13 | 6.17 | 7.23 |
| 15 | 5.48 | 5.08 | 11.6 |
| 16 | 5.93 | 5.51 | 8.17 |

Table 5.1: Experimental measurements of the droplet dimensions $R_0$, $h_0$, and the extracted capillay velocity $\frac{\gamma}{\mu}$ of corresponding coalescing tau protein droplets

# Chapter 6

# Moving wetting ridges on ultra-soft gels

### Citation and credit

Submitted

### Title

Moving wetting ridges on ultra-soft gels

### Authors

Hansol Jeon, Youchuang Chao, and Stefan Karpitschka

## 6.1 Abstract

The surface mechanics of soft solids are important in many natural and technological applications. In this context, static and dynamic wetting of soft polymer gels has emerged as a versatile model system. Recent experimental observations have sparked controversial discussions of the underlying theoretical description, ranging from concentrated elastic forces over strain-dependent solid surface tensions, to poroelastic deformations or the capillary extraction of liquid components in the gel. Here we present measurements of the shapes of moving wetting ridges with high spatio-temporal resolution, combining different wetting phases (water, FC-70, air) on top of different ultra-soft PDMS gels ($\sim 100\,\mathrm{Pa}$). Comparing our experimental results to the asymptotic behavior of linear visco-elasto-capillary theory in the vicinity of the ridge, we separate reliable measurements from potential resolution artifacts. Remarkably, we find that the commonly used elastocapillary scaling fails to collapse the ridge shapes, but, for small normal forces, yields a viable prediction of the dynamic ridge angles. We demonstrate that neither of the debated theoretical models delivers a quantitative description, while the capillary extraction of an oil skirt appears to be most promising.

## 6.2 Introduction

Wetting of soft materials has recently become an intensely studied field of research [119], with rich dynamics [120, 121, 122, 123, 124, 125] and applications from biology [126] to soft electronics [127]. Reticulated polymer networks, typically swollen by a liquid fraction of the polymer itself [128, 124], are commonly used materials in applications and fundamental research. Typically, these materials are so soft that they can be deformed by the capillarity of their surfaces, i.e., a solid capillary pressure [129]. On long timescales, the liquid fraction in the gel can rearrange, leading to poroelastic relaxation and shape adaptation [124, 130]. On small scales, these materials thus behave similar to liquids, dominated by capillary effects. In contrast to liquids, on large scales, these materials behave like solids, resisting to permanent loads with a finite storage modulus [131, 132, 133]. This dual nature of these materials poses intriguing scientific questions, especially when it comes to their response to localized loads, in which the capillary and elastic behaviors both contribute.

It is commonly assumed that a three-phase contact line, formed by a liquid meniscus ending on the surface of a soft solid, provides a near-perfect line load, concentrated to molecular scales [134, 135, 119]. Due to its fundamental and practical relevance, this problem received enormous attention during the last decade [136, 119]. Pioneering work showed that the motion of contact lines on soft materials is limited by dissipation in the solid, not the liquid, which is called viscoelastic braking [134, 135]. The notion that the local force balance at the three-phase line is of capillary instead of elastic origin was experimentally verified in a series of seminal papers by Style et al. [137, 138]. Thus, it is believed that this force balance is equivalent to what is known as Neumann's balance for liquid three-phase lines [139].

A purely capillary force balance at a three-phase line is only possible if the three surface tensions fulfill a certain inequality, namely that none of the surface tensions is larger than the sum of the other two:

$$\gamma_i < \sum_{j \neq i} \gamma_j, \tag{6.1}$$

where the indices $i, j \in \{\mathrm{LA}, \mathrm{SL}, \mathrm{SA}\}$ indicate the interface between adjacent phases (liquid ("L"), ambient ("A"), and solid ("S")). Equivalently, the spreading parameter must be negative for any combination of the three phases. Most of the static and dynamic soft wetting experiments in the past have been conducted for materials where this balance is actually in question, i.e., water/air on cross-linked polydimethylsiloxane (PDMS): The liquid precursor in the soft solid, typically linear PDMS chains, would spread at the interface of the other two phases rather than forming a stable three-phase line. Still, well-defined angles have been observed experimentally at the three-phase line [137, 138, 140, 141]. Recently, a debate on the contributing forces has emerged, and various mechanisms that could alter the force balance have been proposed, both in static and dynamic situations, including strain-dependent solid surface tensions [142, 143, 144, 145, 146, 147, 148, 133], surface adaptation [149], concentrated line loads due to non-linear elastic bulk stresses [150, 151], geometric and non-linear rheological effects [152, 153], as well as extraction of free polymer chains from the gel [154, 128, 155, 156, 157].

Here we revisit this problem, starting with a liquid combination that actually does allow a

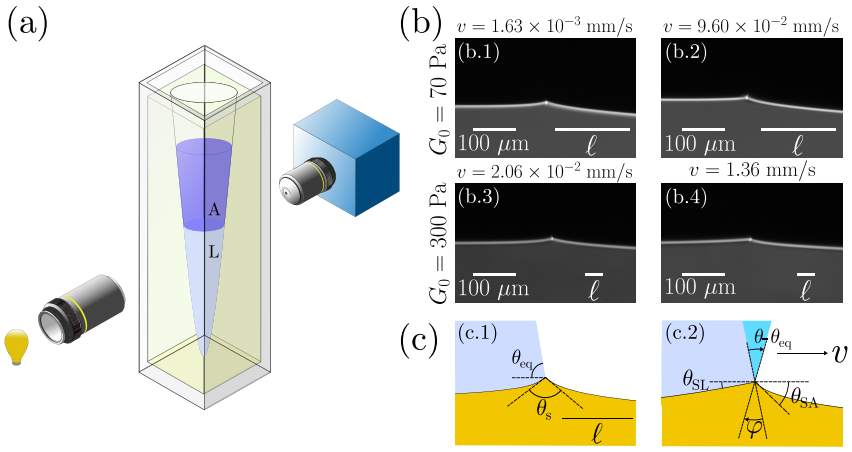


Figure 6.1: (a) A cuvette with a parabolic cavity is partially filled with two immiscible phases (bottom, 'L': FC-70 or water; top, 'A': water or air). The motion of the meniscus between the two phases and the solid wetting ridge is observed with a shadowgraphy setup. (b) Dynamic wetting ridges under an FC-70/air meniscus. Top: Wetting ridge of a 70 Pa gel traveling with $v = 1.63 \times 10^{-3}$mm/s (b.1), and $v = 9.60 \times 10^{-2}$mm/s (b.2). Bottom: Wetting ridge of a 300 Pa gel traveling with $v = 2.06 \times 10^{-2}$mm/s (b.3), and $v = 1.36$ mm/s (b.4). Right scale bars refer to $\ell$, the elastocapillary length of each PDMS gel. (c) Schematic representation of geometry of static (c.1) and moving (c.2) wetting ridges. $\theta_s$ is the opening angle of the ridge, and $\varphi$ indicates rotation of its bisector. $\theta_{eq}$ and $\theta$ are equilibrium and dynamic liquid contact angles, respectively.

stable force balance at the three-phase line, even when the liquid precursor to the soft solid, i.e., the un-crosslinked substrate material, is considered. In this case, the deformations also remain relatively small, and linear visco-elasto-capillary theory is expected to hold near quantitatively. We shadowgraphically visualize wetting ridges at high spatio-temporal resolution (Figure 6.1), for various substrate materials and wetting liquids, to test the existing scaling relations. With this approach, we show that neither of the former explanation attempts [143, 144, 145, 146, 147, 148, 133, 149, 150, 151, 154, 128, 155, 156, 157] delivers a consistent description of the observations.

## 6.3 Experimental

To obtain the shapes of wetting ridges at high spatio-temporal resolution, we performed shadowgraphy on cylindrical cavities inside blocks of transparent PDMS gels, analogous to previous studies [140, 141]. Briefly, the mixed liquid ingredients of the gel formulation are spun at high speed inside a standard optical cuvette while the gel cures. A bubble entrapped in the cuvette is elongated along the rotation axis due to centrifugal forces, forming a stable cylindrical cavity ($R \sim 2$ mm) when the gel is cured. The thickness of the gel layer between the cavity surface and the cuvette inner wall is $h_0 \sim 2$ mm. The surface of the cavity is observed through the gel in "grazing incidence", using a long-working distance microscope (Infinitube with Olympus Objective) and a high-speed camera (Phantom VEO 4K). The cavity is illuminated from behind to observe the shadow generated by refraction at the cavity surface (see Figure 6.1). In contrast to earlier experiments where a diffuse illumination was used, here we used a Köhler-type

collimated light source, focused into the imaging plane by a 5x Mitutoyo microscopy objective. Refraction of light at the cavity surface casts a shadow, while reflection of the collimated light at the gel surface creates a narrow bright line that enhances the visualization of the surface profile. We estimate the resolution of this imaging setup to $\sim 2\,\mu m$, but exclude any data closer than $\sim 4\,\mu m$ to the ridge tip from the analysis, to avoid picking up optical artifacts. Surface profiles are extracted from the shadowgraphs by first calculating the mean intensity gradient in gaussian-weighted neighborhoods (standard deviation $\sim 3$ px) and determining local maxima of the magnitude of the gradient along the direction of the gradient. Due to the apparent asymmetry of the wetting ridge, we fit each side of the contact line with a separate, empirical shape. For the left hand side (in contact with phase 'L', Figure 6.1 (b)), the profile is fitted with a third order polynomial function, $h(x) = a_1 + b_1 x + c_1 x^2 + d_1 x^3$. For the right hand side profile (in contact with phase 'A', Figure 6.1 (b)) we used $h(x) = a_2 + b_2 \log(c_2 + x)$. In addition to the ridge profile, we obtain an estimate of the dynamic liquid contact angle relative to the undeformed substrate, by monitoring the shadow of the liquid meniscus through the cavity. At the center of the cavity, distortion from the lensing effect of the cavity is minimal, and the meniscus position can be determined precisely. Since the capillary length and the ridge location are known, and the capillary number remains very small, the liquid angle at the ridge can be determined.

As gels, we used three different formulations. As a very soft gel, we used Dow Corning CY52-276, mixing components A and B in a mass ratio of 1.3:1, to obtain zero-frequency storage modulus $G_0 \sim 70\,Pa$. For slightly stiffer gels around 300 Pa, we used custom formulations, based on a vinyl-end-functionalized PDMS prepolymer (DMS-V31, Gelest) and two different methylhydrosiloxane-dimethylsiloxane copolymers (HMS-053 and HMS-082, Gelest) as cross-linker, and a platinum-complex catalyst (SIP6831.2, Gelest); The preparation procedure was analogous to Ref. [143]. We first prepared two stock mixtures, base and catalyst (component A), and base and cross-linker (component B), in proportions that the desired ratio of base polymer to cross-linker in the final gel formulation was achieved by mixing components A and B at a 1:1 mass ratio. A gel with $G_0 \sim 300\,Pa$ was obtained with 97.30 wt% of DMS-V31 and 2.70 wt% of HMS-053, estimating a stoichiometric ratio of vinyl to hydride groups of 3.8. Figure 6.2 shows the rheometric spectra of the two gels, where the viscoelastic rheology can be fitted by the Chasset-Thirion constitutional model, $\mu(\omega) = G'(\omega) + i\,G''(\omega) = G_0[1 + (i\,\omega\tau)^n]$, with zero-frequency storage modulus $G_0$, time scale $\tau$, and rheological exponent $n$ [135]. A third gel with $G_0 \sim 340\,Pa$ was obtained with 96.78 wt% of DMS-V31 and 3.22 wt% of HMS-082, estimating a stiochiometric ratio of vinyl to hydride groups of 2.1. This gel was intentionally prepared with a different cross-linker molecule and a different stoichiometric ratio of the functional groups, but a modulus comparable to the previous one. We repeated all experiments on the third gel, finding nearly identical profiles as for the 300 Pa gel. Thus in the following, we will focus exclusively on the 70 Pa and 300 Pa gels. All cavities were stored for a few days prior to use, to achieve stationary gel and surface states [158].

The wetting ridge is formed on the inside of the cavity by the meniscus of a liquid that fills the bottom half of the cavity, leaving the upper half exposed to ambient air. As liquids, we used a fluorinated oil, FC-70 (Sigma) and milli-Q water (resistivity 18.1 $M\Omega\,cm$). We also performed

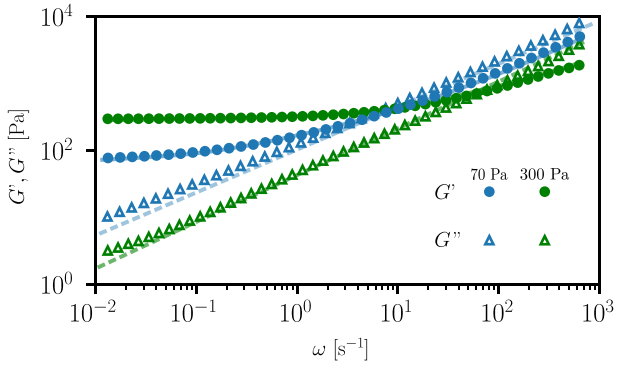


Figure 6.2: Rheometric spectra of the two main gels used (symbols), together with fits of the Chasset-Thirion constitutional model (lines). Blue: Dow-corning CY52-276 A/B, mixed 1.3:1 ($G_0 \sim 70\,\mathrm{Pa}$). Green: Gelest DMS-V31+HMS-053 ($G_0 \sim 300\,\mathrm{Pa}$); Closed symbols: $G'$; Open symbols: $G''$.

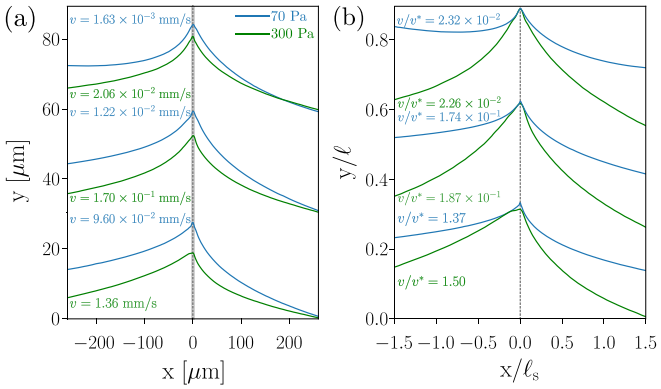


Figure 6.3: Wetting ridge profiles extracted from the shadowgraphic images. Blue curves: profiles of gel with $G_0 \sim 70\,\mathrm{Pa}$, green curves: profiles of gel with $G_0 \sim 300\,\mathrm{Pa}$. (a) Profiles in physical units. A vertical offset has been added to arrange the profiles conveniently.(b) Profiles scaled with $\ell$ in $y$, and $\ell_s$ in $x$.

experiments where the FC-70 meniscus was covered with milli-Q water, to obtain an additional set of solid and liquid surface tensions. For notational convenience, we use the index "L" to denote the liquid phase toward the bottom of the cavity, and "A" for the ambient, upper phase, which can be air or water (Figure 6.1a).

The motion of the meniscus was induced by injecting liquid into the bottom phase of the cavity, using a Nemesys syringe pump with a Hamilton gas tight syringe, connected to a needle that sticks through the liquid meniscus. Importantly, these syringe pumps generate virtually no stick-slip motion in their actuators [159], allowing for truly stationary motion of the menisci. All experiments were preformed at room temperature, $\sim (22 \pm 1)\,^\circ\mathrm{C}$.

## 6.4 Wetting Ridge Profiles

Figure 6.3 (a) shows the surface profiles of moving wetting ridges induced by an FC-70/air meniscus on two gels, with $G_0 \sim 70\,\mathrm{Pa}$ (blue) and $G_0 \sim 300\,\mathrm{Pa}$ (green), and for various velocities, increasing from top to bottom. The profiles have been shifted along the vertical axis for a

convenient arrangement. We define the elastocapillary length using the normal force that the liquid interface exerts at equilibrium, $\ell = \gamma \sin\theta_{\mathrm{eq}}/G_0$, where $\gamma$ is the liquid surface tension and $\theta_{\mathrm{eq}}$ is Young's angle, as a scale for the ridge height. These elastocapillary lengths are indicated as scale bars in Figure 6.3(a). According to linear theory [160], the horizontal length scale $\ell_{\mathrm{s}} = \Upsilon_{\mathrm{s}}/G_0$ involves the solid surface tension $\Upsilon_{\mathrm{s}}$, which is not known a priori, typically different on either side of the ridge, and may, in addition, depend on the surface strain. To obtain a suitable estimate for a mean $\ell_{\mathrm{s}}$, we extract the solid opening angle $\theta_{\mathrm{s}}$ (see Figure 6.1) from the profiles and calculate an effective $\Upsilon_{\mathrm{s}}$ from the vertical force balance, $2\Upsilon_{\mathrm{s}} \sin((\pi - \theta_{\mathrm{s}})/2) = \gamma \sin\theta_{\mathrm{eq}}$. The profiles, scaled with $\ell$ and $\ell_{\mathrm{s}}$ on vertical and horizontal axes, respectively, are shown in Figure 6.3(b), again shifted vertically to align the tips of the ridges. The physical contact line velocities of the displayed profiles have been chosen such that they become comparable when scaled with the characteristic velocity, $v^* = \Upsilon_{\mathrm{s}}/(G_0\tau)$ [160, 140]. Apparently, the profile shapes collapse near the ridge tip for dimensionless velocities $v/v^* < 1$. For dimensionless speeds $v/v^* > 1$, a small deviation near the tips can be seen. However, this deviation is in the range where optical artifacts due to the corner cannot safely be excluded anymore (see Figure 6.3b). Quite remarkable though, despite their collapse at small $|x|$, the scaled profiles deviate significantly already for $|x| \sim 0.2\ell_{\mathrm{s}}$. If the regular visco-elasto-capillary theory [135, 160] would apply, the scaled profiles should collapse up to $|x| \sim \ell_{\mathrm{s}}$.

A sharp fold at the surface of elastic half space, as induced by a contact line, exhibits a regular strain energy density but generates a logarithmic pressure singularity, both in finite strain and in linear theory [161, 162]. For a wetting ridge, the surfaces next to the fold are free and subject to solid capillarity. Thus, the pressure singularity manifests itself in a logarithmic divergence of the curvature of the solid surface, which has been shown in finite strain numerical simulations and experiments [162, 163]. Note that the slopes and thus the contact angles remain regular because the logarithmic singularity is integrable.

Now two questions arise: (i) can the ridge angles be determined faithfully from our experiments, i.e., do our experiments resolve scales on which the slopes have substantially converged to the angles at the three-phase line? (ii) does viscoelastic dissipation in moving wetting ridges generate some kind of singularity that might enter the force balance, or at least discredit the measured angles?

To address these questions, we first analyze the solid shape in the vicinity of the contact line in the framework of linear viscoelasticity, solving for the slope $h'(x)$ of a wetting ridge moving at velocity $v$. We scale $x$ by $\ell_{\mathrm{s}}$, $h'$ by $\ell$, and $v$ by $v^*$. The Fourier transform of the slope is readily obtained following [160]:

$$\widehat{h'}(q) = \frac{-i\,q}{\mu(v\,q)/\chi(q) + q^2}, \tag{6.2}$$

where $q$ is the wave number in units of $\ell_{\mathrm{s}}^{-1}$, and $\chi(q)$ is the Green's function for the geometry of the solid. The solution in real space $h'(x)$ is obtained by Fourier inversion of $\widehat{h'}(q)$. Here we are primarily interested in the properties of the solution near the tip of the ridge, well below the elastocapillary length, while the outer length, i.e. the wall thickness of the soft cavity, is much larger than $\ell_{\mathrm{s}}$. Thus, the elastic behavior can locally be approximated by an elastic half

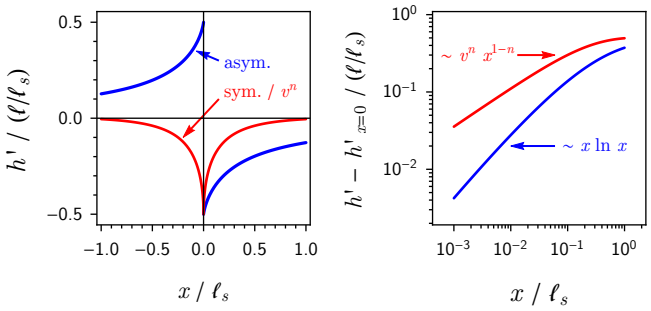


Figure 6.4: Asymptotic surface slopes of moving wetting ridges for small $x$ and $v$, with $n = 1/2$ (left: linear scale. right: double-logarithmic scale after subtracting the slope at $x = 0$). The asymmetric component (blue) corresponds to a static ridge and is independent of $v$ to leading order. The symmetric component (red) scales as $v^n$ and converges much slower to the limiting value at the contact line.

space, i.e. $\chi(q) \sim (2|q|)^{-1}$.

To analyze of the shape near the tip, we expand Equation (6.2) into real and imaginary parts, and those separately for small $v$:

$$\widehat{h'}(q) = \frac{-i\,q}{2|q| + q^2} - v^n \frac{|q|^n \,\sin\frac{n\,\pi}{2}}{2 + 2|q| + q^2/2} + \mathcal{O}(v^{n+1}). \tag{6.3}$$

Physically, the small-$v$ expansion corresponds to approximating the symmetric component of the ridge shape by the static solution because the leading-order consequence of dissipation is the emergence of an antisymmetric component in the shape, close to the tip. The imaginary part in Equation (6.3) resembles the static solution and carries a slope discontinuity at $x = 0$, encoded in the $\sim q^{-1}$ asymptote for large $q$. The real part introduces a symmetric component $\sim v^n$ to the slope due to viscoelastic dissipation.

Equation (6.3) can be inverted analytically to obtain a lengthy expression, plotted in Figure 6.4, which shows the following asymptotic behavior at small $x$:

$$\begin{aligned} h'(x) \sim \quad & - \quad \frac{\operatorname{sign} x}{2} - \frac{2x\,(\ln 2|x| + \gamma_\mathrm{E} - 1}{\pi} \\ & - \quad v^n \left( 2^{n-1} n \,\sec\frac{n\,\pi}{2} + \frac{2\Gamma(n-1)\sin^2\frac{n\,\pi}{2}}{\pi} |x|^{1-n} \right), \end{aligned} \tag{6.4}$$

where $\gamma_\mathrm{E} = 0.5772\ldots$ is Euler's constant. The first line of Equation (6.4) resembles the asymmetric component of the slope (blue lines in Figure 6.4a), which is identical to the static solution. Its slope discontinuity at $x = 0$ that represents the Neumann balance. Such sharp surface fold introduces a log-singular elastic stress in its vicinity which, by elastocapillarity, is translated into a log-singular surface curvature. The second line represents the symmetric component of the slope (red lines in Figure 6.4a), which is caused by dissipation and scales as $v^n$. The constant component corresponds to a rotation of the ridge tip, which had already been derived earlier [160]. In addition, one can identify an algebraic divergence of stress and curvature, $h'' \sim x^{-n}$. This singularity is also integrable across the contact line, does not generate a line force, and the Neumann angles remain well defined. Recent numerical simulations showed that the behavior of the viscoelastic stress is qualitatively maintained for finite strain viscoelasticity

when using an equivalent relaxation law [164].

Figure 6.4(b) shows the deviation of the dissipative (symmetric, red) and static (asymmetric,blue) slope components from their values at the contact line, scaling the symmetric component also with $v^n$, on logarithmic scales. The dissipative component of stress and thus surface curvature diverges much stronger than the elastic component, such that the corresponding components of the slope converges much slower to its value at the contact line. At a distance $\sim \ell_s/10$, the static component of the slopes deviates by $\sim 20\%$ from the value at the contact line ($h'(x = \pm 0, v = 0) = \mp 1/2$), while the corresponding deviation of the viscoelastic component remains much stronger unless the contact line speed is much smaller than the elastocapillary speed. Thus in both, experiments and simulations, resolutions well beyond $\sim \ell_s/10$ are required to correctly resolve the solid contact angles.

In order to estimate the actual surface slopes at the contact line and thus $\theta_{SL}$ and $\theta_{SA}$ (see Figure 6.1c) from the profiles shown in Figure 6.3, we use the asymptotic result of the linear theory to perform a reasonable extrapolation below our resolution limit, noting that finite strains might yield quantitatively different results. For the softer gel, the resolution limit is around $\ell_s/40$, for which a residual deviation is expected to be small. For the stiffer gel, however, we achieve only $\ell_s/10$, and non-linear effects, especially for the viscoelastic component, might still show significant deviations.

## 6.5 Quasi-Static Ridge Angles

Instead of measuring truly static ridges, we here extrapolate the solid angles of moving wetting ridges for $v \to 0$. This has two advantages: on the one hand, we avoid the ambiguity of a possible residual velocity, which can be as small as 1 nm/s; On the other hand, we avoid excessive poroelastic deformation, which occurs on long timescales, most noticeable for wetting ridges that have been residing at the same location for extended periods of time, although poroelastic relaxation will still be present [124, 165]. Extrapolating our measurements of $\theta_{SL}$ and $\theta_{SA}$ for $v \to 0$, we obtain $\theta_{SL} \sim \theta_{SA} \sim 17°$ for FC-70/air, independent (within the errors $\sim \pm 1°$) of the stiffness of the gel. These values match almost perfectly to those reported on static FC-70 droplets on PDMS in air, using confocal microscopy to localize surface-attached beads [137]. We also tested FC-70/water and water/air on all our gels. For FC-70/water, we obtain $\theta_{SL} \sim \theta_{SA} \sim 34°$, again independent of the gel stiffness. For water/air, we obtain $\theta_{SL} \sim \theta_{SA} \sim 50°$ for the 70 Pa gel, and $\theta_{SL} \sim \theta_{SA} \sim 45°$ for the 300 Pa gel. The angles of the last case are most likely suffering from a resolution problem, since the true non-linear stress might be quantitatively different from the linear model. Also, x-ray microscopy experiments yielded different values for this case [138]. Remarkably, however, we always find symmetric ridge tips, independent of the gel or the liquid combination.

Since cross-linking of PDMS leaves the molecular interactions of the PDMS chains largely unchanged, it is instructive to compare the observed angles to the Neumann angles against liquid PDMS. Employing a Neumann construction, using the surface tensions of the liquids against each other and the liquid PDMS base polymer (see table 6.1), one would expect $\theta_s = \pi - \theta_{SL} - \theta_{SA} \sim 115°$ for FC-70/air on PDMS. The validity of this Neumann construction is

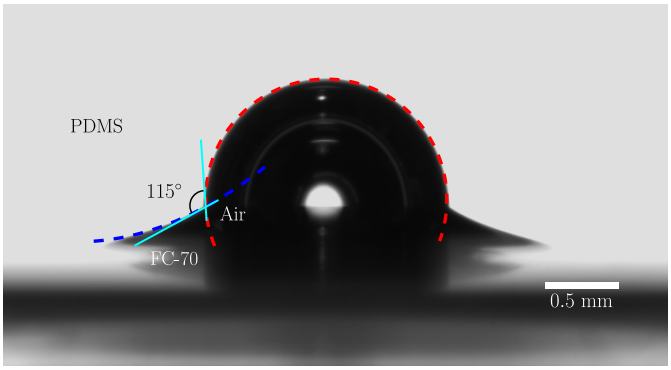


Figure 6.5: An air bubble trapped at the interface of liquid PDMS (top) and FC-70 (bottom). The Neumann angle in the PDMS phase is extracted from the drop (red dashed line) and meniscus (blue dashed line) contours.

confirmed in a direct measurement of the angle in the liquid PDMS phase $\sim 115°$, using an air bubble at the interface between bulk FC-70 and liquid PDMS (Figure 6.5). This value is significantly smaller than our measurement for wetting on cross-linked PDMS, which gives $\theta_s \sim 146°$ for FC-70/air on all cross-linked gels.

Since bulk elasticity does not generate line forces at sharp folds [161, 166, 162], the deviation must be caused by altered surface tensions or other, surface-bound phenomena. Several hypotheses have been proposed to explain this deviation in the Neumann angles between liquid and cross-linked PDMS: (i) the cross-linking reaction alters the surface tension [167], (ii) strain-dependent solid surface tension [143], and (iii) extraction of liquid PDMS precursor from the network into a wetting skirt that, in addition, may [154, 156] or may not [124, 155, 149] cloak the liquid-vapor surface and lower its effective tension.

For case (i), one would expect that the surface tension of cross-linked PDMS is different from liquid PDMS, but otherwise depends only on the liquid that it is contact with. In particular, it should not be affected by the strain at the ridge tip. This can be tested by using our three liquid or gas phases in different combinations. Each interface composition was tested twice, but with different Neumann angles because the exchange of the other phase yields a different liquid-air or liquid-liquid surface tension. Again calculating surface tensions from the Neumann balance, we obtain values that differ significantly (see table 6.2), well beyond any reasonable experimental error estimate, so we arrive at hypothesis (ii).

For case (ii), we may use the Neumann construction preformed above to estimate the solid surface stresses. For the case of FC-70/air on PDMS, the value we obtain matches well with

| | water | FC-70 | PDMS |
|---|---|---|---|
| air | 64 | 18.0 | 19.8 |
| water | | 50.6 | 42.4 |
| FC-70 | | | 6.7 |

Table 6.1: Surface tensions in mN/m of various liquids against each other. For PDMS, we measured the surface tensions of the non-cross-linked base polymer. For water/air, we consider a PDMS-cloaked interface [156]. Measurement errors are $\pm 0.5\,\mathrm{mN/m}$ except for water/air, which is estimated from Ref. [156] and varies $\sim \pm 1\,\mathrm{mN/m}$.

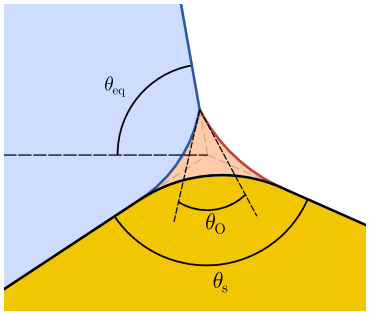


Figure 6.6: Extended Neumann construction in the presence of a liquid skirt (light red), presumably extracted from the soft gel (bottom, yellow). Contact angles between the oil and the gel are assumed to vanish. For cloaking of the liquid interface with oil, the Neumann angle $\theta_O$ would vanish.

previous reports [137]. Solid surface tension is assumed to depend primarily on the surface dilational strain, which can be estimated from the inclination of the surface: $\epsilon_s \sim \sqrt{1+(h')^2} - 1 \sim h'$. Thus, the surface strain should increase with decreasing $\theta_s$. However, from table 6.2, we notice that the surface tensions rather decrease with increasing strain. Note that the values on the last column, for water/air on PDMS ($\theta_s \sim 80°$) probably suffer from a large systematic error, underestimating $\theta_{SL}$ and $\theta_{SA}$. Park *et al.* reported $\Upsilon_{SL} \sim 16\,\mathrm{mN/m}$ and $\Upsilon_{SA} \sim 59\,\mathrm{mN/m}$, without taking into account cloaking [138]. Correcting their values for PDMS-cloaked water, we would obtain $\Upsilon_{SL} \sim 14\,\mathrm{mN/m}$ and $\Upsilon_{SA} \sim 52\,\mathrm{mN/m}$. Observing surface tensions that decrease with decreasing solid angle contradicts the assumption of a strain-dependent solid surface tension since measurements with externally stretched surfaces showed that surface stress increases with strain [143, 162].

In case (iii), the three-phase line is no longer located at the solid surface. Instead, an oil skirt [155, 157] with a negative laplace pressure $p_{skirt}$ transmits the normal force of the liquid-liquid or liquid-air interface, $\gamma \sin\theta$, onto the solid, distributed over a width $\ell_{skirt}$: $p_{skirt} = \gamma \sin\theta / \ell_{skirt}$. Figure 6.6 shows a sketch of this wetting configuration. The distributed pressure can straight-forwardly be implemented into linear visco-elastocapillary theory from [160] to estimate the surface slopes of the gel, using a normal traction (in physical units) $t_n = \gamma \sin\theta \cdot \Theta(\ell_{skirt}/2 - |x|)$, with $\Theta(x)$ the Heaviside theta function. The expression for the surface slopes, Equation (6.3), is then multiplied with the Fourier transform of the traction profile:

$$\widehat{h'}(q) = \frac{-i\,\frac{\ell_s}{\ell_{skirt}}\,\sin\frac{q\,\ell_{skirt}}{\ell_s}}{\mu(v\,q)/\chi(q) + q^2}, \tag{6.5}$$

| | $\theta_s \sim 146°$ | $\theta_s \sim 112°$ | $\theta_s \sim 80°$ |
|---|---|---|---|
| PDMS/air | 28.0 | | 21.5 |
| PDMS/water | | 53.6 | 56.7 |
| PDMS/FC-70 | 14.3 | 10.5 | |

Table 6.2: Surface stresses $\Upsilon_s$ in mN/m, obtained from the Neumann construction under various liquid combinations on top of cross-linked PDMS gels. typical uncertainties are $\pm 1\,\mathrm{mN/m}$, except for $\theta_s \sim 80°$, where a large systematic error cannot be ruled out.

The surface slopes are then calculated by numerical Fourier inversion. Given the small ridge surface slopes $\theta_{SL} \sim \theta_{SA} \sim 17°$ observed for FC-70/air on PDMS gels, this model should be near-quantitatively accurate. To obtain $\theta_s \sim 146°$, a skirt with $\ell_{skirt} \sim 0.86\ell_s$ is required, corresponding to 150 µm and 41 µm for the soft and the stiff gels, respectively. In the light of recent direct visualizations of oil skirts for static [155] and moving [157] contact lines on artificially swollen networks, this estimate appears unreasonably large.

Prior to extraction, the free oil phase in the PDMS gel has to be advected toward the contact line, which is indeed predicted by non-linear poroelasticity theory [168]. Since the refractive index of the oil and network are expected to be well-matched, poroelastic deformations remain 'invisible' in our experiments, i.e. showing up as bright as and thus indistinguishable from the gel, despite their significant size. Poroelastic swelling would further reduce the effective modulus of the gel at the tip. On the one hand, this would reduce the skirt size required to obtain the observed $\theta_s$. On the other hand, such enhanced swelling would show up in a deviation of the typical ridge shape.

This is indeed observed in Figure 6.3(b): The scaled profiles for different gel stiffnesses deviate significantly from each other for $|x| \gtrsim 0.2\ell_s$. The elastocapillary model would predict a good match between the profiles up to $|x| \sim \ell_s$ because the outer length, i.e. the gel thickness, is much larger than $\ell_s$ in both cases and does not impact the local shapes. Instead, we find a closer match between the shapes in physical units. Given that the surface tensions are identical for both cases, this indicates that the zero-frequency shear modulus $G_0$ is not a good scaling parameter here. Whether or not the observed ridge shapes can be described by, e.g., linear poroelasticity [165] remains to be evaluated.

## 6.6 Dynamic ridge angles

Figure 6.7 shows the rotation of the liquid interface, $\theta - \theta_{eq}$ (filled symbols), and of the ridge bisector, $\varphi$ (open symbols: experiments; red dashed line: linear visco-elasto-capillary theory), for FC-70/air on our softer ($\sim$ 70 Pa, blue) and stiffer ($\sim$ 300 Pa, blue) gels. The rotations have been scaled by the typical aspect ratio, i.e., $\ell/\ell_s$, and the velocity by the characteristic velocity $v^*$. For the 70 Pa gel (blue), we find a good agreement between the measured liquid and solid rotation, as well as the prediction from linear theory. Since the wetting ridges under FC-70/air menisci exhibit rather small surface slopes ($\theta_{SL} \sim \theta_{SA} \sim 17°$), one may expect that linear theory could deliver reasonable results here. For the 300 Pa gel (green), however, we find a deviation between the liquid rotation and the solid rotation, while the latter collapses onto the data from the soft gel and the model. Possibly, the velocity-dependent component of the ridge slopes has not been extracted with sufficient resolution, and thus the rotation is underestimated. The liquid angle does not suffer from such resolution limit since the capillary number remains very small and the meniscus shape is not expected to show significant deviations from its static shape. Thus, the dissipation generated by the 300 Pa gel appears to be increased relative to the 70 Pa gel or the theory. Finally, under the assumption of a poroelastic relaxation and/or an extracted oil skirt, the match between theory and the softer gel would be surprising. In this case, poroelastic dissipation or the dissipation in the skirt would have to be taken into account

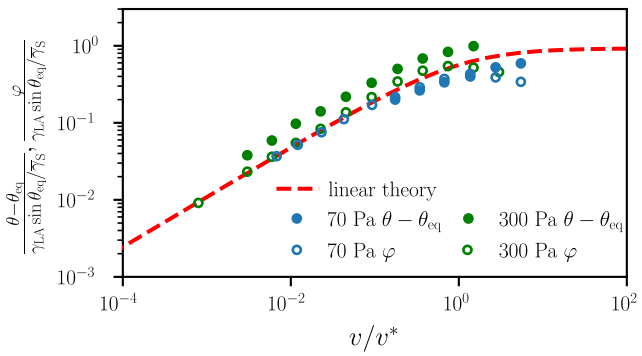


Figure 6.7: Rotation of liquid interface ($\theta - \theta_{eq}$, filled symbols) and the bisector of the wetting ridge ($\varphi$, open symbols), scaled by the aspect ratio $\ell/\ell_s = \gamma \sin\theta_{eq}/\Upsilon_s$ as a function of velocity scaled by the characteristic vico-elasto-capillary velocity $v^*$. The red dashed line shows the result of linear visco-elasto-capillary theory.

as well. If the loss modulus of the free oil phase was similar to the cross-linked gel, however, such a behavior could be rationalized.

Figure 6.8 shows the solid opening angle $\theta_s$ for all liquid combinations and the two gels, with velocity scaled by the elastocapillary velocity $v^*$. We notice that for small scaled velocities $v/v^*$, $\theta_s$ remains constant. For larger $v/v^*$, $\theta_s$ increases. The larger the liquid surface tension $\gamma$, i.e., the larger the normal traction and the smaller $\theta_s$, the earlier the detected $\theta_s$ increases with $v$, which points to a non-linear effect that is triggered by the surface strain. The curves for different gels, however, collapse perfectly, indicating that the time scale $\tau$ of the rheological model correctly describes the dynamics. Previously, the velocity-dependent increase of $\theta_s$ has been interpreted by a dynamical increase of the surface stresses, which yielded a quantitative explanation for the transition to stick-slip motion [140]. Given the asymptotic behavior of the slopes in the linear theory outlined above, resolution artifacts would, however, be expected to manifest in a similar way. Yet, then the stiffer gel should be more prone to these artifacts, and the collapse suggests this is not the case. Invoking again the hypothesis of poroelastic relaxation and/or extraction of an oil skirt by the contact line, and taking into account the non-collapse of the ridge profiles, the storage modulus in the ridge-tip region should be smaller than the independently measured $G_0$, and the length scales no longer depend on it. Further, the increase in $\theta_s$ can be reproduced in the linear model with a distributed traction. On the scale of the skirt, viscoelasticity significantly contributes to the force balance, and the increase of the moduli with frequency then leads to an increase of the solid angle.

## 6.7 Conclusion

We have shown that both the static, and the dynamic angles at the tip of a wetting ridge can not quantitatively be described by standard linear visco-elasto-capillary theory. The solid angle $\theta_s$ is typically much larger than expected from the Neumann balance for liquid PDMS. Neither linear, nor finite strain bulk elasticity can generate line forces at sharp surface folds [161, 162] that could contribute to the Neumann balance. It remains open though, whether a cusp-like singularity

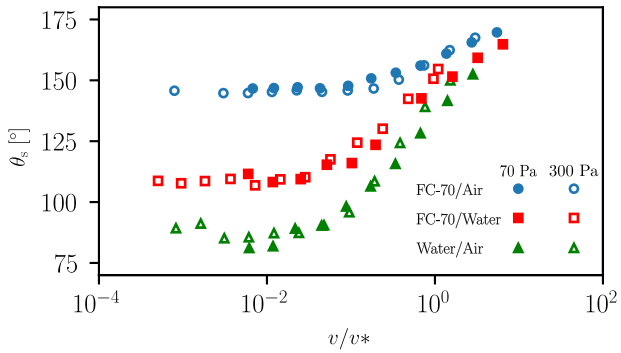


Figure 6.8: Solid opening angle $\theta_s$ as a function of velocity $v$, scaled by the elastocapillary velocity $v^* = \Upsilon_s/(G_0\tau)$. For small speeds, the angle remains constant, increasing only at larger speeds. Data for soft and stiff gels collapses in its scaling. Larger $\gamma$, i.e., smaller $\theta_s$, leads to an earlier increase of $\theta_s$.

of the profile, possibly combined with strain-stiffening constitutional laws, would generate a stronger stress singularity with a non-zero integral. For the case primarily studied here, FC-70/air on PDMS, such a singular profile is not expected. From the Neumann deconstruction of the ridge tip, we derived surface stresses that depend on $\theta_s$. We find that the stresses decrease with $\theta_s$, which seemingly contradicts measurements of the surface stress in response to an external strain [145, 143]. We also find that surface profiles on gels of different stiffness do not collapse, apart from a region very close ($|x| \lesssim 0.2\ell_s$) to the ridge tip, when scaled with the elastocapillary length. This indicates that the zero-frequency loss modulus is not a good parameter for the scaling behavior of the ridge profile. It rather motivates the existence of poroelastic relaxation [165] or an oil skirt [155, 157] extracted from the gel by the contact line.

Despite these discrepancies for the shapes and the static properties of wetting ridges, we find a rather good agreement between the measured rotation and the linear theory, at least for the soft gel where we can exclude significant experimental errors due to resolution-limitations. This points out that, should indeed poroelastic relaxation or an oil skirt be responsible for the observed shapes, and these regions should exhibit a similar elastocapillary velocity $v^*$ as the underlying gel. The measurement of the liquid angle indicates that the shadowgraphy misses a dissipative rotation of the ridge that is localized within the last $\sim 4\,\mu$m. This could be due to finite strain effects or high frequency components in the loss modulus that are not detected in oscillatory rheometry. Unfortunately, with our current experimental setup, higher spatio-temporal resolution is beyond reach. Phase contrast x-ray microscopy at a synchrotron facility [138, 169] could reveal the ridge properties at increased resolution, and possibly identify regions of excess dissipative stress.

## 6.8 Acknowledgments

We thank L. Hauer, D. Vollmer and R. Seemann for helpful discussions on oil skirt extraction, and M.H. Essink and J.H. Snoeijer on strain dependent surface tensions and finite strain viscoelasticity. S.K. and H.J. acknowledge funding from the German research foundation (DFG, Project No. KA4747/2-1). Y.C. acknowledges support through an Alexander von Humboldt

Fellowship.

# Chapter 7

# Conclusion

The research work carried out during this thesis was devoted to the wetting dynamics on soft surfaces. In this work, we formulated and utilised tailored PDMS samples of different stoichiometry with quantified rheological properties to:

1. serve as a soft in-vitro model environment with a stiffness comparable to brain tissues in order to study the phase separation of protein droplets.

2. investigate the dynamics of soft wetting, and address the ongoing debate of the field.

Brief summaries of the scientific results from Chapter 4, 5, and 6, and the possible outlooks for further research will be provided in the next sections.

## 7.1 Tailoring polydimethylsiloxane (PDMS) elastomers of different mechanical properties

### 7.1.1 Summary

In Chapter 4, we successfully formulated various PDMS networks by tuning the stoichiometric ratio of vinyl and silane functional groups. The rheometry of the prepared gels was conducted to quantify their mechanical properties.

We observed that the storage modulus $G_0$ of the network is larger (i.e more elastic) when its corresponding stoichiometric ratio is smaller (refer to Figure 7.1 (a)). Also, the network is stiffer when a base pre-polymer of higher molecular weight is used.

Through the swelling and extraction of PDMS samples, we concluded that the degree of swelling of the network decreases when the network is stiffer (high storage modulus $G_0$). The extraction ratio increases with an increase in the stoichiometric ratio until nA/nB reaches around 2, and starts to saturate (see Figure 7.1 (b)). This result shows that the extraction of free oligomers by using a large amount of solvent can not be used to determine the degree of cross-linking for soft PDMS gels. Also, the higher degree of swelling observed than the literature shows that the swelling ratio heavily depends on the stiffness of the PDMS network.

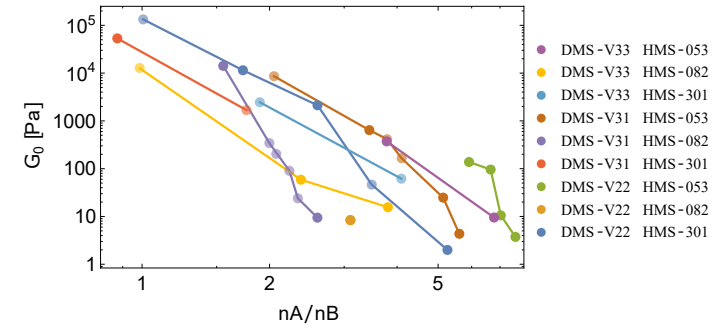


(a)

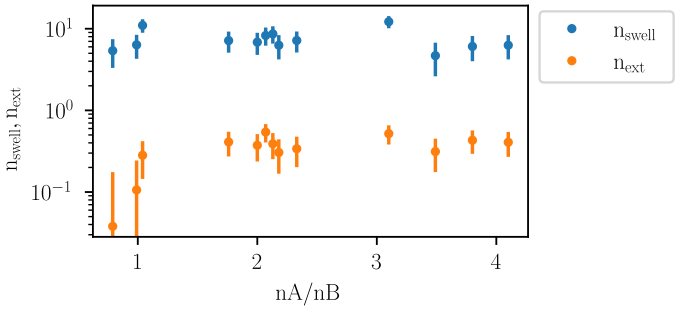


(b)

Figure 7.1: (a) Low frequency storage modulus ($G_0$) vs stoichiometric ratio nA/nB for each material combination. Data from Table 4.8 are represented as the transparent points. (b) $n_{swell}$, and $n_{ext}$ of PDMS samples against their corresponding stoichiometric ratio nA/nB in toluene

### 7.1.2 Outlook

Interfacial extraction methods, in which the PDMS gel is not confined in a small container, can be used to extract uncross-linked molecules in the soft PDMS networks to retain the original shape of our samples.

Recently, there has been a growing attention on bottlebrush polymers for soft wetting studies due to the various advantages over normal linear PDMS polymers. Bottlebrush polymers have relatively shorter side chains than normal PDMS elastomers, and have an entanglement molecular weight of $10^7$ g/mol, which is 3 orders of magnitude higher than that of linear PDMS polymers [170]. It has been found that bottlebrush polymer networks can also exhibit a low elastic modulus of around 100 Pa, that they are less adhesive and have smaller amount of uncross-linked molecules than the linear polymers[170]. Bottlebrush polymer networks consist of four precursors (instead of two like the linear chain PDMS polymers): base, cross-linker, side chain, and extension chain where each precursors contain either vinyl or silane functional groups. The rheological properties of such bottlebrush polymers with different stoichiometric ratio could be studied.

## 7.2 Liquid-liquid phase separation of tau protein droplets on a soft PDMS surface

### 7.2.1 Summary

In Chapter 5, we used one of our formulated PDMS gels to study the liquid-liquid phase separation of tau protein droplets on a soft surface. More specifically we investigated the coalescence dynamics of these droplets, as presented in Figure 7.2 (a).

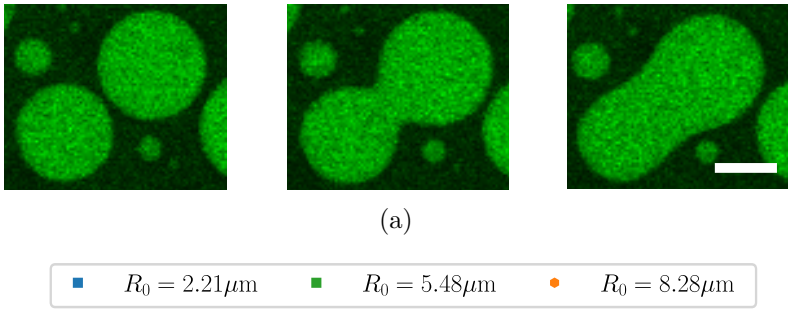

(a)

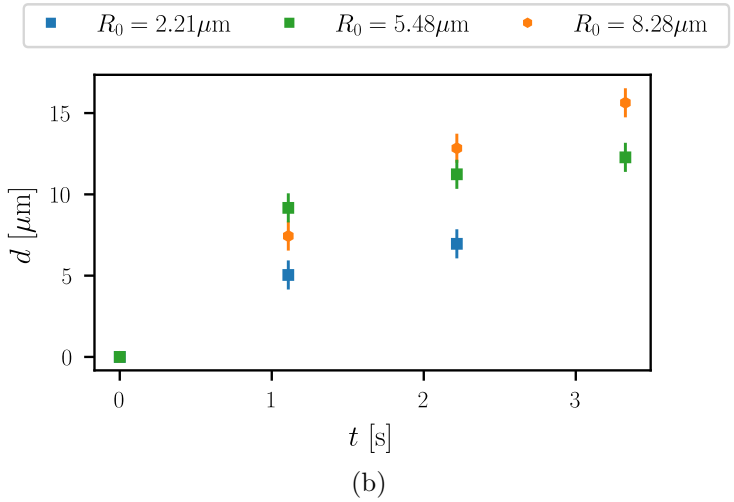


(b)

Figure 7.2: (a) Coalescence dynamics of tau protein droplets on a soft PDMS surface ($G_0$ = 113 Pa). Scale bar: 10 µm. Timestep: 1.10 s. Fluorescently labelled protein droplets appear in green, and the small red dots correspond to the fluorescent particles in the PDMS gel. (b) Time evolution of the width $d$ of the liquid meniscus formed between two merging protein droplets. Different droplet sizes are presented.

By investigating the time evolution of the liquid meniscus bridge width for different coalescence events (see Figure 7.2 (b)), we found that tau protein droplets behave similarly to viscous liquid droplets. Indeed, we retrieved the characteristic coalescence dynamics of viscous droplets, as well as the associated droplet radius dependence. Furthermore, our measurements were used to indirectly estimate the capillary velocity $\gamma/\mu$, without the need of knowing the surface tension nor the viscosity of these tau droplets.

Surprisingly, we did not observe any deformation of the soft PDMS network by the tau protein droplets. As the PDMS surface itself is very soft and deformable ($G_0$ = 113 Pa), this indicates that the interfacial tension between the protein droplets and the buffer solution is too small compared the interfacial tension between the buffer and PDMS to induce a visible wetting

ridge on the PDMS surface.

### 7.2.2 Outlook

In order to be able to directly observe a deformation of the surface, the elasto-capillary length needs to be comparable to the substrate thickness. As presented in Chapter 2, the elasto-capillary length depends on both the substrate stiffness and the surface tension (here between a tau protein droplet and the buffer solution) as $\ell \sim \gamma/G_0$. Thus we can think of tuning $\ell$ to increase the amplitude of the surface deformation. We could try to increase the elasto-capillary length by using an even softer PDMS substrate. However, this will no longer satisfy our main objective of using a gel with comparable stiffness as the brain tissues. Also, the softest gel that we have formulated so far has a stiffness of $G_0 \approx 4\,\mathrm{Pa}$. Assuming that the protein-buffer surface tension is $\gamma \sim 1\,\mu\mathrm{N/m}$ [103], the corresponding elasto-capillary length is then $\ell \sim 0.25\,\mu\mathrm{m}$, which is still far smaller than the thickness of the substrate ($100\,\mu\mathrm{m}$). Therefore the deformation will not be observed.

Instead, we could tune the interfacial tension between the PDMS substrate and the buffer solution. As the interfacial tension between a protein droplet and the buffer is very small, the buffer-PDMS interfacial tension has to be small enough to induce a deformation on the surface. The surrounding liquid (mostly water) could be replaced by another one with a smaller surface tension, but it would not model as accurately the human cytoplasm that usually consists of water.

The capillary length of a sessile protein droplet can be used to extract the surface tension and viscosity of the tau protein droplets. We have already obtained the capillary length ($l_c = 87.2\,\mu\mathrm{m}$) of a droplet based on the image analysis of its contour as done by Ijavi, *et al.* [118]. By determining the sinking speed of the droplets as a function of the droplet size, we could measure the density contrast $\Delta\rho$ between the protein droplet and the buffer solution. The protein-buffer interfacial tension will then be extracted, and the viscosity will be deduced from the already resolved capillary velocity.

## 7.3 Moving wetting ridges on soft gels

### 7.3.1 Summary

In Chapter 6, we showed that both static and dynamic angles at the tip of a wetting ridge cannot be described by linear viscoelastic capillary theory. Also, the obtained opening angle of the solid ridge $\theta_S$ was much larger than what we would expect from the Neumann balance by using the surface tension of liquid (uncured) PDMS silicone oil.

We derived surface stresses that depend on the ridge opening angle via the Neumann deconstruction of the ridge tip. Contradicting the literature [43, 52], we observed a decrease in surface stress with an increase in surface strain.

The deviation of the gel surface profiles of different stiffness (see Figure 7.3 (a))apart from a region very close to the tip indicates that there exists an oil skirt extracted by the contact line.

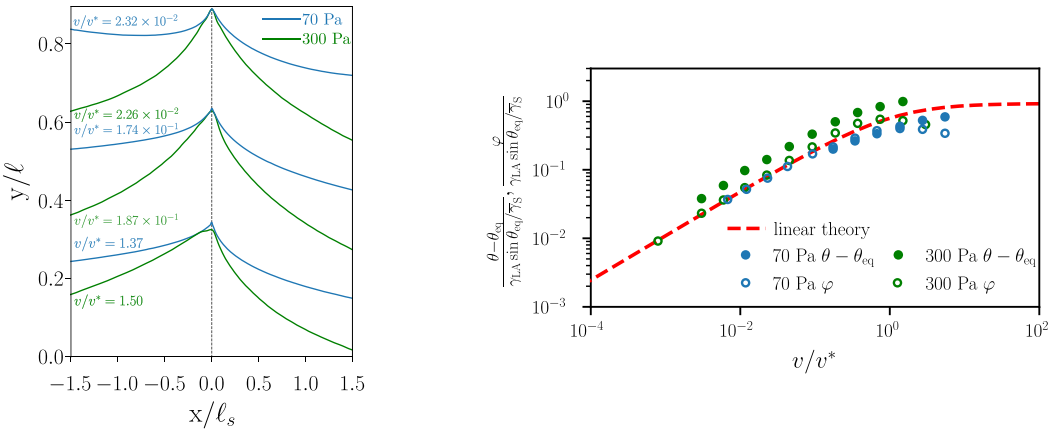


(a) (b)

Figure 7.3: (a) Wetting ridge profiles extracted from the shadowgraphic images. Blue curves: profiles of gel with $G_0 = 70\,\text{Pa}$, green curves: profiles of gel with $G_0 = 300\,\text{Pa}$. Profiles are scaled with $\ell$ in $y$, and $\ell_s$ in $x$. (b) Rotation of liquid interface ($\theta - \theta_{eq}$, filled symbols) and the bisector of the wetting ridge ($\varphi$, open symbols), scaled by the aspect ratio $\ell/\ell_s = \gamma_{LA} \sin\theta_{eq}/\gamma_s$ as a function of velocity scaled by the characteristic vico-elasto-capillary velocity $v^* = \gamma_s/(G_0\tau)$. The red dashed line shows the result of linear visco-elasto-capillary theory.

As shown in Figure 7.3 (b), we observed a good agreement between the measured ridge roatation and the linear theory for the soft gel with a larger elasto-capillary length where we can exclude experimental errors due to the resolution limit. This agreement shows that the oil skirt exhibit a similar loss modulus as the underlying gel.

The measurement of the dynamic liquid contact angle shows that the shadowgraphy does not capture a dissipative rotation of the ridge that is localised within the last $\sim 4\,\mu\text{m}$. This could be due to finite strain effects or high frequency components in the loss modulus that are not detected in oscillatory rheology. Higher spatio-temporal resoultion with our shadowgraphy set up will not be possible.

### 7.3.2 Outlook

A phase contrast x-ray microscopy can be used to obtain a higher resolution experimental data of the wetting ridge. This will hopefully identify regions of excess dissipative stress.

Also, we can study the impact of an oil skirt extracted by the contact line experimentally. Swelling of a polymer gel by a lower molecular weight silicone oil can induce an oil skirt as observed by Cai, *et al.* [49, 50]. We can investigate how does the existence of such phase separated oil skirt can affect the dynamics of the wetting ridge.

# Bibliography


[1] Dongliang Tian, Yanlin Song, and Lei Jiang. "Patterning of controllable surface wettability for printing techniques". *Chemical society reviews* 42.12 (2013), pp. 5184–5209.

[2] Edward J Swift et al. "Dentin/enamel adhesives: review of the literature". *Pediatric dentistry* 24.5 (2002), pp. 456–461.

[3] Richard James Archer et al. "Recent progress and future directions of multifunctional (super) wetting smooth/structured surfaces and coatings". *Advanced Functional Materials* 30.26 (2020), p. 1907772.

[4] Sera Shin et al. "Bio-inspired extreme wetting surfaces for biomedical applications". *Materials* 9.2 (2016), p. 116.

[5] Kock-Yee Law and Hong Zhao. *Surface wetting: characterization, contact angle, and fundamentals*. Springer International Publishing Basel, Switzerland, 2016.

[6] Gui Lu, Xiao-Dong Wang, and Yuan-Yuan Duan. "A critical review of dynamic wetting by complex fluids: from Newtonian fluids to non-Newtonian fluids and nanofluids". *Advances in colloid and interface science* 236 (2016), pp. 43–62.

[7] GR Lester. "Contact angles of liquids at deformable solid surfaces". *Journal of Colloid Science* 16.4 (1961), pp. 315–326.

[8] BV Deryagin, VM Starov, and NV Churaev. "Pressure on a wetting perimeter". *Colloid Journal of the USSR* 44.5 (1982), pp. 770–775.

[9] Martin ER Shanahan. "The spreading dynamics of a liquid drop on a viscoelastic solid". *Journal of Physics D: Applied Physics* 21.6 (1988), p. 981.

[10] Robert W Style et al. "Universal deformation of soft substrates near a contact line and the direct measurement of solid surface stresses". *Physical review letters* 110.6 (2013), p. 066103.

[11] Su Ji Park et al. "Visualization of asymmetric wetting ridges on soft solids with X-ray microscopy". *Nature communications* 5.1 (2014), pp. 1–7.

[12] Pierre-Gilles De Gennes. "Wetting: statics and dynamics". *Reviews of modern physics* 57.3 (1985), p. 827.

[13] M Amaral Fortes. “Microscopic and macroscopic contact angles”. *Journal of the Chemical Society, Faraday Transactions 1: Physical Chemistry in Condensed Phases* 78.1 (1982), pp. 101–107.

[14] Kock-Yee Law. *Definitions for hydrophilicity, hydrophobicity, and superhydrophobicity: getting the basics right*. 2014.

[15] Uwe Thiele et al. “Sliding drops on an inclined plane”. *Colloids and Surfaces A: Physicochemical and Engineering Aspects* 206.1-3 (2002), pp. 87–104.

[16] James C Bird, Shreyas Mandre, and Howard A Stone. “Short-time dynamics of partial wetting”. *Physical review letters* 100.23 (2008), p. 234501.

[17] EB Dussan. “On the spreading of liquids on solid surfaces: static and dynamic contact lines”. *Annual Review of Fluid Mechanics* 11.1 (1979), pp. 371–400.

[18] Daniel Bonn et al. “Wetting and spreading”. *Reviews of modern physics* 81.2 (2009), p. 739.

[19] Jing-Den Chen. “Experiments on a spreading drop and its contact angle on a solid”. *Journal of colloid and interface science* 122.1 (1988), pp. 60–72.

[20] PG de Gennes. “F. rochard-Wyart, and D. Quere”. *Capillarity and Wetting Phenomena: Drops, Bubbles, Pearls, Waves* (2003).

[21] LH Tanner. “The spreading of silicone oil drops on horizontal surfaces”. *Journal of Physics D: Applied Physics* 12.9 (1979), p. 1473.

[22] OV Voinov. “Hydrodynamics of wetting”. *Fluid dynamics* 11.5 (1976), pp. 714–721.

[23] AM Cazabat and MA Cohen Stuart. “Dynamics of wetting: effects of surface roughness”. *The Journal of Physical Chemistry* 90.22 (1986), pp. 5845–5849.

[24] Chun Huh and Laurence E Scriven. “Hydrodynamic model of steady movement of a solid/liquid/fluid contact line”. *Journal of colloid and interface science* 35.1 (1971), pp. 85–101.

[25] Jacco H Snoeijer and Bruno Andreotti. “Moving contact lines: scales, regimes, and dynamical transitions”. *Annual review of fluid mechanics* 45.1 (2013), pp. 269–292.

[26] Julian Vincent. “Chapter One. Basic Elasticity and Viscoelasticity”. In: *Structural biomaterials*. Princeton University Press, 2012, pp. 1–28.

[27] Stefan Karpitschka et al. “Droplets move over viscoelastic substrates by surfing a ridge”. *Nature communications* 6.1 (2015), pp. 1–7.

[28] Serge Mora et al. “Capillarity driven instability of a soft solid”. *Physical review letters* 105.21 (2010), p. 214301.

[29] Alain Carré, Jean-Claude Gastel, and Martin ER Shanahan. “Viscoelastic effects in the spreading of liquids”. *Nature* 379.6564 (1996), pp. 432–434.

[30] MER Shanahan and PG De Gennes. "Equilibrium of the triple line solid/liquid/fluid of a sessile drop". In: *Adhesion 11*. Springer, 1987, pp. 71–81.

[31] Franz Ernst Neumann and Albert Wangerin. *Vorlesung über die Theorie der Capillarität*. BG Teubner, 1894.

[32] Anne-Laure Biance, Christophe Clanet, and David Quéré. "First steps in the spreading of a liquid droplet". *Physical Review E* 69.1 (2004), p. 016301.

[33] Alain Carré and Martin ER Shanahan. "Viscoelastic braking of a running drop". *Langmuir* 17.10 (2001), pp. 2982–2985.

[34] Piotr Mazurek, Sindhu Vudayagiri, and Anne Ladegaard Skov. "How to tailor flexible silicone elastomers with mechanical integrity: a tutorial review". *Chemical Society Reviews* 48.6 (2019), pp. 1448–1464.

[35] Keil J Regehr et al. "Biological implications of polydimethylsiloxane-based microfluidic cell culture". *Lab on a Chip* 9.15 (2009), pp. 2132–2139.

[36] Johannes Karl Fink. *High performance polymers*. William Andrew, 2014.

[37] D Nichetti and I Manas-Zloczower. "Viscosity model for polydisperse polymer melts". *Journal of rheology* 42.4 (1998), pp. 951–969.

[38] Sergei S Sheiko and Andrey V Dobrynin. "Architectural code for rubber elasticity: From supersoft to superfirm materials". *Macromolecules* 52.20 (2019), pp. 7531–7546.

[39] JS Rowlinson and B Widom. *Molecular Theory o [Capillarity (Oxford University Press)*. 1982.

[40] Antonin Marchand et al. "Capillary pressure and contact line force on a soft solid". *Physical review letters* 108.9 (2012), p. 094301.

[41] Bruno Andreotti and Jacco H Snoeijer. "Statics and dynamics of soft wetting". *Annual review of fluid mechanics* 52 (2020), pp. 285–308.

[42] Bruno Andreotti and Jacco H Snoeijer. "Soft wetting and the Shuttleworth effect, at the crossroads between thermodynamics and mechanics". *EPL (Europhysics Letters)* 113.6 (2016), p. 66001.

[43] Ro Shuttleworth. "The surface tension of solids". *Proceedings of the physical society. Section A* 63.5 (1950), p. 444.

[44] Mees M Flapper et al. "Reversal of Solvent Migration in Poroelastic Folds". *arXiv preprint arXiv:2209.00887* (2022).

[45] Maurice A Biot. "General theory of three-dimensional consolidation". *Journal of applied physics* 12.2 (1941), pp. 155–164.

[46] Menghua Zhao et al. "Growth and relaxation of a ridge on a soft poroelastic substrate". *Soft matter* 14.1 (2018), pp. 61–72.

[47] Qin Xu et al. “Viscoelastic and poroelastic relaxations of soft solid surfaces”. *Physical Review Letters* 125.23 (2020), p. 238002.

[48] Aurélie Hourlier-Fargette et al. “Role of uncrosslinked chains in droplets dynamics on silicone elastomers”. *Soft Matter* 13.19 (2017), pp. 3484–3491.

[49] Zhuoyun Cai et al. “Fluid separation and network deformation in wetting of soft and swollen surfaces”. *Communications Materials* 2.1 (2021), pp. 1–11.

[50] Lukas Hauer et al. “Phase Separation in Wetting Ridges of Sliding Drops on Soft and Swollen Surfaces”. *arXiv preprint arXiv:2208.11177* (2022).

[51] Rafael D Schulman et al. “Surface energy of strained amorphous solids”. *Nature communications* 9.1 (2018), pp. 1–6.

[52] Qin Xu et al. “Direct measurement of strain-dependent solid surface stress”. *Nature communications* 8.1 (2017), pp. 1–6.

[53] Julien Dervaux, Matthieu Roché, and Laurent Limat. “Nonlinear theory of wetting on deformable substrates”. *Soft Matter* 16.22 (2020), pp. 5157–5176.

[54] M Van Gorcum et al. “Spreading on viscoelastic solids: are contact angles selected by Neumann’s law?” *Soft Matter* 16.5 (2020), pp. 1306–1322.

[55] Luuk A Lubbers et al. “Drops on soft solids: free energy and double transition of contact angles”. *Journal of fluid mechanics* 747 (2014).

[56] Katharine E Jensen et al. “Wetting and phase separation in soft adhesion”. *Proceedings of the National Academy of Sciences* 112.47 (2015), pp. 14490–14494.

[57] Jessamine Ng Lee, Cheolmin Park, and George M Whitesides. “Solvent compatibility of poly (dimethylsiloxane)-based microfluidic devices”. *Analytical chemistry* 75.23 (2003), pp. 6544–6554.

[58] John Burke. “Solubility Parameters: Theory and Application” (1984).

[59] *Solubility parameters: Theory and application*. URL: https://cool.culturalheritage.org/coolaic/sg/bpg/annual/v03/bp03-04.html.

[60] Charles M Hansen. *The three dimensional solubility parameter and solvent diffusion coefficient: Their importance in surface coating formulation*. 1967.

[61] Johannes Fink. *Petroleum engineer’s guide to oil field chemicals and fluids*. Gulf Professional Publishing, 2021.

[62] URL: https://www.toppr.com/guides/chemistry/atoms-and-molecules/dipole-moment/.

[63] Paul J Flory. *Principles of polymer chemistry*. Cornell university press, 1953.

[64] Stephen D Bruck. "Fiber Structure-Property Relationships: A Disulfide-Crosslinked Self-Crimping Polyamide". *Journal of Research of the National Bureau of Standards. Section A, Physics and Chemistry* 65.6 (1961), p. 489.

[65] Arturo Horta and M Alejandra Pastoriza. "The interaction parameter of crosslinked networks and star polymers". *European polymer journal* 41.12 (2005), pp. 2793–2802.

[66] N Stafie, DF Stamatialis, and Matthias Wessling. "Effect of PDMS cross-linking degree on the permeation performance of PAN/PDMS composite nanofiltration membranes". *Separation and purification technology* 45.3 (2005), pp. 220–231.

[67] Leslie H Sperling. *Introduction to physical polymer science*. John Wiley & Sons, 2005.

[68] Mark Alger. *Polymer science dictionary*. Springer Science & Business Media, 1996.

[69] Robert W Style et al. "Surface tension and contact with soft elastic solids". *Nature communications* 4.1 (2013), pp. 1–6.

[70] R Eisenschitz and W Philippoff. "Eine neue Methode zur Bestimmung mechanischer Materialkonstanten von Kolloiden". *Naturwissenschaften* 21.28 (1933), pp. 527–528.

[71] *Introduction to confocal microscopy*. URL: https://www.olympus-lifescience.com/en/microscope-resource/primer/techniques/confocal/confocalintro/.

[72] Juan Carlos Stockert and Alfonso Blázquez-Castro. *Fluorescence microscopy in life sciences*. Bentham Science Publishers, 2017.

[73] *Confocal microscopy*. URL: https://www.microscopyu.com/techniques/confocal.

[74] Shihe Xu et al. "Degradation of polydimethylsiloxanes (silicones) as influenced by clay minerals". *Environmental science & technology* 32.9 (1998), pp. 1199–1206.

[75] Asma Sharfeddin et al. "Comparison of the macroscale and microscale tests for measuring elastic properties of polydimethylsiloxane". *Journal of Applied Polymer Science* 132.42 (2015).

[76] Daniel R Darby et al. "Modulus and adhesion of Sylgard 184, Solaris, and Ecoflex 00-30 silicone elastomers with varied mixing ratios". *Journal of Applied Polymer Science* 139.25 (2022), e52412.

[77] Brian D Mather et al. "Michael addition reactions in macromolecular design for emerging technologies". *Progress in Polymer Science* 31.5 (2006), pp. 487–531.

[78] Andrew B Lowe. "Thiol-ene "click" reactions and recent applications in polymer and materials synthesis". *Polymer Chemistry* 1.1 (2010), pp. 17–36.

[79] Andrew B Lowe. "Thiol–ene "click" reactions and recent applications in polymer and materials synthesis: a first update". *Polymer Chemistry* 5.17 (2014), pp. 4820–4870.

[80] Gurkan Hizal, Umit Tunca, and Amitav Sanyal. "Discrete macromolecular constructs via the Diels–Alder "Click" reaction". *Journal of Polymer Science Part A: Polymer Chemistry* 49.19 (2011), pp. 4103–4120.

[81] Nuttapol Risangud et al. "Hydrosilylation as an efficient tool for polymer synthesis and modification with methacrylates". *RSC advances* 5.8 (2015), pp. 5879–5885.

[82] Stephen J Clarson and J Anthony Semlyen. *Siloxane polymers*. Prentice Hall, 1993.

[83] François Ganachaud, Sylvie Boileau, Bruno Boury, et al. *Silicon based polymers*. Springer, 2008.

[84] Zhixin Wang, Alex A Volinsky, and Nathan D Gallant. "Crosslinking effect on polydimethylsiloxane elastic modulus measured by custom-built compression instrument". *Journal of Applied Polymer Science* 131.22 (2014).

[85] Piotr P Matloka et al. "Chain-End and Chain-Internal Crosslinking in "Latent Reactive" Silicon Elastomers". *Macromolecular Chemistry and Physics* 206.2 (2005), pp. 218–226.

[86] Hans Claesson et al. "Semi-crystalline thermoset resins: tailoring rheological properties in melt using comb structures with crystalline grafts". *Progress in organic coatings* 49.1 (2004), pp. 13–22.

[87] Mohammad Vatankhah-Varnoosfaderani et al. "Bottlebrush elastomers: A new platform for freestanding electroactuation". *Advanced Materials* 29.2 (2017), p. 1604209.

[88] Sundar K Venkataraman et al. "Critical extent of reaction of a polydimethylsiloxane polymer network". *Polymer* 30.12 (1989), pp. 2222–2226.

[89] Justin D Glover et al. "Extracting uncrosslinked material from low modulus sylgard 184 and the effect on mechanical properties". *Journal of Polymer Science* 58.2 (2020), pp. 343–351.

[90] Suman K Patel et al. "Elastic modulus and equilibrium swelling of poly (dimethylsiloxane) networks". *Macromolecules* 25.20 (1992), pp. 5241–5251.

[91] Maura Cesaria et al. "PDMS treated with dichloromethane: swollen weight without underestimation due to the solvent volatility and thermal aging to reduce swelling and morphology damage" (2017).

[92] B. Arkles. "Reactive Silicones: Forging New Polymer Links" (2016).

[93] James C Scanlan and H Henning Winter. "Composition dependence of the viscoelasticity of end-linked poly (dimethylsiloxane) at the gel point". *Macromolecules* 24.1 (1991), pp. 47–54.

[94] Zhanjie Tan, Raimund Jaeger, and G Julius Vancso. "Crosslinking studies of poly (dimethylsiloxane) networks: a comparison of inverse gas chromatography, swelling experiments and mechanical analysis". *Polymer* 35.15 (1994), pp. 3230–3236.

[95] Quang TrongáNguyen et al. “Sorption of organic solvents into dense silicone membranes. Part 1.—Validity and limitations of Flory–Huggins and related theories”. *Journal of the Chemical Society, Faraday Transactions* 89.24 (1993), pp. 4339–4346.

[96] Jin Sung Yoo, Sung Jun Kim, and Joong So Choi. “Swelling equilibria of mixed solvent/poly (dimethylsiloxane) systems”. *Journal of Chemical & Engineering Data* 44.1 (1999), pp. 16–22.

[97] A Tiwari et al. “The effect of surface roughness and viscoelasticity on rubber adhesion”. *Soft matter* 13.19 (2017), pp. 3602–3621.

[98] Jun Young Chung, Ido Regev, and L Mahadevan. “Spontaneous exfoliation of a drying gel”. *Soft matter* 12.37 (2016), pp. 7855–7862.

[99] Randy H Ewoldt, Michael T Johnston, and Lucas M Caretta. “Experimental challenges of shear rheology: how to avoid bad data”. In: *Complex fluids in biological systems*. Springer, 2015, pp. 207–241.

[100] Anand U Oza and David C Venerus. “The dynamics of parallel-plate and cone–plate flows”. *Physics of Fluids* 33.2 (2021), p. 023102.

[101] Clare M O’Connor, Jill U Adams, and Jennifer Fairman. “Essentials of cell biology”. *Cambridge, MA: NPG Education* 1 (2010), p. 54.

[102] Elisabeth A Marnik and Dustin L Updike. “Membraneless organelles: P granules in Caenorhabditis elegans”. *Traffic* 20.6 (2019), pp. 373–379.

[103] Clifford P Brangwynne et al. “Germline P granules are liquid droplets that localize by controlled dissolution/condensation”. *Science* 324.5935 (2009), pp. 1729–1732.

[104] Nicholas M Kanaan et al. “Liquid-liquid phase separation induces pathogenic tau conformations in vitro”. *Nature communications* 11.1 (2020), pp. 1–16.

[105] Susanne Wegmann et al. “Tau protein liquid–liquid phase separation can initiate tau aggregation”. *The EMBO journal* 37.7 (2018), e98049.

[106] M Green, R Sinkus, and LE Bilston. “High resolution 3D brain MR-elastography”. In: *Proc. Intl. Soc. Mag. Reson. Med*. Vol. 14. 2006.

[107] Nic D Leipzig and Molly S Shoichet. “The effect of substrate stiffness on adult neural stem cell behavior”. *Biomaterials* 30.36 (2009), pp. 6867–6878.

[108] Silvia Budday et al. “Mechanical properties of gray and white matter brain tissue by indentation”. *Journal of the mechanical behavior of biomedical materials* 46 (2015), pp. 318–330.

[109] Giulia Tarricone, Irene Carmagnola, and Valeria Chiono. “Tissue-Engineered Models of the Human Brain: State-of-the-Art Analysis and Challenges”. *Journal of Functional Biomaterials* 13.3 (2022), p. 146.

[110] Jens Eggers, John R Lister, and Howard A Stone. "Coalescence of liquid drops". *Journal of Fluid Mechanics* 401 (1999), pp. 293–310.

[111] L Duchemin, Jens Eggers, and C Josserand. "Inviscid coalescence of drops". *Journal of Fluid Mechanics* 487 (2003), pp. 167–178.

[112] A Menchaca-Rocha et al. "Coalescence of liquid drops by surface tension". *Physical Review E* 63.4 (2001), p. 046309.

[113] WD Ristenpart et al. "Coalescence of spreading droplets on a wettable substrate". *Physical review letters* 97.6 (2006), p. 064501.

[114] Robert W Hopper. "Plane Stokes flow driven by capillarity on a free surface". *Journal of Fluid Mechanics* 213 (1990), pp. 349–375.

[115] Paul R Kaneelil et al. "Three-Dimensional Self-Similarity of Coalescing Viscous Drops in the Thin-Film Regime". *Physical Review Letters* 129.14 (2022), p. 144501.

[116] Mingming Wu, Thomas Cubaud, and Chih-Ming Ho. "Scaling law in liquid drop coalescence driven by surface tension". *Physics of Fluids* 16.7 (2004), pp. L51–L54.

[117] Shana Elbaum-Garfinkle et al. "The disordered P granule protein LAF-1 drives phase separation into droplets with tunable viscosity and dynamics". *Proceedings of the National Academy of Sciences* 112.23 (2015), pp. 7189–7194.

[118] Mahdiye Ijavi et al. "Surface tensiometry of phase separated protein and polymer droplets by the sessile drop method". *Soft Matter* 17.6 (2021), pp. 1655–1662.

[119] Bruno Andreotti and Jacco H. Snoeijer. "Statics and Dynamics of Soft Wetting". *Annual Review of Fluid Mechanics* 52.1 (2020), pp. 285–308. DOI: 10.1146/annurev-fluid-010719-060147.

[120] Tadashi Kajiya et al. "Advancing liquid contact line on visco-elastic gel substrates: stick-slip vs. continuous motions". *Soft Matter* 9.2 (2013), pp. 454–461. DOI: 10.1039/c2sm26714d.

[121] R. W. Style et al. "Patterning droplets with durotaxis". *Proc. Natl. Acad. Sci. U.S.A.* 110.31 (2013), pp. 12541–12544. DOI: 10.1073/pnas.1307122110.

[122] S. Karpitschka et al. "Liquid Drops Attract or Repel by the Inverted Cheerios Effect". *Proc. Natl. Acad. Sci. U.S.A.* 113.27 (2016), pp. 7403–7407. DOI: 10.1073/pnas.1601411113.

[123] A. Pandey et al. "Dynamical theory of the inverted cheerios effect". *Soft Matter* 13 (2017), pp. 6000–6010. DOI: 10.1039/C7SM00690J.

[124] Qin Xu et al. "Viscoelastic and Poroelastic Relaxations of Soft Solid Surfaces". *Physical Review Letters* 125.23 (2020), p. 238002. DOI: 10.1103/PhysRevLett.125.238002.

[125] Dominic Mokbel, Sebastian Aland, and Stefan Karpitschka. "Stick-slip contact line motion on Kelvin-Voigt model substrates". *Europhysics Letters* 139.3 (2022), p. 33002. DOI: 10.1209/0295-5075/ac6ca6.

[126] Carlos Pérez-González et al. "Active wetting of epithelial tissues". *Nature Physics* 15.1 (2018), pp. 79–88. DOI: 10.1038/s41567-018-0279-5.

[127] John A. Rogers, Takao Someya, and Yonggang Huang. "Materials and Mechanics for Stretchable Electronics". *Science* 327.5973 (2010), pp. 1603–1607. DOI: 10.1126/science.1182383.

[128] Justin D. Glover et al. "Extracting uncrosslinked material from low modulus sylgard 184 and the effect on mechanical properties". *Journal of Polymer Science* 58.2 (2020), pp. 343–351. DOI: 10.1002/pol.20190032.

[129] Serge Mora et al. "Capillarity Driven Instability of a Soft Solid". *Physical Review Letters* 105.21 (2010), p. 214301. DOI: 10.1103/physrevlett.105.214301.

[130] Matthew G. Hennessy, Andreas Münch, and Barbara Wagner. "Phase separation in swelling and deswelling hydrogels with a free boundary". *Physical Review E* 101.3 (2020), p. 032501. DOI: 10.1103/physreve.101.032501.

[131] L. A. Lubbers et al. "Drops on soft solids: free energy and double transition of contact angles". *J. Fluid Mech.* 747 (2014), R1. DOI: 10.1017/jfm.2014.152.

[132] Binyu Zhao et al. "Elasticity-to-Capillarity Transition in Soft Substrate Deformation". *Nano Letters* 21.24 (2021), pp. 10361–10367. DOI: 10.1021/acs.nanolett.1c03643.

[133] Christopher Henkel, Jacco H. Snoeijer, and Uwe Thiele. "Gradient-dynamics model for liquid drops on elastic substrates". *Soft Matter* 17.45 (2021), pp. 10359–10375. DOI: 10.1039/d1sm01032h.

[134] Alain Carré, Jean-Claude Gastel, and Martin E. R. Shanahan. "Viscoelastic effects in the spreading of liquids". *Nature* 379 (6564 1996), pp. 432–434. DOI: 10.1038/379432a0.

[135] D Long, A Ajdari, and L Leibler. "Static and dynamic wetting properties of thin rubber films". *Langmuir* 12.21 (1996), pp. 5221–5230. DOI: 10.1021/la9604700.

[136] Robert W. Style et al. "Elastocapillarity: Surface Tension and the Mechanics of Soft Solids". *Annual Review of Condensed Matter Physics* 8.1 (2017), pp. 99–118. DOI: 10.1146/annurev-conmatphys-031016-025326.

[137] Robert W. Style et al. "Universal Deformation of Soft Substrates Near a Contact Line and the Direct Measurement of Solid Surface Stresses". *Phys. Rev. Lett.* 110 (6 2013), p. 066103. DOI: 10.1103/PhysRevLett.110.066103.

[138] Su Ji Park et al. "Visualization of asymmetric wetting ridges on soft solids with X-ray microscopy". *Nature Communications* 5.1 (2014), p. 4369. DOI: 10.1038/ncomms5369.

[139] Jacco H. Snoeijer, Etienne Rolley, and Bruno Andreotti. "Paradox of Contact Angle Selection on Stretched Soft Solids". *Phys. Rev. Lett.* 121.6 (2018), p. 068003. DOI: 10.1103/physrevlett.121.068003.

[140] M. van Gorcum et al. "Dynamic Solid Surface Tension Causes Droplet Pinning and Depinning". *Phys. Rev. Lett.* 121.20 (2018), p. 208003. DOI: 10.1103/physrevlett.121.208003.

[141] M. van Gorcum et al. "Spreading on viscoelastic solids: are contact angles selected by Neumann's law?" *Soft Matter* 16.5 (2020), pp. 1306–1322. DOI: 10.1039/c9sm01453e.

[142] R Shuttleworth. "The Surface Tension of Solids". *Proc. Phys. Soc. London, Sect. A* 63.5 (1950), pp. 444–457. DOI: 10.1088/0370-1298/63/5/302.

[143] Qin Xu et al. "Direct measurement of strain-dependent solid surface stress". *Nature Communications* 8.1 (2017). DOI: 10.1038/s41467-017-00636-y.

[144] Rafael D. Schulman et al. "Surface energy of strained amorphous solids". *Nat. Commun.* 9.1 (2018), p. 982. DOI: 10.1038/s41467-018-03346-1.

[145] Q. Xu, R. W. Style, and E. R. Dufresne. "Surface elastic constants of a soft solid". *Soft Matter* 14.6 (2018), pp. 916–920. DOI: 10.1039/c7sm02431b.

[146] Jin Young Kim et al. "Measuring Surface Tensions of Soft Solids with Huge Contact-Angle Hysteresis". *Physical Review X* 11.3 (2021), p. 031004. DOI: 10.1103/PhysRevX.11.031004.

[147] Katrina Smith-Mannschott et al. "Droplets Sit and Slide Anisotropically on Soft, Stretched Substrates". *Physical Review Letters* 126.15 (2021), p. 158004. DOI: 10.1103/PhysRevLett.126.158004.

[148] Stefanie Heyden et al. "Contact lines on stretched soft solids: modelling anisotropic surface stresses". *Proceedings of the Royal Society A: Mathematical, Physical and Engineering Sciences* 477.2245 (2021), p. 20200673. DOI: 10.1098/rspa.2020.0673.

[149] William S. Y. Wong et al. "Adaptive Wetting of Polydimethylsiloxane". *Langmuir* 36.26 (2020), pp. 7236–7245. DOI: 10.1021/acs.langmuir.0c00538.

[150] Julien Dervaux, Matthieu Roché, and Laurent Limat. "Nonlinear theory of wetting on deformable substrates". *Soft Matter* 16.22 (2020), pp. 5157–5176. DOI: 10.1039/d0sm00395f.

[151] Robin Masurel et al. "Elastocapillary ridge as a noninteger disclination". *Phys. Rev. Lett.* 122 (2019), p. 248004.

[152] Menghua Zhao et al. "Geometrical control of dissipation during the spreading of liquids on soft solids". *Proc. Natl. Acad. Sci. U.S.A.* 115.8 (2018), pp. 1748–1753. DOI: 10.1073/pnas.1712562115.

[153] Hamza K. Khattak et al. “Direct force measurement of microscopic droplets pulled along soft surfaces”. *Nature Communications* 13.1 (2022), p. 4436. DOI: 10.1038/s41467-022-31910-3.

[154] Aurélie Hourlier-Fargette et al. “Role of uncrosslinked chains in droplets dynamics on silicone elastomers”. *Soft Matter* 13.19 (2017), pp. 3484–3491. DOI: 10.1039/c7sm00447h.

[155] Zhuoyun Cai et al. “Fluid separation and network deformation in wetting of soft and swollen surfaces”. *Communications Materials* 2.1 (2021), pp. 1–11. DOI: 10.1038/s43246-021-00125-2.

[156] Chander Shekhar Sharma et al. “Enhanced Condensation on Soft Materials through Bulk Lubricant Infusion”. *Advanced Functional Materials* 32.17 (2021), p. 2109633. DOI: 10.1002/adfm.202109633.

[157] Lukas Hauer et al. “Phase Separation in Wetting Ridges of Sliding Drops on Soft and Swollen Surfaces”. *arXiv* (2022), p. 2208.11177. URL: arxiv.org/abs/2208.11177.

[158] Justin D. Glover et al. “Interfacial strength dominates fold formation in microscale, soft static friction”. *arXiv* (2022), p. 2203.09575. URL: arxiv.org/abs/2203.09575.

[159] Zida Li et al. “Syringe-pump-induced fluctuation in all-aqueous microfluidic system implications for flow rate accuracy”. *Lab Chip* 14 (4 2014), pp. 744–749. DOI: 10.1039/C3LC51176F.

[160] S. Karpitschka et al. “Droplets move over viscoelastic substrates by surfing a ridge”. *Nat. Commun.* 6 (2015), p. 7891. DOI: 10.1038/ncomms8891.

[161] Manohar Singh and Allen C. Pipkin. “Note on Ericksen's problem”. *Zeitschrift für angewandte Mathematik und Physik ZAMP* 16.5 (1965), pp. 706–709. DOI: 10.1007/bf01590971.

[162] A. Pandey et al. “Singular Nature of the Elastocapillary Ridge”. *Phys. Rev. X* 10.3 (2020), p. 031067. DOI: 10.1103/physrevx.10.031067.

[163] M. A. J. van Limbeek et al. “Pinning-induced folding-unfolding asymmetry in adhesive creases”. *Phys. Rev. Lett.* 127 (2021), p. 028001. DOI: 10.1103/PhysRevLett.127.028001.

[164] Martin H. Essink. “Soft Contact: from wetting to adhesion”. PhD thesis. Universiteit Twente, 2022.

[165] Caroline Kopecz-Muller et al. “Mechanical response of a thick poroelastic gel in contactless colloidal-probe rheology”. *arXiv* (2022), p. 2212.05821. URL: arxiv.org/abs/2212.05821.

[166] S. Karpitschka et al. “Soft wetting: Models based on energy dissipation or on force balance are equivalent”. *Proc. Natl. Acad. Sci. U.S.A.* 115.31 (2018), E7233–E7233. DOI: 10.1073/pnas.1808870115.

[167] Weiwei Zhao et al. “The role of crosslinking density in surface stress and surface energy of soft solids”. *Soft Matter* 18.3 (2022), pp. 507–513. DOI: 10.1039/d1sm01600h.

[168] Mees M. Flapper et al. “Reversal of Solvent Migration in Poroelastic Folds”. *arXiv* (2022), p. 2209.00887. URL: arxiv.org/abs/2209.00887.

[169] S. J. Park et al. “Self-spreading of the wetting ridge during stick-slip on a viscoelastic surface”. *Soft Matter* 13.44 (2017), pp. 8331–8336. DOI: 10.1039/c7sm01408b.

[170] Li-Heng Cai et al. “Soft Poly (dimethylsiloxane) Elastomers from Architecture-Driven Entanglement Free Design”. *Advanced Materials* 27.35 (2015), pp. 5132–5140.